Study of Formation of Molecules in the Star Forming Regions Using Continuous Time Random Walk Monte Carlo Simulation

THESIS SUBMITTED FOR THE DEGREE OF

DOCTOR OF PHILOSOPHY (SCIENCE)

IN

PHYSICS

BY

WASIM IQBAL

DEPARTMENT OF PHYSICS

UNIVERSITY OF CALCUTTA

JULY, 2014

To

My Dear Parents

...Your smiles, the best gift of my life...

Acknowledgments

I thank almighty Allah for keeping me physically and mentally in good health, I started this work and now have reached the end, have wished for your mercy and help when I have been good or wrong and I am grateful.

I remember my parents today, they loved me the most, I have been away from them for my work but always wished the same from them as if I am at home. The distance from you both is never been a distance but in miles only. My mother, "Mehrun Nisa", is my first teacher. I still follow many of those what I learned from you. My father, "Zafar Alam Ansari", always wanted us to study well and do good in life, I hope I have crossed first half of it and wish their good wishes for the next.

The first person I want to gratefully thank is Dr. Kinsuk Acharyya. He guided me throughout and provided valuable suggestions and needed informations which made my research work better. His patience, care and insight of various problem made it possible for me to carry out and complete many of topics. He gave me enough freedom in thinking and choosing my own problems during my research carrier. Whenever I had a problem without any hesitation I went to him and he made me understand the topic crystal clear. He is the one who is more than a supervisor to me, a friend, a colleague in my life.

I also thank Prof. Eric Herbst, who gave us very valuable suggestions. His great experience and knowledge of the subject has given me many things to learn, that helped me a lot in my research work.

I am thankful to my friends in S N Bose National Centre for Basic Sciences. I have been here for five years which is the second most after my home. Because of you all I can say this place my second home. So many names but you all have left this home. I miss you all and wish to meet again.

What I will miss the most after leaving Kolkata is my sister and her biryani, and Royal's biryani with Fahad.

Signature

List of Publications

In Journals :

- [†]**Iqbal, W.**, Acharyya, K., & Herbst, E.,
"Kinetic Monte Carlo Studies of H_2 Formation on Grain Surfaces Over a Wide Temperature Range".
The Astrophysical Journal,**751**, 581 (2012).

- [†]**Iqbal, W.**, Acharyya, K., & Herbst, E.,
"H_2 Formation in Diffuse Clouds: A New Kinetic Monte Carlo Study".
The Astrophysical Journal,**784**, 139 (2014).

- [†]**Iqbal, W.**, Acharyya, K., & Herbst, E.,
"Water Formation in Diffuse Clouds: A Kinetic Monte Carlo Study".
In preparation.

In Proceedings :

- **Iqbal, W.**, Acharyya, K.,
"Study of H_2 formation on the interstellar dust grains using CTRW Monte Carlo Simulation".
39th COSPAR Scientific Assembly, **39**, 7961 (2012).

- **Iqbal, W.**,
"Study of H2 Formation in the surface of the interstellar dust grains at high temperature using kinetic Monte Carlo Method".
AIP, **1543**, 278 (2013).

[†]Used for the present thesis

Abstract

We used the Continuous Time Random Walk Monte Carlo technique to study the formation of molecules on the surface of interstellar dust grains in the star forming regions. We considered both physisorption and chemisorption sites on different grain materials, olivine (a polycrystalline silicate), amorphous silicate and amorphous carbon. In first set of studies we found out H_2 formation efficiency at wider range of temperatures, which can be found in various regions associated with star formation, such as diffuse and dense clouds, photon dominated regions, proto-planetary discs. We considered mobility of atoms due to both thermal hopping and quantum mechanical tunneling. We explored, the temperature range between 5 K and 825 K for different incoming H fluxes representative of interstellar environments with atomic hydrogen number density ranging between 0.1 cm^{-3} and 100 cm^{-3} and dust grain sizes ranging from 10^2 sites to 10^6 sites. We also considered rough surfaces with multiple binding sites. In the second set of calculations, we used a parallel network of many grains following grain size distribution from the literature and studied H_2 formation in diffuse clouds. In the diffuse clouds grains temperature depends on its size. We performed two sets of calculations, one with fixed average temperature for each grain size, in other, we solved radiative transfer equation to find temperature fluctuations on grains due to stochastic heating caused by stellar ultra violet photons. We found that the standardly held assumption that the formation of H_2 occurs in a facile manner on grains with radii in the size range 0.005-0.25 micron is somewhat fragile in the sense that the rate of formation depends strongly on the surface used and its topology, the mechanism for the reaction, as well as on the type of binding of H. Then in the final set of calculations, we studied formation of water and other big molecules. We found that, formation of water mainly depends on coverage of O on the surface. Water formation rate goes down only when temperature is high enough to cause significant desorption of O from the surface else all O accreted to the surface is converted to water. We found that when average grain temperature is used under diffuse cloud conditions, there is no size dependence on the water formation. However, when we used temperature fluctuations, then small grains do not produce any water on their surface due to higher temperature due fluctuations and only bigger grains can produce water and that too at reduced rate. Molecules other than H_2 and water such as H_2O_2, O_3 etc., is not produced in significant numbers under diffuse cloud conditions.

Contents

List of Figures

List of Tables

1 General Introduction and Overview

1.1 Introduction

Our Galaxy, the Milky Way is a member of local group of about 30 galaxies. It contains about few hundred billions of stars, which are separated from each other by large distance. Our eyes can see nothing in this vast space between stars, earlier it was thought to be an empty and void in space, a perfect vacuum. However, now we know that this space is filled with tenuous gas, small sub-micron particles called grains, energetic radiation and magnetic field and we called this region as interstellar medium (ISM). The average particle density in the interstellar medium is roughly a factor of about 10^{19} less than in the terrestrial atmosphere at sea level. Thus, the ISM is a very diffuse medium and by terrestrial standards it can be considered as a near-perfect vacuum. Despite the fact that most of the interstellar region is extremely dilute, there is still about of 5-10 billion solar mass of gas and dust in the ISM, which is approximately 5% of the mass of visible stars in the Galaxy. The matter in the ISM is predominantly composed of about 99% gas by mass, with rest 1% mass of the ISM being found in dust grains. The gas within the ISM is roughly composed of $\sim$ 90% H and $\sim$ 10% He by number density and very small amount of other heavier elements like, carbon, nitrogen, oxygen, iron etc.

The primordial interstellar medium was formed in the big bang. The chemical history of the Universe as a result of Big bang is not very diverse, being made up of mostly hydrogen, small amount of helium and with a very small amount of lithium, beryllium and boron. The first generation stars were formed with this composition only. These elements are continuously fused in the core of the stars to yield further heavier elements like, carbon, nitrogen, oxygen and elements up to iron depending on the mass of the star. Some of these early stage stars, which were massive and had produced heavier element due to fusion in their core, died with a gigantic explosion called supernovae which provided the favorable condition for the synthesis of elements heavier than iron. In such Supernovae explosions much of the matter is thrown back into the interstellar medium, changing chemical composition of the local ISM. In this way, the abundance of heavy elements in the ISM continuously and gradually increases which in turn provides essential ingredients for the next generation stars.

With enrichment of the ISM with heavier elements, ejected from the cores of dying stars, a new life cycle of rich molecular chemistry starts. This chemical evolution of elements in the ISM leads to the formation of numerous exotic molecules. So far, more than 180 molecules have been discovered through their electronic (these transitions are in the ultraviolet or in the visible range), vibrational (arises in the infrared wavelengths), and rotational spectra (lie in the radio wavelengths). Many of these molecules deplete during various evolutionary phases of star formation onto cold grains and are eventually incorporated into the planetesimals of new stellar systems. Recent observations of comets such as Hyakutake and Hale-Bopp show remarkable similarity between the composition of interstellar and cometary ices. Analysis of carbonaceous meteorites show a high deuterium level which is also an indicator of their interstellar origin. Thus studying various physical and chemical processes which are responsible for the formation of these molecules are of primary importance. In this thesis, I studied few such problems in

which formation of few important molecules e.g., H_2, H_2O etc., in variety of astrophysical environment have been discussed.

In this chapter, I will give a brief overview of the ISM and its different components which are relevant for the thesis work.

1.2 Early concept of ISM

Till late 19th century, our galaxy, the Milky Way was considered to be the whole Universe and all the observed stars were considered to be within our galaxy. The Milky Way was thought to consist of stars in complete vacuum. Later with their observations, Herschel and others realized that there are other larger bodies and structures which are not stars. However, still major portion of the ISM was known to be empty and void of anything.

Vesto Slipher of Lowell Observatory obtained a spectrum of the Pleiades reflection nebulosity in the early 20th century and found it to be reflected starlight, leading to his speculation that it was reflection from small particles. The first observational evidence came from photographic study of spectroscopic binary stars that there is a general ISM that fills the space between the stars. Observations showed that there were very narrow stationary lines in addition to the relatively broad absorption lines associated with the atmospheres of the stars. Hartmann first identified the narrow stationary lines of H and K in the spectrum of the spectroscopic binary star δ Ori in 1904. These narrow stationary lines were particularly noticeable in the spectra of bright O and B stars. The narrow stationary lines had the following properties:

(i) The lines are very narrow, with equivalent widths of a few mÅ.

(ii) Their strengths are correlated with distance: lines from more distant stars were stronger as shown by Plaskett and Pierce in the 1930s.

(iii) Their radial velocities (relative to the local standard of rest) showed a sine-wave pattern with galactic longitude consistent with galactic rotation.

In the 1930s, Robert J. Trumpler from Lick Observatory proved that there was a general absorbing medium that causes the extinction of starlight. Trumpler noticed that linear diameters of open clusters increase with distance from the Sun. He concluded that this apparent increase is caused by the unaccounted interstellar extinction that makes photo metric distances to the open clusters greater than they are in reality. It was also the first indication for the existence of dust particles. van de Kamp found that the galaxy count decreases towards the galactic plane. He calculated the total absorption by which the intensity of light passing perpendicularly through the intervening layers is diminished. Thus in the early years of the 20th century the idea of empty interstellar space was replaced by an interstellar medium which is homogeneous and diffuse. Later work on the observed stationary lines led to the idea of "clouds" or huge clump of matter in the ISM, that is, the matter in the ISM is not distributed uniformly throughout but there exists regions of high atomic and molecular densities.

1.3 General properties of different regions in the ISM

The composition of our galaxy (Milky Way) is made of stars, which provide a mass of approximately 10^{10} to 10^{11} times the solar mass ($M_\odot$), and the interstellar matter that provides a mass of $\sim 10^9\ M_\odot$. Both stars and the interstellar matter are distributed predominantly on the disk of the galaxy, with a typical radius of 10 kpc and a thickness of 250 pc. In addition, there is a halo of invisible matter around the galaxy making up $\sim 10^{12}\ M_\odot$, which is distributed more spherically. Although the average density of gas in the ISM is about one hydrogen atom per cubic cm, the density distribution is far from uniform. The density varies from ~ 0.01 hydrogen per cubic cm in the hot medium to 10^4

- 10^7 cm^{-3} hydrogen in the dense molecular clouds. Similarly, temperature can also vary from 10 K in dense clouds to $\sim 10^6$ K in hot ionized gas. Nearly half of the interstellar matter is confined to discrete clouds occupying only $\sim$ 1-2 % of the interstellar volume. Densest region of these clouds are the birth place of stars.

1.3.1 Interstellar clouds

The interstellar clouds are the local concentrations of matter in ISM separated by the low density inter cloud medium. These clouds constitute an extremely important component of ISM because these are the sites for star formation and contain the bulk of the total mass of ISM. Interstellar clouds differ significantly in their physical and chemical structure. Depending on various physical quantities like visual extinction, number density of hydrogen, the clouds can be divided into four major classes (Table 1.1): i) Diffuse atomic - these are the most tenuous clouds which are completely exposed to the stellar radiation, ii) Diffuse molecular, iii) dense clouds - these are densest regions of interstellar medium, and finally, iv) the translucent clouds are of intermediate density (Snow and McCall (2006)).

Table 1.1: Classification of interstellar cloud types

	Diffuse Atomic	Diffuse Molecular	Translucent	Dense Molecular
Defining characteristics	$f^n_{H_2} < 0.1$	$f^n_{H_2} > 0.1$, $f^n_{C^+} > 0.5$	$f^n_{C^+} < 0.5$, $f^n_{CO} < 0.9$	$f^n_{CO} > 0.9$
A_V	0	~ 0.2	~ 1 - 2	> 2
Typical n_H	10 - 100	100 - 500	500 - 5000	10^4
Typical T(K)	30 - 100	30 - 100	15 - 50	10 - 50
Operational	UV / Vis	UV / Vis, IR	Vis (UV) IR	IR

1.3.1.1 Diffuse Atomic Clouds

The diffuse atomic clouds are the region of ISM which are completely exposed to the Interstellar Radiation Field (ISRF). The visual extinction is less than 0.1, typical temperature is in between 30K and 100K and density is around 10 - 100 cm^{-3} . The fraction of hydrogen in its molecular form ($f^n_{H_2}$) is less than 0.1. These regions are sufficiently optically thin and can be observed by means of visible and ultraviolet (UV) absorption lines. Hydrogen is mostly in neutral form, and atoms with lesser ionization potential than hydrogen are in ionized form. Scarcity of molecular species implies that very little chemical processes occur in these clouds (Snow and McCall (2006)).

1.3.1.2 Diffuse Molecular Clouds

This is the region of the diffused cloud where molecules begin to form due to some attenuation of the interstellar radiation field provided by the diffuse atomic gas that surrounds these regions. Typical visual extinction is less than that of 1. Molecular hydrogen begins to form in substantial amount ($f^n_{H_2} > 0.1$). Although few molecules e.g., CO, CH, CN, C_2, C_3, H^+, HCO^+, OH, C_2H etc. are observed in this region for $A_V > 0.3$, the ISRF is still sufficiently strong to keep most of the carbon in C^+ form through photo-ionization (atomic carbon) and photo-dissociation (CO). This also implies that chemical reactions have only just started. These clouds have temperatures typically between 30K and 100K (since ISRF causes the heating of gas, the temperature of these clouds decrease with increasing column density) and densities between 100 cm^{-3} and 500 cm^{-3} . Diffuse molecular clouds can be observed for a wide variety of visual extinction, or total column density.

1.3.1.3 Translucent clouds

These are the regions of ISM where ISRF is so attenuated that conversion of ionized carbon to neutral carbon or carbon monoxide is possible at a substantial rate. These types of clouds are introduced (van Dishoeck and Black (1989)) to emphasize on this change. These clouds, in steady state, must be surrounded by diffuse molecular clouds and therefore, the visual extinction for these clouds should be more than unity. The translucent cloud regime is the least understood of all the clouds due to the lack of the observational data. The existing theoretical models also do not always agree. Recently, a working definition for these clouds has been proposed as the gas with $f^n_{C^+} < 0.5$ and $f^n_{CO} < 0.9$, where, $f^n_{C^+}$ and f^n_{CO} are the fractions of carbon in ionized form and in the form of carbon monoxide respectively. Thus, the ionized carbon is no longer the dominant form of carbon. The presence of the molecular hydrogen and the absence of C^+ make the chemistry different from that of the diffuse clouds.

1.3.1.4 Dense Molecular Clouds

These are the clouds with visual extinction more than 2 magnitude. The gas in these clouds is mostly molecular, most of the recently known interstellar molecules are discovered in these regions through observations of microwave rotational transitions. Hydrogen is mainly in molecular form and carbon is in CO form. These clouds are mainly self-gravitating and the temperature can be as low as 10 K and typical density is in between 10^4 cm^{-3} and 10^7 cm^{-3} . These regions are very well studied both from the observational and the theoretical point of view. Figure 1.1 shows, the Horsehead Nebula, which is embedded in the vast and complex Orion Nebula.

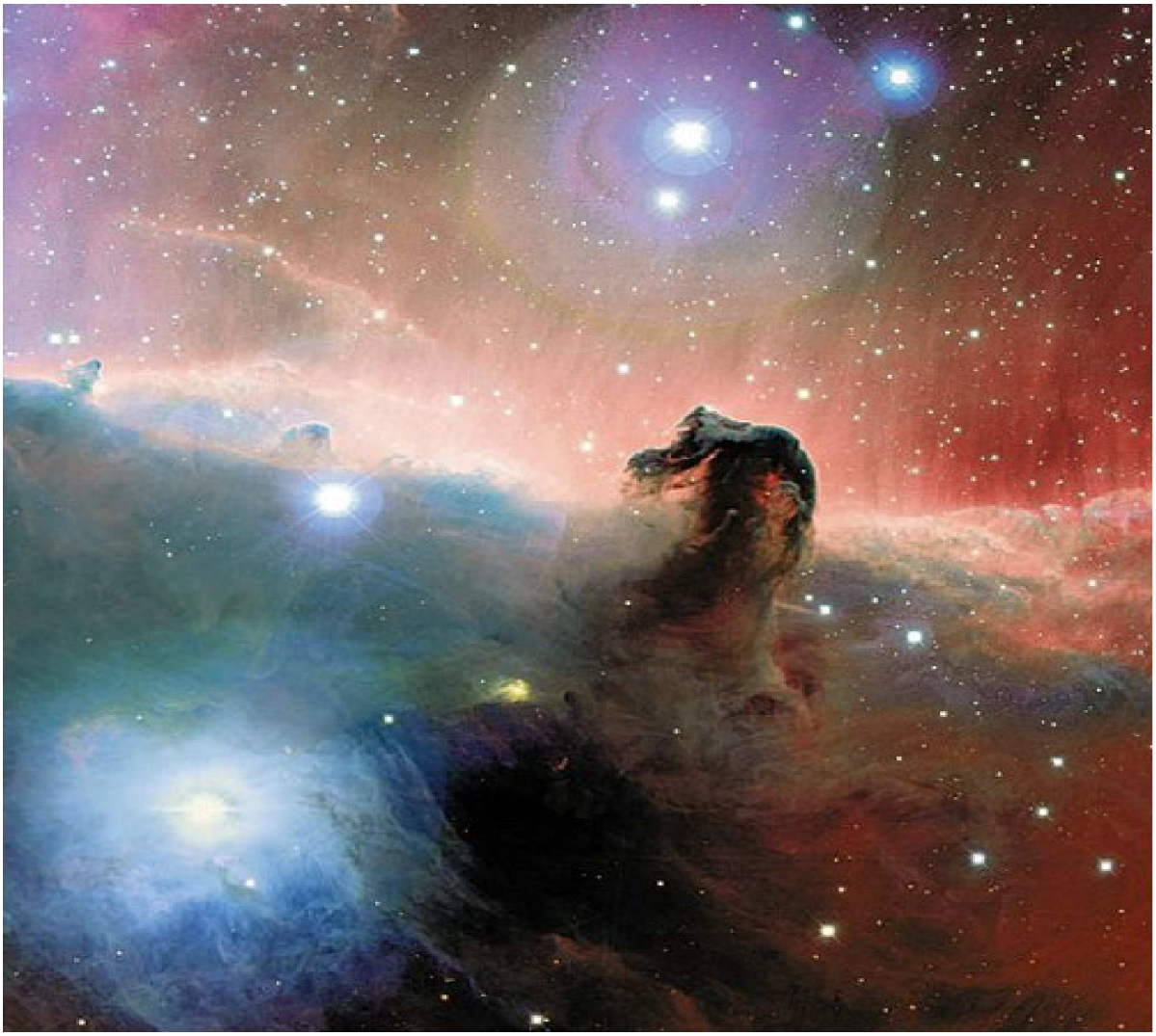

Figure 1.1: Image of Horsehead Nebula. Figure taken from http://www.nasa.gov.

1.4 Components of the ISM

The ISM is a dilute region but it is far from being a simple void space, other than the various energy sources, it contains dilute gases and dust grains.

1.4.1 Energy Sources in the ISM

The ISM is filled with electromagnetic radiation. Basic energy sources in the ISM are stellar objects, high energy particles, and mechanical energy from supernovae, stellar winds and differential rotation of galaxy.

1.4.1.1 Interstellar Radiation Field

Interstellar radiation field is the electromagnetic radiation, produced by stars and interstellar matter, that fills the ISM. The radiation field spectrum is dominated by the emission from stars of late spectral classes, which has a large peak in the near infrared, at wavelength of about 1 micron. The energy density of this component has a local value of about 0.5 eV/cm^3 (Mathis et al. (1983)).

A second stellar component, due to stars of class OB, has a peak in the ultraviolet range (at 0.1 micron) but has an energy density lower by about an order of magnitude. Energy density and spectrum of the radiation field show large variation along the Galaxy depending on the distribution of the stars spectral type. In particular, toward the Galactic center an energy density distribution larger by a factor 3-10 and with a softer spectrum could be found.

Another component of the interstellar radiation field is due to emission in the far infrared of the dust associated with the interstellar matter and heated by absorption of star light. Depending on the temperature, it is possible to distinguish three components (Cox et al. (1986)).

(i) Cold Dust, with temperature of about 10-25 K, is associated to the HI regions and to the molecular clouds. It may be heated by both old and young stellar population.

(ii) Warm Dust, with temperature of about 30-40 K, is associated to HII regions and is heated by stars of spectral class O and B.

(iii) Hot dust, with temperature of about 250-500 K is constituted of very small (radius ~ 5 Å) grains heated by general ISRF and normal grains (radius ~ 0.1 μm) heated by M giants.

This temperature distribution gives rise to a spectrum with a main peak corresponding to a wavelength of 100 micron and to a secondary peak around 10 micron. Even if the dust component is less known, its energy density can be estimated between 0.05 and 0.3 eV (Strong et al. (2000); Mathis et al. (1983); Chi et al. (1991)).

The dominant source of ionizing photons is hot, young stars in the disk. These are thought to account for a major fraction of the Reynolds layer ionization although it is unknown just how half the UV photons manage to escape the dense star-forming regions. It is possible that HII regions are highly porous or that some (runaway) O stars are ejected from the stellar nurseries. The observed Hα flux along the Magellanic stream suggests that 5-10 per cent of the UV field escapes into the Galactic halo (Bland et al. (1999)).

1.4.2 Cosmic rays

The cosmic rays are high energy ($>$ 100 MeV) charged particles, originating in outer space and traveling at nearly the speed of light. Cosmic rays include essentially all of the elements in the periodic table; about 89% of the nuclei are protons with energies between 1 and 100 GeV, 10% helium, and about 1% heavier elements with the same relative abundances as in the solar system. But there are important differences in elemental and isotopic composition that provide information on the origin and history of galactic cosmic rays. For example, there is a significant overabundance of the rare elements Li,

Be, and B produced when heavier cosmic rays such as carbon, nitrogen, and oxygen fragment into lighter nuclei during collisions with the interstellar gas. The isotope ^{22}Ne is also overabundant, showing that the nucleosynthesis of cosmic rays and of the solar system material have differed. The interaction of cosmic rays with interstellar matter and photons gives to gamma ray radiation through various mechanism, through π^0 meson decay, Coulomb acceleration of cosmic ray electrons leads to gamma ray bremsstrahlung emission and inverse Compton scattering. It is believed that the cosmic ray derives its energy from the supernova explosions with an efficiency 10% of the kinetic energy of the ejecta. The pressure due to cosmic ray provides a support against the gravity for the gas in ISM. Low energy $\sim$ 100 MeV cosmic rays are very important for the heating and ionization of interstellar matter. Indirect measurements provide a primary cosmic ray ionization rate in the ISM of $\sim 2^{-6}$ (H atom)$^{-1}$ s^{-1} . In regions associated with massive stars, this rate can be significantly higher. Cosmic rays are also important for the desorption of molecules from the grain surface.

1.4.3 Gas in the ISM

Hydrogen and helium in gaseous state make up most of the mass in the ISM, with a very small fraction being contributed by other heavier elements. The gases in different regions of the ISM are found in a variety of phases, namely, coronal gas, ionized gas, neutral atomic gas and molecular gas (Tielens (2005)). The most abundant species in the ISM, hydrogen exists as neutral (HI), singly ionized (HII) and in molecular (H_2) form, with HI dominating at larger distances from the center of the galaxy. The physical properties of different phases of gas in the ISM are summarized in Table 1.2.

Although the density in the ISM is very low, gases in the ISM take part in chemical reactions, either in the gas form or on the surface of dust grains. So, there are two form

of gas, atomic and molecular.

Table 1.2: Characteristics of gases in different regions of the ISM: coronal gas and hot ionized medium (HIM), warm ionized medium (WIM), H II regions, warm neutral medium (WNM), cold neutral medium (CNM), and molecular clouds. The values in this Table are taken from Ioppolo (2010).

Component	Fractional Volume (%)	Scale Height (pc)	Temperature (K)	Density (cm^{-3})	Sate of Hydrogen
Coronal Gas					
HIM	30-70	1000-3000	10^6-10^7	10^{-4}-10^{-2}	ionized
WIM	20-50	1000	8000	0.2-0.5	ionized
H II regions	< 1	70	8000	10^2-10^4	ionized
WNM	10-20	300-400	6000-10000	0.2-0.5	neutral atomic
CNM	1-5	100-300	50-100	20-50	neutral atomic
Molecular clouds	< 1	70	10-50	10^2-10^6	molecular

1.4.3.1 Molecules in the ISM

First signature of molecular species were found by Merrill (1936). He detected four new bands whose wavelengths are 5780, 5796, 6284 and 6614 Å. In the subsequent years the possible signature of CH, CH^+ and CN were found in the interstellar absorption lines superimposed on the spectra of bright stars Dunham (1937); Swings and Rosenfeld (1937); Mckellar (1940). These lines are detected in the optical wavelengths. Hendrik van de Hulst, predicted in 1944 that in the cold regions of the ISM (10K) neutral hydrogen atoms can radiate line emission at 21-cm wavelengths via hyper fine atomic transitions in the ground state. Ewen and Purcell conclusively proved the existence of neutral hydrogen in the cold ISM in the year of 1951. Subsequently Muller and Oort (1951) also detected this line. Faint radio emission from cold HI was found to pervade the disk of the Milky Way.

This discovery was perhaps the most important one in the radio-astronomy of ISM.

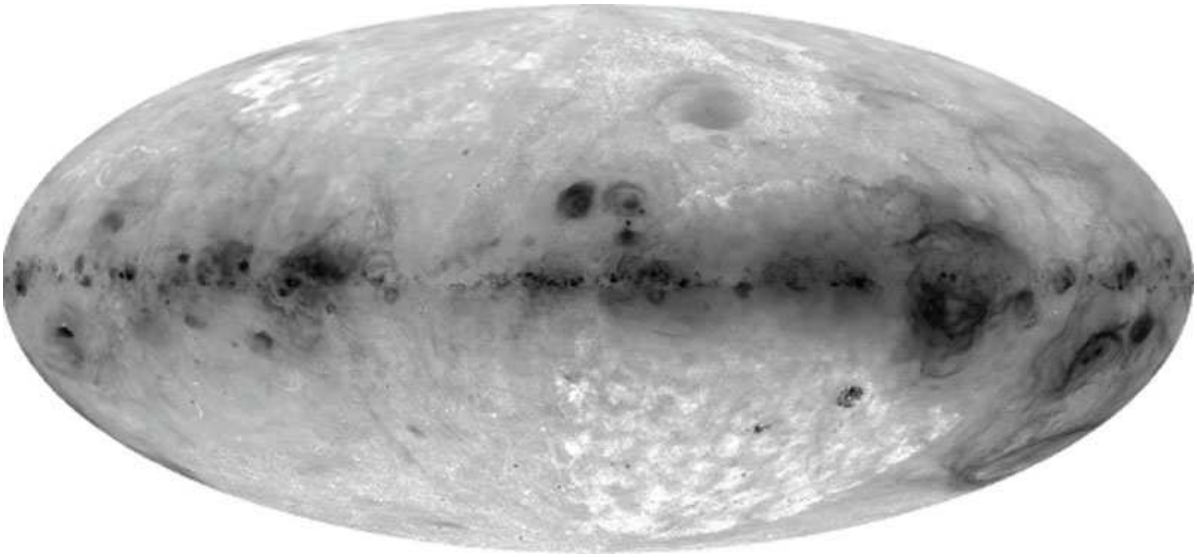

Figure 1.2: A composite view of the Hα sky. Figure taken from http://ned.ipac.caltech .edu/level5/March13/Haffner/Haffner4.html.

It initiated the era of radio-wavelength studies of the ISM and since then the radio wave become principal tool for mapping ISM in the Milky Way as well as other galaxies and in the inter-galactic medium. In 1963 Weinreb et al. (1963) reported detection of the 18-cm lines of the OH radical. This was the first direct detection of emission lines at radio wavelengths. They observed the lines in the absorption in the spectrum of Cassiopeia A at frequencies which closely agrees with laboratory values. In 1968, Cheung et al. (1968) detected emission from the poly-atomic molecules of NH_3 (ammonia) at 1.2 cm, in 1969, Cheung et al. (1969) observed water and Snyder et al. (1969) reported H_2CO (formaldehyde) in discrete interstellar clouds using radio detection methods. One of the most important of the molecular tracers at mm wavelengths, the CO (J=1-0) emission line at 2.6mm was first detected in 1970 by Wilson et al. (1970). Detection's of interstellar CN and HCN was made later in the 1970s.

H_2, which is the most abundant molecule in the ISM is also the most hard molecule to detect using radio-wavelength. It has no permanent dipole moment because it is a homo nuclear diatomic molecule, and so it does not emit radio-wavelength lines, unlike

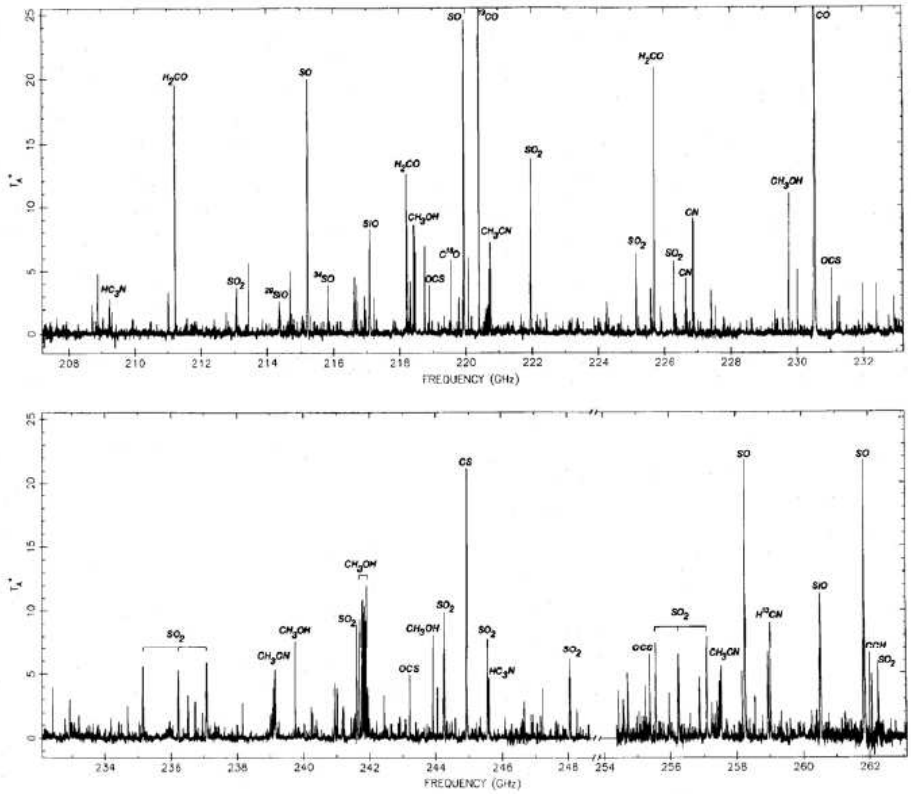

Figure 1.3: Owens Valley Radio Observatory (OVRO) spectral line survey of various molecules.

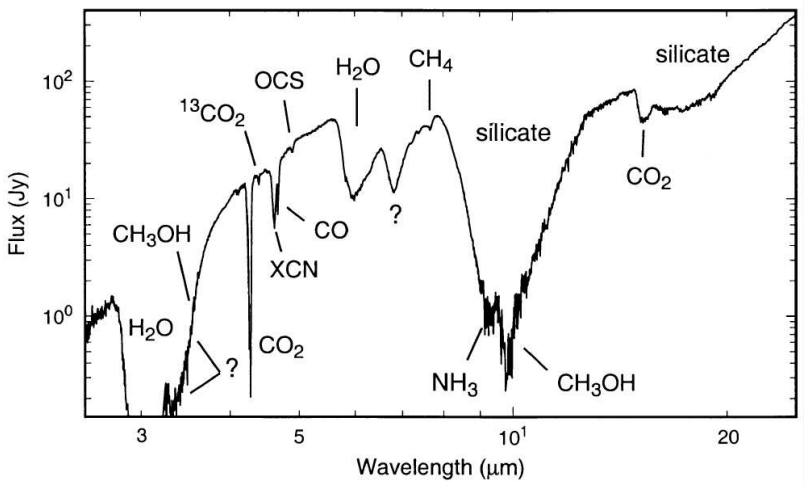

Figure 1.4: ISO-SWS spectrum of YSO W33A. Various absorption features due to silicate grain cores and icy mantles are shown (Gibb et al., 1999)

CO, OH, and others. Interstellar H_2 was first detected in absorption towards hot stars in the satellite UV in 1973 by Carruthers et al. This period marks the beginning for the search of interstellar molecules. The interstellar medium contains a large number of complex molecules, so far around 180 molecules have been detected in various regions of ISM. Fig. 1.3 shows the spectral line survey of various molecules which is done by Owens Valley Radio Observatory (OVRO). Many of these molecules are organic, i.e., they include hydrogen, carbon and nitrogen. These molecules range in complexity from H_2 to a 13-atom linear nitrile, $HC_{11}N$ and many of these molecules are quite unusual to find in ISM by terrestrial standards. H_2 is the most abundant molecule by far, with CO in the second position, four order of magnitude lower. More complex molecules are even less abundant, at least 4 to 10 orders of magnitude lower than H_2 . These molecules are very important because they can be the pre-cursors of more complex bio-molecules including simple amino acids, such as glycine. If amino acids and other pre-biotic molecules are formed in the evolution of molecular cloud and accreted in the form of dust, meteorites and comets, they may have provided essential ingredients for pre-biotic synthesis on earth. Most interestingly, the possible molecular precursors of glycine such as, CH_4 , H_2O, NH_3 , HCOOH, CH_3COOH are all discovered in the various regions of ISM. However, the simplest amino acid, namely, glycine itself eluded confirmed detection. So far, numerous searches for interstellar glycine have been conducted but the intrinsic weakness of the glycine lines coupled with the contamination of the spectrum by other molecules make it very difficult for such confirmation (Kaun et al. (2003); Holis et al. (2003)). Besides these, there are poly cyclic aromatic carbons (PAHs), containing some 50 C atoms. These molecules are abundant, $\sim 10^7$ relative to H, locking up about 10% of the elemental carbon. These molecules show broad emission mid-infrared features in the spectrum of most IR objects.

Table 1.3: Molecules found in interstellar clouds of various sorts.

Molecules with 2 atoms				
H_2	AlF	AlCl	C_2	CH
CH^+	CN	CO	CO^+	CP
SiC	HCl	KCl	NH	NO
NS	NaCl	OH	PN	SO
SO^+	SiN	SiO	SiS	CS
HF	HD	FeO	O2	CF^+
SiH	PO	AlO	OH^+	CN^-
SH^+	SH	HCl^+	TiO	ArH^+
Molecules with 3 atoms				
C_3	C_2H	C_2O	C_2S	CH_2
HCN	HCO	HCO^+	HCS^+	HOC^+
H_2O	H_2S	HNC	HNO	MgCN
MgNC	N_2H^+	N_2O	NaCN	OCS
SO_2	c-SiC_2	CO_2	NH_2	H_3^+
SiCN	AlNC	SiNC	HCP	CCP
AlOH	H_2O^+	H_2Cl^+	KCN	FeCN
HO_2	TiO_2			
Molecules with 4 atoms				
c-C_3H	l-C_3H	C_3N	C_3O	C_3S
C_2H_2	NH_3	HCCN	$HCNH^+$	HNCO
HNCS	$HOCO^+$	H_2CO	H_2CN	H_2CS
H_3O^+	ciC_3	CH_3	C_3N	PH_3
HCNO	HOCN	HSCN	H_2O_2	C_3H^+
HMgNC				
Molecules with 5 atoms				
C_5	C_4H	C_4Si	l-C_3H_2	c-C_3H_2
H_2CCN	CH_4	HC_3N	HC_2NC	HCOOH
H_2CNH	H_2C_2O	H_2NCN	HNC_3	SiH_4
H_2COH^+	C_4H^-	HC(O)CN	HNCNH	CH_3O
NH_4^+	H_2NCO^+			
Molecules with 6 atoms				
C_5H	l-H_2C_4	C_2H_4	CH_3CN	CH_3NC
CH_3OH	CH_3SH	HC_3NH^+	HC_2CHO	NH_2CHO
C_5N	l-HC_4H	l-HC_4N	c-H_2C_3O	H_2CCNH
C_5N^-	HNCHCN			
Molecules with 7 atoms				
C_6H	CH_2CHCN	CH_3C_2H	HC_5N	CH_3CHO
CH_3NH_2	c-C_2H_4O	H_2CCHOH	C_6H^-	
Molecules with 8 atoms				
CH_3C_3N	$HC(O)OCH_3$	CH_3COOH	C_7H	H_2C_6
CH_2OHCHO	l-HC_6H	CH_2CHCHO	CH_2CCHCN	H_2NCH_2C
CH_3CHNH				
Molecules with 9 atoms				
CH_3C_4H	CH_3CH_2CN	$(CH_3)_2O$	CH_3CH_2OH	HC_7N
C_8H	$CH_3C(O)NH_2$	C_8H^-	C_3H_6	CH_3CH_2SH
Molecules with 10 atoms				
CH_3C_5N	$(CH_3)_2CO$	NH_2CH_2COOH	CH_3CH_2CHO	$(CH_2OH)_2$
Molecules with 11 atoms				

Continued on next page

Table 1.3 – *Continued from previous page*

HC_9N	CH_3C_6H	C_2H_5OCHO	$CH_3OC(O)CH_3$
Molecules with 12 atoms			
c-C_6H_6	$CH_3OC_2H_5$	n-C_3H_7CN	
Molecules with $>$ 12 atoms			
$HC_{11}N$	C_{60}	C_{70}	

1.4.4 Dust Grains

Interstellar dust grains contribute about 1% to the total mass in the ISM. These varies in size ranging from few nanometers to micrometers. These grains are irregular in shape and size, mostly composed of carbon and/or silicates, and are intimately mixed with the interstellar gas. They are formed in the atmospheres of evolved stars as well as in novae and supernovae. Although just 1% by mass, they play a vital role in the formation of molecules in the ISM, in the energy balance of the galaxy, in the star and planet formation and in many other processes.

Presence of dust in the ISM is felt by two major ways on light passing through it: 1) the light is dimmed due to absorption by dust grains, this phenomena is called the interstellar extinction, 2) through reddening of star light due to scattering, this is known as the interstellar reddening. Dust grain also causes the polarization of starlight. ISM is bright in infrared due to the continuum emission by cold dust grains. Interstellar grains take part in the chemical evolution of the interstellar matter. There are two ways in which interstellar grains control the chemistry. In one, it provides the surface for chemical reactions, e.g., H_2 formation. In other, the grains control the gas phase chemistry through freeze out and desorption processes. In the cold clouds, the gas phase species sticks very efficiently onto the grains forming ice mantles. In the absence of suitable desorption mechanism this mantle grows until on the later stage of star formation when the the grains are warmed to the temperature where the molecules can

desorb again. These desorbed molecules then takes part in the chemical evolution of this region. The ground-based and ISO studies discovered a nearly complete inventory of these ice mantles for deeply embedded massive young stars such as NGC 7538 IRS9, W33 A and RAFGL 7009S Whittet et al. (1996). The observed grain mantle composition are mainly consists of hydrogenated species like H_2O, CH_4, NH_3, CH_3OH and oxidized species like CO, CO_2 etc. Fig. 1.4 shows, molecular absorption features from the grain mantle.

1.5 Physical Processes for Molecule Formation

Molecules can form both in the interstellar gas and dust. Exothermic ion molecular reactions are the most probable (endothermic reactions are not possible in the cold conditions like interstellar medium) gas phase reactions. The initiating process is the cosmic ray ray induced ionization of H_2 to yield mainly H_2^+, via following reaction:

$$H_2 + CR \rightarrow H_2^+ + e^- + CR, \tag{1.1}$$

where, CR stands for cosmic rays. This H_2^+ ion then reacts with H_2 and produces H_3^+. H_3^+ is very important radical because it then reacts with carbon to produce the simplest hydro-carbon,

$$C + H_3^+ + \rightarrow CH^+ + H_2 \tag{1.2}$$

$$CH^+ + H_2 \rightarrow CH_2^+ + H \tag{1.3}$$

$$CH_2^+ + H_2 \rightarrow CH_3^+ + H \tag{1.4}$$

$$CH_3^+ + H_2 \rightarrow CH_5^+ + h\nu \tag{1.5}$$

$$CH_5^+ + e^- \rightarrow CH_4 + H \tag{1.6}$$

again, this could similarly produce $C_3H_3, C_2H_5, C_6H_4^+, C_2H_5, C_3H_7, C_3H_7O, C_2H_5O$ etc. Similarly, nitrogenated compounds like ammonia NH_3 could also be produced, which then reacts,

$$CH_3 + +NH_3 \rightarrow CH_3NH_3 + h\nu \quad (1.7)$$

$$CH_3^+ + HCN \rightarrow CH_3CNH^+ + h\nu \quad (1.8)$$

which then produce methyl amine and aceto-nitrile via dissociative recombination reactions.

The oxygen-containing molecules such as water, in standard gas-phase chemistry, forms through ion-molecule reactions starting with the formation of OH^+ via following reactions:

$$O + H_3^+ \rightarrow H_2 + OH^+ \quad (1.9)$$

$$O + H_2^+ \rightarrow H + OH^+, \quad (1.10)$$

Then a series of rapid hydrogen abstraction reactions with H_2 leads to H_3O^+, which can dissociatively recombine to form H_2O and OH with branching ratios of $\sim$ 0.33 % and $\sim$ 66 % respectively. Other complex oxygen bearing molecules such as alcohol, acetaldehyde, dimethyl ether etc. can also be produced from the following reactions,

$$CH_3^+ + H_2O \rightarrow CH_3OH_2^+ + h\nu \quad (1.11)$$

$$H_3O^+ + C_2H_2 \rightarrow CH_3CHOH^+ + h\nu \quad (1.12)$$

$$CH_3^+ + CH_3OH \rightarrow (CH3)_2OH^+ + h\nu. \quad (1.13)$$

Modern day gas phase networks consists of around 5000 reactions among around 500

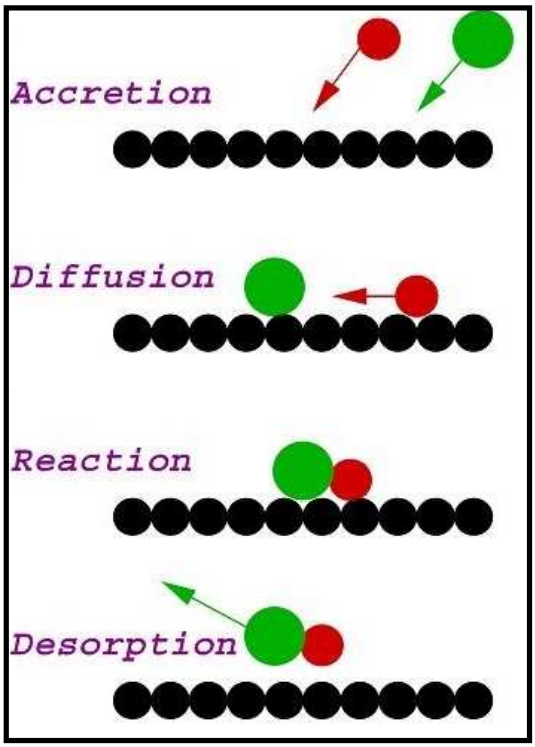

Figure 1.5: Physical processes that accruing on a grain surface

species.

Understanding the mechanism of molecule formation onto a grain surface requires a knowledge of the basic physical processes that are involved when the gas phase species interacts with grains (Fig. 1.5). The first step is accretion, i.e., landing of an atom/molecules onto a grain, The accretion rate of a given species i is given by,

$$r_{acc}(i) = \xi(i)\sigma v_i n_g(i) n_d, \tag{1.14}$$

where, ξ is the sticking coefficient, v_i is the thermal velocity (cm s^{-1}), $n_g(i)$ is the gas phase concentration of the i^{th} species and σ is the grain cross-section (cm^2). In the next step, accreted species will react to form a molecule. Reactions occur via the Langmuir-Hinshelwood mechanism, i.e., reactants migrate around the grain surface until they meet at a binding site. Migration occurs by thermal hopping of reactants over the diffusion

energy barrier E_b between sites. Initially it was thought that mobility of the atoms on a grain surface is due to quantum mechanical tunneling. However, Recent laboratory experiments revealed that mobility on the grain surface is mainly due to thermal hopping although, many models consider both the hopping and tunneling. Diffusion energy barriers define the rates at which reactions take place. In addition to this their could be activation energy barrier E_A. In the cold star forming regions only exothermic reactions or reactions with small E_A is relevant. The rate of hopping at a given temperature, say, T, is given by,

$$A_i = \nu_i \exp(-E_b(i)/k_bT), \tag{1.15}$$

where, k_b is the Boltzmann constant and ν is the typical vibrational frequency, given by,

$$\nu_i = \sqrt{\frac{2g_sE_d(i)}{\pi^2 m_i}}, \tag{1.16}$$

where, g_s is surface density of sites on a grain, m_i is the mass of the i-th species and $E_d(i)$ is the binding energy for desorption. The typical values of vibrational energies are in the range of 10^{12} - 10^{13} s^{-1}. If another atom is found during hopping, it will recombine and form a molecule. To find the formation rate one need to add rates of hopping for both the molecules.

If it does not find a partner within its desorption time, it will desorb. The desorption rate is given by,

$$W_i = \nu_i(i) \exp(-E_d(i)/k_bT). \tag{1.17}$$

Thermal desorption rate at 10 K is inadequate for most species, therefore, non thermal desorption due to UV photons and cosmic rays are very important.

Different regions of ISM shows different kind of chemical evolution. In the atomic diffuse clouds almost all species are in the atomic form except a small amount of H_2.

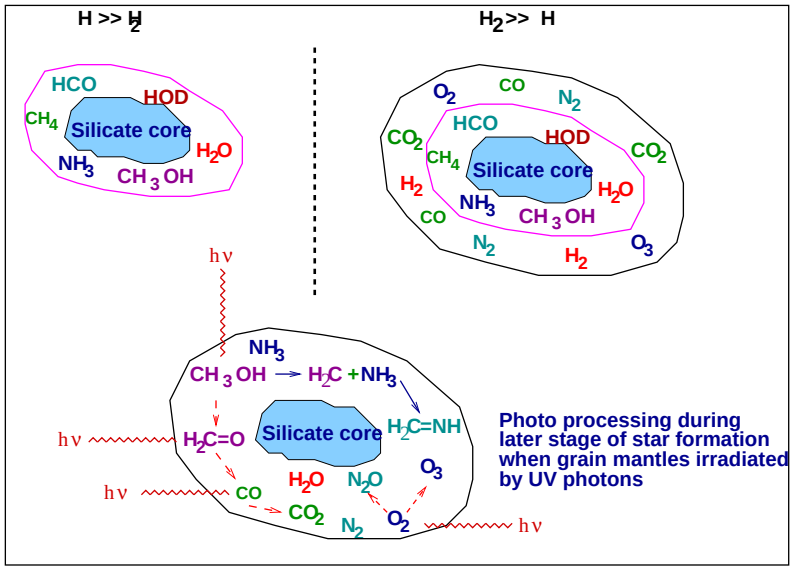

Figure 1.6: Physical processes that accruing on a grain surface

The chemistry in the diffuse clouds is mainly dominated by the low temperature gas phase reactions leading to the enhanced formation of small radicals and unsaturated molecules. In the dense clouds, many gaseous species accrete onto the grains. At low temperature, the chemistry on grains is mainly dominated by the hydrogenation reactions, since mobility of atomic-H is much higher than the other species. These ices are also processed by the ultraviolet photons, X-ray and cosmic rays i.e., energetic particles of the ISM. As these clouds begin to warm up and form disks around them which are called proto-planetary disks. The ices are heated and molecules are desorbed back into the gas phase, according to their desorption temperatures. These freshly evaporated molecules drive a rich chemistry in these regions. Here, the chemical processes are different from those in the cold regions. In particular, small saturated molecules such as NH_3, H_2O, CH_3OH, etc are far more abundant in these regions than the other regions. Fig. 1.6, schematically shows type of molecules that are formed on the grain surface when gas is rich atomic hydrogen, when it is rich in molecular hydrogen and finally in lower panel how UV radiation ionizes various species.

1.6 This thesis

This thesis presents studies on the formation of molecules with an emphasis on H_2 and water in a variety of astrophysical environments. Although H_2 is the simplest and most abundant molecule in the Universe its formation pathways at high temperature is not clear. Laboratory experiments can only explain H_2 formation between 6 and 10 K for olivine and between 9 and 15 K for amorphous carbon. However, H_2 formation is frequently observed at much elevated temperature. A major focus of this thesis is to address this issue. Water is another very important molecule which constitutes nearly 70 % of grain mantle. Its formation in the diffuse ISM was studied.

In the second chapter, first various methods to study the formation of molecules along with physical processes that are involved is discussed. Suitability of all the methods are also discussed. Through out thesis, Continuous Time Random Walk (CTRW) Monte Carlo method is used, although it is computationally, very intensive, but various astrophysical environment, especially, the low density regions requires that this method be used. In this chapter major emphasis is given to discuss CTRW Monte Carlo method and how it is implemented in our numerical simulation.

In the Chapter, 3, results of H_2 formation using CTRW Monte Carlo technique on the surface of interstellar dust grains with both physisorption and chemisorption sites on olivine and carbonaceous material are presented. In the standard approach, atoms must first enter the physisorption site before chemisorption can occur. Hydrogen atom mobility due to both thermal hopping and quantum mechanical tunneling is considered. The temperature range between 5 K and 825 K has been explored for different incoming H fluxes representative of interstellar environments with atomic hydrogen number density ranging between 0.1 cm^{-3} and 100 cm^{-3} and dust grain sizes ranging from 100 sites to 10^6 sites, the latter corresponding roughly to olivine grains of radius 0.2μm. Then rough

surfaces with multiple binding sites are considered. Then CTRW Monte Carlo results is compared to the standard rate equation approach. Finally, results in which chemisorption sites are entered directly and diffusion proceeds only to other chemisorption sites are presented.

In the Chapter 4, the formation of H_2 on the surfaces of interstellar dust grains in diffuse interstellar clouds using CTRW Monte Carlo method is studied. For this study, three different grain materials, olivine (a poly crystalline silicate), amorphous silicate, and amorphous carbon, as well as a grain temperature that depends on granular size is considered. In the diffuse clouds, grain temperature fluctuates due to interaction of ultra Violet photons with small grains. For some studies this temperature fluctuations is included. Results were presented for four different granular surfaces, one "flat" with one type of binding site due to physisorption, one "rough" with five different types of physisorption binding sites due to lateral forces, and two with sites for chemisorption, one in which a chemisorption site is entered by the first hydrogen atom via diffusion from a precursor physisorption site, and one in which chemisorption is direct but occurs with a barrier for the adsorption of the first hydrogen atom.

In the Chapter 5, we take the CTRW Monte Carlo approach to examine a much bigger network of molecules on the surface of dust grains in diffuse interstellar clouds. We consider H and O as accreting species on the dust grains and monitor their thermal motion on the surface and observe how they result in the production of H_2, OH, H_2O, H_2O_2, HO_2, O_2 and O_3. We consider temperature range upto 20K and various grain sizes to see the effect on chemical evolution. We show various results in mono-layer for H_2O formation and discuss other species whose productions are very low to even form a single mono-layer.

References

Bland-Hawthorn, J., Maloney, P. R., 1999, Astrophys. J., 510, L33

Cheung, A. C., Rank, D. M., Townes, C. H., Thornton, D. D., & Welch, W. J., 1968, Phys. Rev. Lett., 21, 1701

Cheung, A. C., Rank, D. M., Townes, C. H., Thornton, D. D., & Welch, W. J., 1969, Nature, 221, 626C

Chi, X., & Wolfendale, A. W., 1991, Journal of Physics G Nuclear Physics, 17, 987

Cox, P., Kruegel, E., & Mezger, P. G., 1986, A&A, 155, 380

Dunham, T., 1937, PASP, 49, 26D

Hollis, J. M., Pedelty, J. A., Snuder, L. E., Jewll, P. R., Lovas, F. J., Palmer, P., Liu, S. Y., 2003, ApJ, 588, 353H

Ioppolo, S., PhD thesis, 2010 Leiden University

Kaun, Y. J., Charnley, S. B., Huang, H. C., Tseng W. L. & Kisel, Z., 2003, ApJ, 593, 848

Mathis, J. S., Mezger, P., & Panagia, N., 1983, A&A, 128, 212, (MMP)

McKellar, A., 1940, PASP, 52, 87

Merrill, P. W., 1936, ApJ., 83, 126M

Muller, C. A., & Oort, J. H., 1951, Nature, 168, 357

Snow, T. P., & McCall, B. J., 2006, ARA&A, 44, 367S

Snyder, L. E., Buhl, D., Zuckerman, B., & Palmer, P., 1969, Phys. Rev. Lett., 22, 679

Strong, A. W., Moskalenko, I. V., & Reimer, O., 2000, 537, 763

Swings, P., & Rosenfeld, L., 1937, ApJ. 86, 483S

Tielens, A. G. G., 2005, The Physics and Chemistry of the Interstellar Medium (New York:Cambridge University Press)

van Dishoeck, E. F., & Black, J. H., 1989, ApJ, 340, 273

Weinreb, S., Barrett, A. H., Meeks, M. L., & Henry, J. C., 1963, Nature, 200, 829

Wilson, R. W., Jefferts, K. B., & Penzias, A. A., 1970, ApJL, 161, L43

Whittet, D. C. B., Schutte, W. A., Tielens, A. G. G. M., et al., A&A, 1996, 315, L357

2 Models to Study Formation of molecules in the in the ISM

2.1 Introduction

Detection of molecular species in the ISM using different observational techniques leads to study the route of its formation in the ISM. In last few decades, several models have been developed to study the formation of molecules in the ISM. These models are basically based on kinetics and/or simulations. This starts with the idea to explain the formation of the simplest molecule, that is molecular hydrogen. It was realized although H_2 is the simplest of all molecular species, its formation route on the gas phase is slow and insignificant. To explain H_2 formation, Gould & Salpeter (1963), introduced interstellar dusts as a catalyzing agent. In their three body theory of H_2 formation, it is assumed that interstellar dust grains act as catalyst in the formation of H_2 and it is formed on the surface of dust grains in the ISM. The catalytic effect of silicate and carbon grains in the formation of H_2 as been experimentally proved at low temperatures (Pirronello et al. (1997a, 1999); Manicò et al. (2001); Hornekær et al. (2003)). Since then several authors studied H_2 formation both theoretically (Gould

& Salpeter (1963); Williams (1968); Hollenbach & Salpeter (1970, 1971); Hollenbach et al. (1971); Smoluchowski (1981, 1983); Aronowitz & Chang (1985); Duley & Williams (1986); Pirronello & Averna (1988); Sandford & Allamandolla (1993); Takahashi et al. (1999); Farebrother et al. (1999)) and experimentally (Brackmann & Fite (1961); Schutte et al. (1976); Pirronello et al. (1997a,b, 1999); Manicò et al. (2001); Roser et al. (2002, 2003)). The understanding of different ways of H_2 formation in different regions of the ISM is a key for astronomers to understand the complex astrochemistry as H_2 plays a very important role in formation of more complex molecules and hence influences the chemical evolution of ISM (Duley & Williams (1984); Williams (1998)).

There are now several theoretical methods to study the surface chemistry that occurs on interstellar dust grains under a variety of astrophysical conditions. These approaches include the rate equation method, as well as several more detailed stochastic methods, based upon either the direction solution of the master equation or a Monte Carlo realization of this solution. In this chapter, I will try to explain few of the major chemical models, namely,

- Rate equation,
- Modified Rate equation
- Master equation and
- Continuous Time Random Walk Monte Carlo Simulation.

The earliest studies were done with the standard Rate equations used for diffusive reactions in surface science, which are based on average surface abundances, an approach most useful when there are large numbers of reactants on a given surface (Hasegawa et al. (1992); Biham et al. (2001)). Given that grains are small particles and that the interstellar medium is very dilute, the accretion rate of incoming species such as H atoms

onto grains will be very low. As a result, at any instant of time the average number of a species such as atomic H on a single grain surface can be less than unity and the surface population of reacting species can fluctuate widely, which leads to an overestimation of the rate of H_2 formation and the need for a stochastic approach (Charnley, Tielens & Rodgers (1997); Caselli, Hasegawa & Herbst (1998); Shalabiea, Caselli & Herbst (1998); Stantcheva, Caselli & Herbst (2001)). The departure from average values will be more severe for higher temperature, because the residence time for any atoms on grains will decrease significantly. Thus, at low flux and at high temperatures, the rate equation method is least likely to be successful. However, this method is very easy to implement and computationally less intensive.

Following work by Charnley (1998, 2001), Biham et al. (2001) and Green et al. (2001) proposed a direct master equation method independently and used it to study small systems of surface reactions: H_2 recombination for Biham et al. (2001) and H_2, O_2, and OH formation for Green et al. (2001). In the master equation approach, surface abundances are calculated using the time evolution of coupled probabilities and one has to solve a large number of equations, ideally infinite. Several authors have used the master equation approach for a smaller system of surface reactions because the surface equations can easily be coupled to rate equations for the gas-phase chemistry (Stantcheva, Caselli & Herbst (2001); Stantcheva & Herbst (2004); Acharyya et al. (2005)). Even so, approximations are needed to render the approach more tractable for large-scale calculations: these include using the master equation only for reactive surface species of small abundance (Stantcheva & Herbst (2004); Acharyya et al. (2005)) and using the method of moments (Barzel & Biham (2007)). Although method of moments, useful for H_2 formation Le Petit et al. (2009) and for larger systems of surface equations, the latter approximation is still under development for systems coupled to gas-phase chemistry because of mathematical instabilities. Recently, so-called hybrid methods

have been used to stabilize the moment equation approach (Du & Parise (2011)).

The other approach is the Monte Carlo method, which can be used to simulate the direct master equation method for probabilities of surface abundances, however, for gas-grain systems of reactions, it is very difficult to couple to rate equations for gas-phase chemistry. The difficulty has been solved by Vasyunin et al. (2009), who developed a method to solve both the gas-phase and surface chemistry simultaneously using the Monte Carlo approach. The approach is computer intensive, and it is still difficult to solve the equations for periods of greater than 1 Myr.

For smaller networks, such as the development of ice mantles or the formation of molecular hydrogen, a more detailed Monte Carlo approach, known as the Continuous Time Random Walk (CTRW) method, or more simply the kinetic Monte Carlo technique, is very useful (Chang, Cuppen & Herbst (2005)). The advantage of this "microscopic" technique is that it treats all atoms and molecules individually, and monitors their moves (accretion, hopping, desorption, recombination) on the grain surface, treated as a lattice of binding sites, in a continuous time frame, which removes the error due to fluctuations in the populations of the species (Chang, Cuppen & Herbst (2005); Cuppen & Herbst (2005); Cuppen et al. (2009)). In addition, the technique can be used for rough and even amorphous surfaces by assigning different energy parameters to individual sites, and can simulate several mechanisms of surface reactions besides the diffusive (Langmuir-Hinshelwood) one, including the Eley-Rideal mechanism, in which a gas-phase species lands directly on an adsorbate, and reactions within the gaps of porous ices. The technique has been used to look at the development of ice mantles Cuppen & Herbst (2007); Cuppen et al. (2009) and probe details of H_2 formation Cazaux et al. (2005); Cuppen, Morata & Herbest (2006); Herbst & Cuppen (2006). Chakrabarti et al. (2006) used a similar method that keeps track of each individual reactant and their movements and calculated the effective grain surface area involved in the forma-

tion of molecular hydrogen in interstellar clouds. Most recently, the kinetic Monte Carlo method has been used to study the very complex formation of H_2 on graphite, which involves preliminary dimer formation Cuppen & Hornekaer (2008); Gavardi et al. (2009). An astronomical application of H_2 formation in shocks, where the gas temperature is very high but the dust temperature quite low, has also been undertaken Cuppen et al. (2010).

This chapter is organized in the following way. First, I explain the laboratory experiments conducted to measure the rate of H_2 formation on the surface of dust grain having a rang of temperature. This will give an understanding of various rates. Which in turn will help to determine appropriate method to study it. Then I discussed rate equation approach and Master equation approach respectively. Finally, Continuous Time, Random Walk Monte Carlo simulations method is discussed.

2.2 Experimental work

Various experiments have been performed using ultra high-vacuum (UHV) chamber to create the typical ISM like condition in the laboratory, a series of experiments were performed to measure the rate of HD formation by the recombination of H and D atoms on the sample by irradiating the sample with two beams of H and D atoms and monitoring the HD produced during the experiment (Pirronello et al. (1997a,b, 1999)). In the above experiments two different substrates were used as samples which can be considered as close analog of interstellar dust grain: a natural olivine (a poly crystalline silicate containing Mg_2SiO_4 and Fe_2SiO_4) slab and an amorphous carbon sample. The substrate temperatures during the irradiation by H and D atoms were kept in the range between 5 and 15 K. The experiments were performed in two steps, in first step the sample was irradiated by the separate beams of H and D and in the second step which

is called the temperature-programmed desorption (TPD), the sample temperature was quickly ramped to over 30 K to desorb all weakly adsorbed H, D and HD. The rate of HD formation was measured using a quadrupole mass spectrometer both during irradiation and in the subsequent TPD experiment. To analyze the experimental results the rate equation method was used.

Table 2.1: Energy barriers for olivine and amorphous carbon

Substrate	E_0 (K)	E_1 (K)	E_2 (K)	μ
Olivine	287	373	314	0.33
Amorphous carbon	511	658	542	0.413

In this analysis the parameters of the rate equation (i.e. energy barriers for atomic hydrogen diffusion and desorption, the barrier for molecular hydrogen desorption, and the probability of spontaneous desorption of a hydrogen molecule upon recombination) were fitted to the experimental TPD curves. Using the values of the parameters that best fit the experimental results, the efficiency of hydrogen recombination on the olivine and amorphous carbon surfaces was calculated for ISM conditions using the same rate equation model. In the Table 2.1, these parameters are listed. These parameters are activation energy barriers for atomic hydrogen diffusion (E_0) and desorption (E_1), the barrier for molecular hydrogen desorption (E_2) and the probability of spontaneous desorption (μ) of a hydrogen molecule upon recombination. When these values are used, at 10 K, hopping time scale for H-atom is around 3 second, and desorption time scale is around 16000 seconds for H. However, accretion time scale is much larger ($\sim$ yrs), therefore at low densities, probability of having two H-atoms on a grain is low as a result rate equation approach will break down. This problem will be more severe as temperature is used since residence time will go down exponentially, where as accretion rate will not change much due to very weak temperature dependence. When efficiency

of H_2 formation is calculated using these parameters it is found that HD can efficient be formed within a small range of temperature (6-10 K for olivine and 12-17 K for amorphous carbon) under laboratory conditions which were tried to be kept similar to ISM in the best possible way.

2.3 Rate Equation Method

Let us consider a laboratory experiment in which a sample analogous to interstellar dust grain is being irradiated by a flux of H atoms. When H atoms come very close to the surface, they get adsorbed to the surface. This kind of adsorption is called physisorption. There is no chemical reaction between the substrate and the adsorbed H atom. Adsorbed H atoms are called adatoms.If the temperature of the sample is not very low ($< 5K$), these adsorbed H atoms perform random walk (hopping) on the surface of the substrate. The probability to walk in any possible direction is assumed to be same as it is a random process and there is no preferred direction. When two adatoms meet one another while doing their random walk they recombine and form one molecular hydrogen (H_2). This mechanism is called Langmuir-Hinshelwood (LH) Mechanism, schematically shown in the Fig. 2.1. Their is an another method in called Eley-Rideal (ER) Mechanism, in which, an atom interacts directly with an adsorbed species and forms a molecule. This mechanism is shown in the Fig. 2.2.

No all H adatoms find another adatoms to form H_2. Some adatom get enough energy to overcome the energy barrier and leave the surface, this process is called desorption of H atoms from the surface, Let $n_{\mathrm{H}}(t)$ (in monolayers [ML]) be the coverage of H atoms on the surface and $n_{\mathrm{H_2}}(t)$ (in ML) the coverage of H_2 molecules at any time t. We can write the following set of time dependent equations following LH mechanism called the

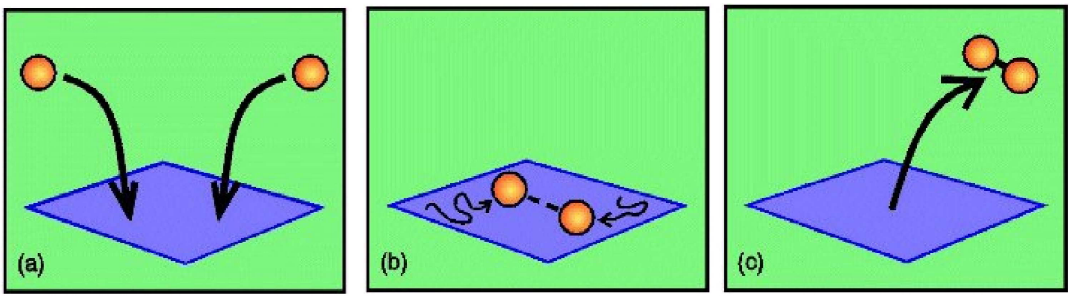

Figure 2.1: Langmuir-Hinshelwood Mechanism. (a) An atom adsorbs onto the surface. (b) Another atom passes by which interacts with the one on the surface and (c) A molecule is formed which desorbs.

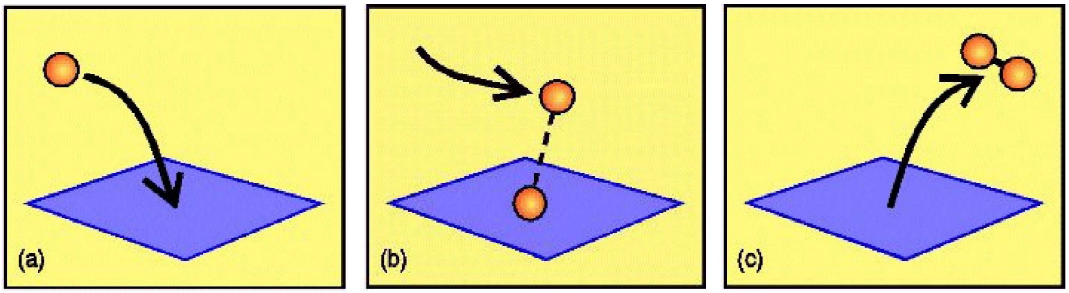

Figure 2.2: Eley-Rideal Mechanism. (a) Two atoms adsorb onto the surface. (b) They diffuse across the surface and interact when they are close and (c) A molecule is formed which desorbs.

rate equations for H_2 formation,

$$\frac{dn_{\mathrm{H}}}{dt} = f_{\mathrm{H}}(1 - n_{\mathrm{H}} - n_{\mathrm{H_2}}) - W_{\mathrm{H}} n_{\mathrm{H}} - 2a_{\mathrm{H}} n_{\mathrm{H}}^2, \tag{2.1}$$

$$\frac{dn_{\mathrm{H_2}}}{dt} = \mu a_{\mathrm{H}} n_H^2 - W_{\mathrm{H_2}} n_{\mathrm{H_2}}. \tag{2.2}$$

The Equation (2.1) gives the rate of change of coverage of H on the surface and the Equation (2.2) gives the same for H_2. The term in parentheses in the Equation (2.1) represents the Langmuir-Hinshelwood rejection term. In Langmuir-Hinshelwood (LH) scheme an H atom when it is deposited on the top of another H atom or H_2 already on the surface, is rejected. The effective flux of H atoms is represented by f_{H} (in units of ML s^{-1}). The second term in Equation (2.1) represents the desorption of H atoms from

the surface where W_{H} is called the desorption rate. The third term in Equation (2.1) is due to the decrease in population of H atoms on the surface by two when two adatoms recombines into H_2, a_{H} is called the hopping rate. The desorption rate and hopping rate are given respectively as,

$$W_{\mathrm{H}} = \nu \cdot \exp(-E_1/k_B T) \tag{2.3}$$

and

$$a_{\mathrm{H}} = \nu \cdot \exp(-E_0/k_B T), \tag{2.4}$$

where, ν is called the attempt rate (taken most commonly to be 10^{12} s^{-1}), E_1 and E_0 are respectively the activation energy barriers for desorption and hopping of an H atom, T is the temperature in K and k_B is the Boltzmann constant. Here in the above equations it is assumed that there is no barrier for recombination i.e. when ever two adatoms meet they always form H_2. The first term on the right hand side of Equation (2.2) accounts for the formation of H_2 molecules by the process of recombination of adatoms. The factor 2 in the third term of Equation (2.1) does not appear here since two H atoms are required to form one molecule of hydrogen. The parameter μ represents the fraction of H_2 that remains on the surface upon formation, while a fraction of $(1-\mu)$ is assumed to be released in the gaseous form spontaneously due to the excess energy released in the recombination process. The second term in Equation (2.2) is for the desorption of H_2 molecules adsorbed to the surface after formation. It is assumed that H_2 released from the surface never return back to the surface and hence there is no flux term for H_2 in the Equation (2.2). The desorption rate of H_2 is

$$W_{\mathrm{H_2}} = \nu \cdot \exp(-E_2/k_B T), \tag{2.5}$$

where, E_2 is the activation energy barrier for H_2 desorption. The rate $R_{\mathrm{H_2}}$ (in ML s^{-1})

of H_2 production can be written as

$$R_{H_2} = (1-\mu)a_H n_H^2 + W_{H_2} n_{H_2}. \tag{2.6}$$

The recombination efficiency (η) of H_2 formation in the steady state is given by

$$\eta = \frac{r_{H_2}}{f_H/2} \tag{2.7}$$

The recombination efficiency can be defined as the fraction of the H atoms that desorb in the form of H_2. In the steady state condition the value of η lies between 0 and 1.

One can solve the Equation (2.1) and Equation (2.2) for steady state condition by putting the left hand side of Equation (2.1) and Equation (2.2) equal to zero to obtain the coverage of H and H_2 in the steady state condition for a given temperature and a given flux. By putting the steady state coverage of H and H_2 in the Equation (2.6) the rate of H_2 formation can be obtained very easily. Keeping the value of R_{H_2} in the Equation (2.7) the value of η can be calculated. In the case of low coverage, we can neglect the LH rejection term in the Equation (2.1), so the steady state coverage of H and H_2 for the simplified case are respectively given by

$$n_H = \frac{-W_H + \sqrt{W_H^2 + 8a_H f_H}}{4a_H} \tag{2.8}$$

$$n_{H_2} = \frac{\mu}{8a_H W_{H_2}} \left(W_H^2 + 4a_H f_H - W_H \sqrt{W_H^2 + 8a_H f_H} \right). \tag{2.9}$$

The rate equation model described by Equation (2.1) and Equation (2.2) was used by Katz et al. (1999) to analyze the results of laboratory experiments (Pirronello et al. (1997a,b, 1999)).

The rate equation results also show that the efficiency of H_2 formation is high only between a small range of temperature (between 6-9 K for olivine and 12 - 16 K for amorphous carbon). The rate equation is good to use when the coverage of H on the surface is not very low as the computing efficiency is very high but when the coverage of H atom is very low that is the case when dust grain is very small or hydrogen flux is weak, or at high temperature the rate equation over estimates the rate of H_2 formation as the rate equation model takes into account only the average densities and ignores the discrete nature of H atoms on the surface and the fluctuations (Charnley, Tielens & Rodgers (1997); Caselli, Hasegawa & Herbst (1998); Shalabiea, Caselli & Herbst (1998); Stantcheva, Caselli & Herbst (2001)) which becomes dominant for very low coverage. Hence the rate equation model can not be applied to the regions of the ISM where the number density of H atom is very low resulting in a very weak flux of H atoms or the grain radius is very small.

2.3.1 Rate equations with chemisorption sites

Cazaux & Tielens (2004) used Rate equations for surface with both physisorption and chemisorption sites, that is surface with two kind of potential wells. Their modified Rate equations with the time evolution in units of fractional monolayers for physisorbed hydrogen atoms ($\dot{\mathrm{H}}_P$), chemisorbed hydrogen atoms ($\dot{\mathrm{H}}_C$) and molecular hydrogen ($\dot{\mathrm{H}}_2$) are as follows:

$$\dot{\mathrm{H}}_P = F(1-\mathrm{H}_P-\mathrm{H}_2) - \alpha_{pc}\mathrm{H}_P - 2\alpha_{pp}\mathrm{H}_P^2 + \alpha_{cp}\mathrm{H}_C(1-\mathrm{H}_P) - \beta_{\mathrm{H}_P}\mathrm{H}_P \quad (2.10)$$

$$\dot{\mathrm{H}}_C = \alpha_{pc}\mathrm{H}_P(1-\mathrm{H}_C) - \alpha_{pc}\mathrm{H}_P\mathrm{H}_C - \alpha_{cp}\mathrm{H}_C - 2\alpha_{cc}\mathrm{H}_C^2 - \beta_{\mathrm{H}_C}\mathrm{H}_C \quad (2.11)$$

$$\dot{\mathrm{H}}_2 = \mu(2\alpha_{pp}\mathrm{H}_P^2 + \alpha_{pc}\mathrm{H}_P\mathrm{H}_C + \alpha_{cp}\mathrm{H}_C\mathrm{H}_P + \alpha_{cc}\mathrm{H}_C^2) - \beta_{\mathrm{H}_2}\mathrm{H}_2 \quad (2.12)$$

where, α_{pp} is mobility from physisorption to physisorption site, α_{pc} is mobility from physisorption to chemisorption site, α_{cc} is mobility from chemisorption to chemisorption site and α_{cp} is mobility from chemisorption to physisorption site. $\beta_{\mathrm{H}_P}, \beta_{\mathrm{H}_C}$ and β_{H_2} are corresponding desorption rates for physisorbed H, chemisorbed H and H_2 respectively. Cazaux & Tielens (2004) wrote the simplified equation for efficiency of H_2 production as

$$\epsilon_{\mathrm{H}_2} = \left(1 + \frac{\mu F}{2\beta_{\mathrm{H}_2}} + \frac{\beta_{\mathrm{H}_P}}{\alpha_{pc}}\right)^{-1} \xi \tag{2.13}$$

where,

$$\xi = \left(1 + \frac{\nu_{\mathrm{H}_C}}{2F} \exp\left(-\frac{1.5E_{\mathrm{H}_C}}{kT}\right)\left(1 + \sqrt{\frac{E_{\mathrm{H}_C} - E_S}{E_{\mathrm{H}_P} - E_S}}\right)^2\right)^{-1} \tag{2.14}$$

and

$$\begin{aligned} \alpha_{pc} &= 8\sqrt{\pi T}\nu_{\mathrm{H}_p} \frac{\sqrt{E_{\mathrm{H}_C} - E_{\mathrm{H}_P}}}{E_{\mathrm{H}_C} - E_S} \exp\left(-2a\frac{\sqrt{2m_{\mathrm{H}}k_B(E_{\mathrm{H}_P} - E_s)}}{\hbar}\right) \\ &+ 4\nu_{\mathrm{H}_P}\sqrt{\frac{E_{\mathrm{H}_P} - E_S}{E_{\mathrm{H}_C} - E_S}} \exp\left(\frac{-(E_{\mathrm{H}_P} - E_S)}{T}\right) \end{aligned} \tag{2.15}$$

Rate equation method results is compared with CTRW Monte Carlo results to find the difference. Since Rate equation method is computationally fast, it is important to know the regime for which these method is applicable for effective use of the computer resources.

2.4 Master Equation Method

Rate equation fails to give the correct results in the limit of low flux and small grain radius which is quite expected in the various regions in the ISM. So, in such cases where the coverage is expected to be very low due to high temperature or very low flux or

the grain size is so small that the population of adatoms on the surface is too low then the approach of Master equation model (Biham et al. (2001)) could be used. Master equation model uses the probability to calculate the number of adatoms on the surface instead of average number of adatoms.

In this approach, Biham et al. (2001) considered a grain exposed to a flux of H atoms. The probability that there are $N_{\rm H}$ hydrogen atoms on the grain surface is given by $P_{\rm H}(N_{\rm H})$, where, $N_{\rm H} = 0, 1, 2, \ldots, S$, and

$$\sum_{N_{\rm H}=0}^{\infty} P_{\rm H}(N_{\rm H}) = 1. \tag{2.16}$$

Biham et al. (2001) gave a set of equations that give the time derivatives of these probabilities, these equations are called Master Equations. Basically, it is a set of coupled linear differential equations of the form,

$$\begin{aligned} \dot{P}_{\rm H}(N_{\rm H}) &= F_{\rm H}\left[P_{\rm H}(N_{\rm H}-1) - P_{\rm H}(N_{\rm H})\right] \\ &+ W_{\rm H}\left[(N_{\rm H}+1)P_{\rm H}(N_{\rm H}+1) - N_{\rm H}P_{\rm H}(N_{\rm H})\right] \\ &+ A_{\rm H}\left[(N_{\rm H}+2)(N_{\rm H}+1)P_{\rm H}(N_{\rm H}+2) - N_{\rm H}(N_{\rm H}-1)P_{\rm H}(N_{\rm H})\right]. \end{aligned} \tag{2.17}$$

Thus for $N_{\rm H} = 0, 1, 2, ...$, we have,

$$
\begin{aligned}
\dot{P}_{\rm H}(0) &= -F_{\rm H}P_{\rm H}(0) + W_{\rm H}P_{\rm H}(1) + 2\cdot 1\cdot A_{\rm H}P_{\rm H}(2), \\
\dot{P}_{\rm H}(1) &= F_{\rm H}\left[P_{\rm H}(0) - P_{\rm H}(1)\right] + W_{\rm H}\left[2P_{\rm H}(2) - P_{\rm H}(1)\right] + 3\cdot 2\cdot A_{\rm H}P_{\rm H}(3), \\
\dot{P}_{\rm H}(2) &= F_{\rm H}\left[P_{\rm H}(1) - P_{\rm H}(2)\right] + W_{\rm H}\left[3P_{\rm H}(3) - 2P_{\rm H}(2)\right], \\
&+ A_{\rm H}\left[4\cdot 3\cdot P_{\rm H}(4) - 2\cdot 1\cdot P_{\rm H}(2)\right], \\
&\vdots \\
\dot{P}_{\rm H}(N_{\rm H}) &= F_{\rm H}\left[P_{\rm H}(N_{\rm H}-1) - P_{\rm H}(N_{\rm H})\right] \\
&+ W_{\rm H}\left[(N_{\rm H}+1)P_{\rm H}(N_{\rm H}+1) - N_{\rm H}P_{\rm H}(N_{\rm H})\right] \\
&+ A_{\rm H}\left[(N_{\rm H}+2)(N_{\rm H}+1)P_{\rm H}(N_{\rm H}+2) - N_{\rm H}(N_{\rm H}-1)P_{\rm H}(N_{\rm H})\right] \\
&\vdots
\end{aligned}
$$

Each equation includes three terms. The first term describes the effect of the incoming flux $F_{\rm H}$. The probability $P_{\rm H}(N_{\rm H})$ increases when an H atom is adsorbed on a grain that already has $N_{\rm H}-1$ adsorbed atoms at a rate of $[F_{\rm H}P_{\rm H}(N_{\rm H}-1)]$, and decreases when a new atom is adsorbed on a grain with $N_{\rm H}$ atoms on it at a rate of $[F_{\rm H}P_{\rm H}(N_{\rm H})]$. The second term includes the effect of desorption. An H atom that is desorbed from a grain with $N_{\rm H}$ atoms, decreases the probability $P_{\rm H}(N_{\rm H})$ at a rate of $[N_{\rm H}W_{\rm H}P_{\rm H}(N_{\rm H})]$, and increases the probability $P_{\rm H}(N_{\rm H}-1)$ at the same rate. The third term describes the effect of H_2 formation. The production of one molecule reduces the number of H atoms on the surface from $N_{\rm H}$ to $N_{\rm H}-2$. For one pair of H atoms the recombination rate is proportional to the sweeping rate $A_{\rm H}$ multiplied by 2 since both atoms are mobile simultaneously. This rate is multiplied by the number of possible pairs of atoms, namely $N_{\rm H}(N_{\rm H}-1)/2$. Note that the equations for $\dot{P}_{\rm H}(0)$ and$\dot{P}_{\rm H}(1)$ do not include all the terms, because at least one H atom is required for desorption to occur and at least two

for recombination. The rate of formation of H_2 molecules on a single grain, $R_{H_2}^{grain}$ (cm^{-3} s^{-1}), is thus given by,

$$R_{H_2}^{grain} = A_H[\langle N_H^2\rangle - \langle N_H\rangle], \tag{2.18}$$

where,

$$\langle N_H^k\rangle = \sum_{N_H=0}^{\infty} N_H^k P_H(N_H), \tag{2.19}$$

is the kth moment of the distribution $P_H(N_H)$. The probability that there are N_{H_2} hydrogen molecules on the grain is given by $P_{H_2}(N_{H_2})$ and the time evolution of these probabilities is given by,

$$\begin{aligned}
\dot{P}_{H_2}(0) &= -F_{H_2}P_{H_2}(0) + W_{H_2}P_{H_2}(1) - \mu R_{H_2}P_{H_2}(0),\\
\dot{P}_{H_2}(1) &= F_{H_2}\left[P_{H_2}(0) - P_{H_2}(1)\right] + W_{H_2}\left[2P_{H_2}(2) - P_{H_2}(1)\right]\\
&+ \mu R_{H_2}\left[P_{H_2}(0) - P_{H_2}(1)\right],\\
\dot{P}_{H_2}(2) &= F_{H_2}\left[P_{H_2}(1) - P_{H_2}(2)\right] + W_{H_2}\left[3P_{H_2}(3) - 2P_{H_2}(2)\right]\\
&+ \mu R_{H_2}\left[P_{H_2}(1) - P_{H_2}(2)\right],\\
&\vdots\\
\dot{P}_{H_2}(N_{H_2}) &= F_{H_2}\left[P_{H_2}(N_{H_2}-1) - P_{H_2}(N_{H_2})\right]\\
&+ W_{H_2}\left[(N_{H_2}+1)P_{H_2}(N_{H_2}+1) - N_{H_2}P_{H_2}(N_{H_2})\right]\\
&+ \mu R_{H_2}\left[P_{H_2}(N_{H_2}-1) - P_{H_2}(N_{H_2})\right].\\
&\vdots
\end{aligned} \tag{2.20}$$

where, F_{H_2} (molecules s^{-1}) is the flux of H_2 molecules that stick on the grain surface, W_{H_2} is the desorption rate of molecules from the surface (which is inversely proportional to their residence time, namely $t_{H_2} = 1/W_{H_2}$). Each of these equations includes three terms, describing the effects of an incoming H_2 flux, desorption and recombination,

respectively.

The time dependence of $R_{H_2}^{grain}$ can be obtained by numerically integrating Equation (2.18) using a standard Runge-Kutta method. For the case of steady state, namely $\dot{P}_H(N_H) = 0$ for all N_H, an analytical solution for $P_H(N_H)$ was obtained, in terms of A_H/W_H and W_H/F_H (Biham and Lipshtat (2002)). The rate of formation of H_2 molecules on a single grain with S adsorption sites is given by (Biham and Lipshtat (2002)),

$$R_{H_2}^{grain} = \frac{F_H}{2} \frac{I_{W_H/A_H+1}\left(2\sqrt{2F_H/A_H}\right)}{I_{W_H/A_H-1}\left(2\sqrt{2F_H/A_H}\right)}, \tag{2.21}$$

where, $I_x(y)$ is the modified Bessel function. The recombination efficiency of H atoms to form H_2 is given by,

$$\eta = \frac{R_{H_2}}{(F_H/2)}. \tag{2.22}$$

Master equations gives better results compared to Rate equations methods but is far more complex and needs more computing power. When we need to apply Master equation for a complex network of molecules than above written equations become more complex. When studying the formation of H_2 only, we have to write only two sets of equations as shown above one set for each of H and H_2, similarly while studying a complex network say for example a network of X number of atoms and molecules then we need to write a set of X equations and number of terms in each equations may be more than three depending on the considered chemical route for the formation of molecules. Proper care is needed that all terms are written correctly in all the equations.

2.5 Monte Carlo Simulation

In recent years, Continuous Time Random Walk (CTRW) Monte Carlo simulation technique is developed to simulate the formation of different molecules on the surface of the dust grains in the ISM. Chang, Cuppen & Herbst (2005) applied CTRW Monte Carlo simulation technique to study the formation of hydrogen molecule on the surface of the interstellar dust grains and compared the results with that of rate equation method. In the simulation, incoming atoms are deposited on a grain lattice. Depending upon the model, one can consider physisorption well, or chemisorption well or both physisorption and chemisorption well for the adsorption of incoming atoms. Following the analysis of Katz et al. (1999), it is assumed that these adatoms "hop" from site to site when they have enough energy to overcome a barrier against classical diffusion, a process known as "thermal activation". Chang, Cuppen & Herbst (2005) ignored quantum mechanical tunneling of H atom from one site to other site but for a more realistic simulation, tunneling from site to site may also be considered.

The advantage of this technique is that instead of using average densities of the species on the surface of the dust grains for calculation, it treats every adatoms and molecules individually and monitors their moves (hopping, desorption, recombination etc) on the grain surface in a continuous time frame. Which removes the error due to fluctuations in the population of the species which become dominant in the case of low flux, high temperature and for small grains. This feature of simulation to monitor each event separately makes the model work with equal efficiency for all possible conditions one can expect in the ISM and makes the model a universal technique. However, it requires much greater computing power compared to Rate equation method or even Master equation method and for a complex system it may require simplified approximations to get the result within meaningful time. However with increasing computing power it is

possible to use CTRW Monte Carlo simulation to study the role of dust grains in the formation of molecules in the ISM under different conditions.

2.5.1 Model

For simplicity, let us again consider the formation of H_2 on the surface of dust rains. In the CTRW Monte Carlo simulation technique, grains surface is considered as a mesh of lattice points. Each lattice site is an adsorption site for incoming H atoms. H atoms are deposited on this grain lattice at random time intervals depending on the waiting time which is calculated using the flux of H atoms in the gas phase. An adsorbed H atom can hop to any of its neighboring site with equal probability. In the process if H-atom meets an another H atom it forms H_2. A fraction $1-\mu$ (where, μ represents the fraction of H_2 molecules that are not ejected immediately due to formation heat, but remain on the grain until they desorb from the surface) of the formed H_2 is instantly released in the gas phase while remaining are adsorbed to the surface and desorbed later. Analyzing experimental TPD data for olivine and amorphous carbon Katz et al. (1999), found a non-zero value for the parameter μ.

In our model, we assumed μ to be zero in most of the cases as the assumption that $\mu = 0$ is not important because, except at very low temperatures, H_2 will evaporate quickly if not immediately ejected, so for low temperature simulation one can not neglect non zero value of μ. Generally, the deposition of additional H_2 molecules from space is neglected since H_2 does not constitute a dominant fraction of the gas phase in the environments under simulation. In addition, H_2 does not efficiently stick to the surface even at very low temperature ($\sim$ 10 K). Since accretion time scale is much larger than the desorption time scale, many H-adatoms will desorb back in to the gas phase before recombination. This will become more severe as temperature is increased.

Several earlier studies (Chang, Cuppen & Herbst (2005); Cuppen & Herbst (2005); Chang, Cuppen & Herbst (2006); Cuppen, Morata & Herbest (2006)) neglected mobility due to quantum mechanical tunneling from site to site. However, we considered both hopping and tunneling and compared these results. Since our goal is study at higher temperatures we considered both physisorption and chemisorption sites. In one class of models an incoming H atom is first given a physisorption site to adsorb and then it can hop to a neighboring site which may be a physisorption or chemisorption site depending on the transmission coefficients (T_{ij}) (Cazaux & Tielens (2004)). Following Cazaux & Tielens (2010), transmission coefficients (T_{ij}) from site i to site j by tunneling is given by,

$$T_{ij}^{(1)} = 4\sqrt{\frac{E-B_{ij}}{E}}\left(\left(1+\sqrt{\frac{E-B_{ij}}{E}}\right)^2 + \frac{B_iB_j\left(\sinh\sqrt{\frac{2m(B_i-E)}{\hbar^2}}Z\right)^2}{(B_i-E)(E)}\right)^{-1}, \text{ if } E<B_i \tag{2.23}$$

and for diffusion it is given by,

$$T_{ij}^{(2)} = 4\sqrt{\frac{E-B_{ij}}{E}}\left(\left(1+\sqrt{\frac{E-B_{ij}}{E}}\right)^2 - \frac{B_iB_j\left(\sin\sqrt{\frac{2m(E-B_i)}{\hbar^2}}Z\right)^2}{(B_i-E)(E)}\right)^{-1}, \text{ if } E>B_i \tag{2.24}$$

where, Z is the width of the barrier, B_{ij} is the energy of the barrier between site i and site j, B_i is the energy of the barrier between two i sites, and B_j is the energy of the barrier between two j sites. Expressions for these energies used in the simulation are summarized in Table 2.2.

We integrate transmission coefficients numerically over the energies available to the

Table 2.2: Expressions for parameters used to calculate transmission coefficients to go from site i to site j(Cazaux & Tielens (2010)).

T_{ij}	B_i	B_j	B_{ij}	Z
T_{PP}	$E_P(k) - E_{SP}$	$E_P(k) - E_{SP}$	0	A
T_{CC}	$E_C(k) - E_{SC}$	$E_C(k) - E_{SC}$	0	A
T_{PC}	$E_P(k) - E_S$	$E_C(k) - E_S$	$E_P(k) - E_C(k)$	a
T_{CP}	$E_C(k) - E_S$	$E_P(k) - E_S$	$E_P(k) - E_C(k)$	a

adatom to obtain the different probabilities to go from one site to another site. The probability to go from site i to site j is given by

$$P_{ij} = \frac{1}{kT}\int_0^{B_i} \exp\left(-\frac{E}{kT}\right) T_{ij}^{(1)}\, dE + \frac{1}{kT}\int_{B_i}^{\infty} \exp\left(-\frac{E}{kT}\right) T_{ij}^{(2)}\, dE, \tag{2.25}$$

where, T is the dust/surface temperature and E is the energy of the particle. The hopping rate or mobility of the adatom can be calculated by multiplying P_{ij} with the attempt rate (ν_i) corresponding to site i or j, ν_i is given by the following equation,

$$\nu_i = \sqrt{\frac{2n_s E_l}{\pi^2 m}}, \tag{2.26}$$

Here, E_l is the depth of the well to which the species is bounded at the site i, m is the mass of the adatom, and $n_s = 5 \times 10^{13}$ cm^{-2} for amorphous carbon and 2×10^{14} cm^{-2} for olivine (Biham et al., 2001). So following processes take place during the simulation of H_2 formation,

- The accretion of H atom on the grain surface (accretion of H_2 is rejected in LH mechanism).
- Hopping of adatoms from one site to another neighbor site.
- Desorption of adatoms from the surface.

- Formation of H_2.
- Desorption of H_2.

Accretion of H atoms on the surface of dust grain is calculated using the flux of H atoms in the gas phase. The flux or deposition rate ($R_{\rm H}$) of H atom on the grain surface in the unit of atom per second is given by

$$R_{\rm H} = \sigma_{gr}\ \upsilon_{\rm H}\ n_{\rm H} \tag{2.27}$$

where, σ_{gr} is the cross section of the dust grain, $n_{\rm H}$ and $\upsilon_{\rm H}$ are respectively the number density and average velocity of H atoms in the gas phase. Here, sticking coefficient is assumed to be 1. The expression for υ_H is given by,

$$\upsilon_{\rm H} = \sqrt{\frac{8\ k\ T_{gas}}{\pi\ m}} \tag{2.28}$$

where, m is the mass of H atom and T_{gas} the temperature of the hydrogen gas. Deposition, hopping, and desorption are all Poisson processes, which means that they are memory-less, or Markovian. For such a memory-less or Poisson process the time interval t between two consecutive events follows an exponential distribution given by the following expression,

$$\psi_\lambda(t) = \frac{\exp(-b_\lambda t)}{b_\lambda^{-1}}, \tag{2.29}$$

where, b_λ^{-1} is the average time between consecutive events λ and its inverse b_λ is the rate of process λ. Waiting times WT_λ is calculated according to the following expression by calling random numbers,

$$WT_\lambda = -\frac{\ln\ X}{b_\lambda}, \tag{2.30}$$

where, X is a random number, $0 < X < 1$.

For deposition, which one can labeled as process $0, b_0 = t_0^{-1}$ is the deposition rate of H atoms (in units of atoms s^{-1}) and t_0 is the average deposition time. Similarly, for hopping (process 1), b_1 is the hopping rate. Following Cazaux & Tielens (2004), in our model we used Equation 2.25 and Equation 2.26 to calculate the hopping rate. The hopping rate is similar to as described for Rate equation and Master equation approaches, and given by,

$$b_1 = \nu \; exp(-E_b/T), \tag{2.31}$$

where, E_b (in units of K) is the diffusion barrier, Desorption is considered to be another independent Poisson process, (Chang, Cuppen & Herbst (2005)) considered same kind of waiting-time distribution for desorption also, thus for a single desorption energy, desorption rate (b_2)is given by,

$$b_2 = \nu \; exp(-E_D/T) \tag{2.32}$$

where, E_D is the desorption energy. If hopping and desorption are independent, the distributions can be multiplied and re-normalized to obtain a total waiting-time distribution for desorption and hopping of the form (Chang, Cuppen & Herbst (2005)),

$$\psi(t) = b \; exp(-bt), \tag{2.33}$$

with a total rate given by,

$$b = b_1 + b_2. \tag{2.34}$$

This total rate is used to calculate when the adsorbed H atom will make its next move, that is hooping or desorption. Following Chang, Cuppen & Herbst (2005), the competition between desorption and hopping can then easily be simulated by comparing the

ratio of an individual rate of Hopping and desorption to the total rate, that is comparing $(b_2)/(b_1+b_2)$ with a random number X. If X is smaller than the ratio, then the H atom will undergo desorption, otherwise it will hop to another neighbor site. A schematic diagram of the various steps is shown in the Figure 2.3.

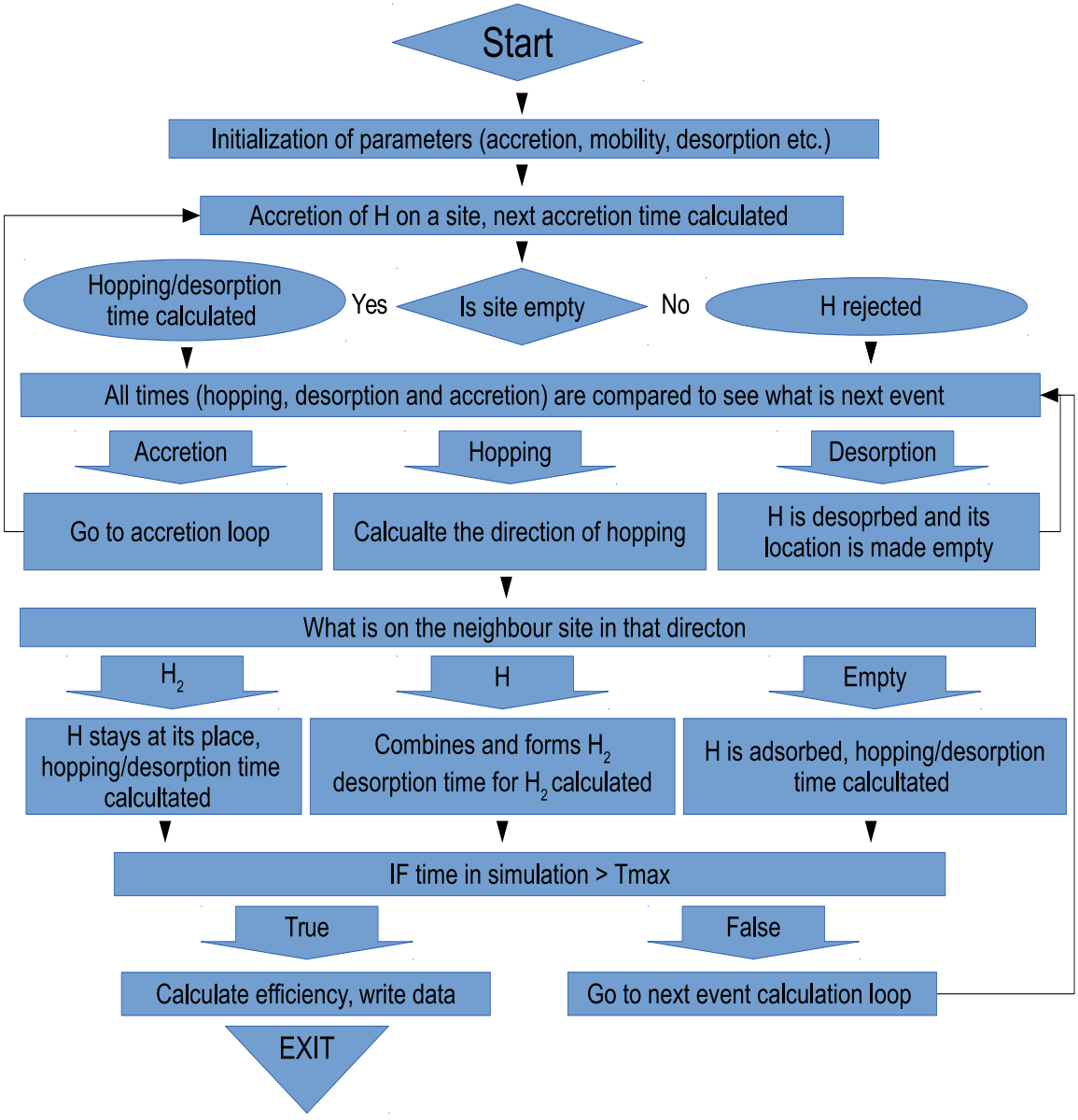

Figure 2.3: A schematic of various steps in Monte Carlo study of H_2 formation.

For all H atoms on the surface, the time at which they will make their next move,

either hopping or desorption, is determined as described above. In addition, the next time at which a deposition occurs is similarly determined. All these waiting times are compared after each event (accretion, hopping or desorption) and the processes are evaluated in the order of next occurrence.

Whenever a hydrogen atom hops to another site or a new hydrogen atom arrives on the lattice, a new waiting time is generated for its next move. The actual clock time at which the move occurs is the current time plus the waiting time. Incoming H atoms are assigned random sites (which is determined by generating a random number), and if there are H atoms already on the sites, the landing species will be bounced of (Chang, Cuppen & Herbst (2005)). This effect corresponds to the Langmuir-Hinshelwood rejection term in rate equations. Following Chang, Cuppen & Herbst (2005), we assumed the sticking probability to be unity, which means that all incoming H atoms stick to the surface if they get empty site. Whenever an H atom arrives, the arrival time for the next H atom is generated randomly from the distribution $\psi_0(t)$.

In the simulation, we use square lattices, in reality, dust grains are spherical in shape. To account for that, periodic boundary conditions is used, that is when an H atoms leaves from any direction of the lattice mesh, it enters back from the opposite side of the lattice mesh. The periodic boundary conditions are reasonable for grain surfaces because an H atom can always come back to where it started hopping by proceeding straight in a given direction. A schematic diagram of how periodic boundary condition is used for square lattice is shown in the Figure 2.4. After running simulation for some time, a quasi steady-state condition is reached in which the surface population of H atoms fluctuates around a constant value. The time to reach steady-state varies with parameters used during the simulation. Generally it ranges from 10^3 - 10^9 s. After steady state has been reached, we keep a continuous count of the number of arriving H atoms, $N_{\rm H}$, and the number of H_2 molecules formed, $N_{\rm H_2}$, after running for sufficiently long

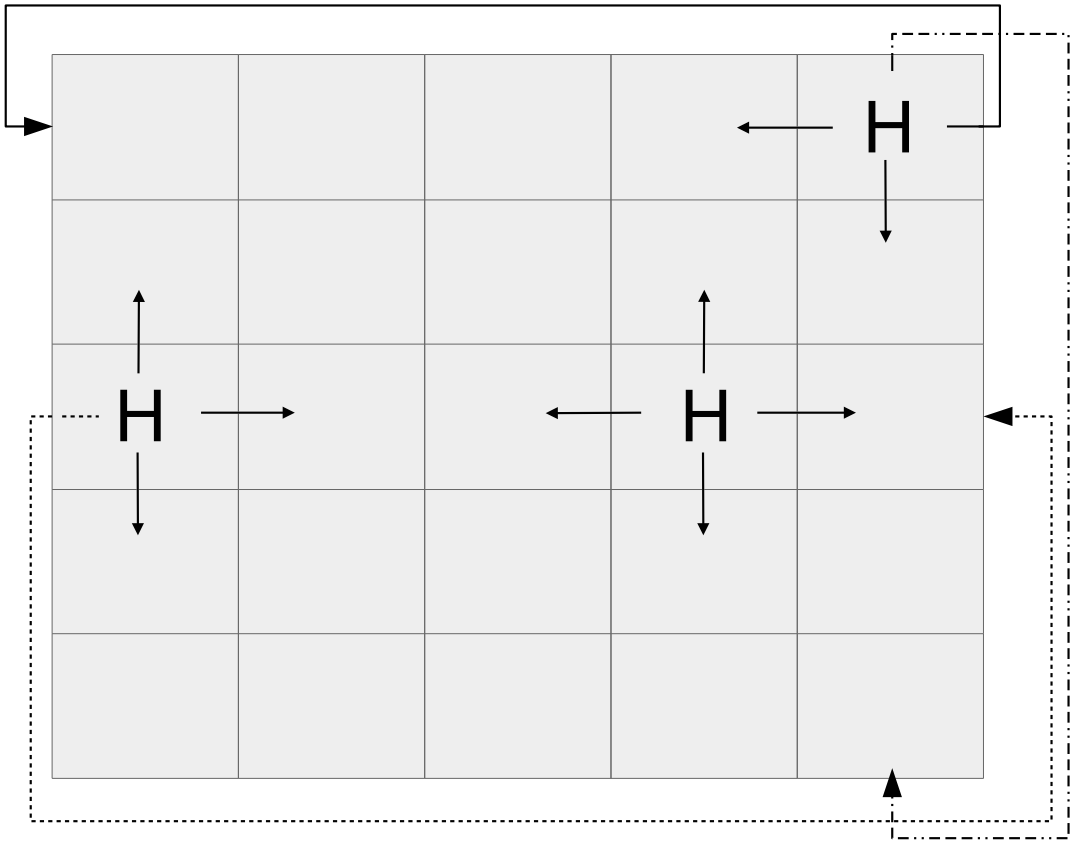

Figure 2.4: A schematic diagram showing mobility of H in different directions and boundary condition.

time in steady-state condition, recombination efficiency η is calculated by the following expression,

$$\eta = \frac{2N_{\mathrm{H_2}}}{N_{\mathrm{H}}}. \tag{2.35}$$

2.5.2 Study of formation of bigger molecules using Monte Carlo Simulation

Like Rate equation and Master equation approaches, Monte Carlo simulation can also be applied to study the bigger chemical network on the interstellar dust grains. In such cases, we need accretion rates of all incoming atoms and also different energy values of

all the atoms and molecules to calculate their hopping and desorption rates. Generally, at low temperatures, bigger and heavier molecules do not hop or desorb and remain motionless at the place of their formation while lighter atoms and molecules move and desorb from the surface as explained earlier. This causes formation of ices on the surface of dust grains. This makes the system a multi-layer system, in which atoms or molecules are deposited over ice layers of other atoms or molecules. In this an atom or molecule can move up or down in between the layers. A complete route of different possible reactions need to be implemented. With all added complexity in the code the simulation is generally run for about 10^5 to 10^6 years. After which total number of different molecules formed are calculated and converted to number of monolayers formed. The detail of this is explained in the chapter 5.

2.6 Other aspects of study

In most of our calculations we considered plain flat surface lattice. However, interstellar grains could be rough, thereby, binding energy on these surfaces could be high. In some of our calculations we studied this aspect. We introduced roughness by introducing lateral bonds following Cuppen & Herbst (2005). Since we took square lattice with each site having four neighbors, thus each adsorption site can have maximum four lateral bonds. This gives us five different sets of these energies which can be expressed by the equations,

$$E_1(i,j) = E_1 + nE_L(i,j) \tag{2.36}$$

and

$$E_2(i,j) = E_2 + nE_L(i,j) \tag{2.37}$$

where (i, j) is the index that indicates different binding sites and E_L is the energy of a so-called lateral bond, which arises due to imperfection in surface. The index n can be 0 - 4, corresponding to the number of lateral bonds existing at site (i, j). For our rough surface, we assume that 60% of the sites on a granular surface are flat ($n = 0$), while 10% of sites have each of the other values of the index. The different sites are randomly distributed across the surface. The value of E_L was taken as 30% of the desorption energy (E_2). Thus, atoms binds more strongly in rough surfaces. Figure 2.5 shows such a rough surface, darker site means more lateral bonds.

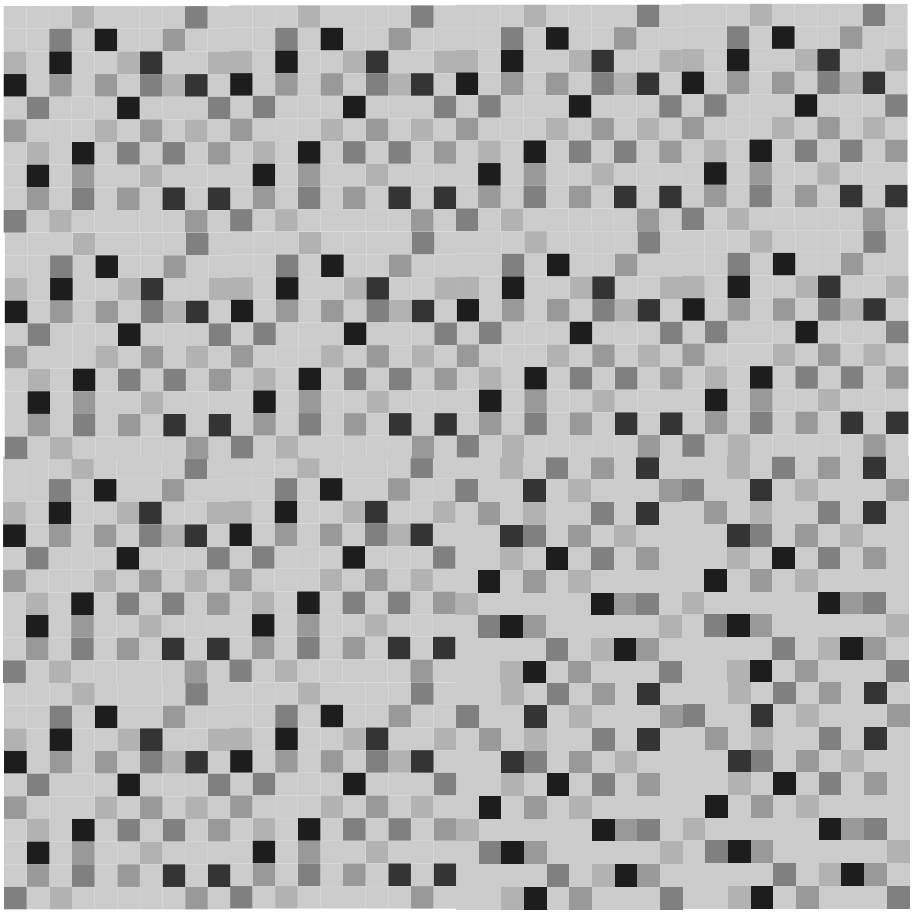

Figure 2.5: A representation of rough surface, darker sides means more lateral bond.

References

Acharyya, K., Chakrabarti, S. K., & Chakrabarti, S., 2005, MNRAS, 361, 550.

Aronowitz, S., & Chang, S., 1985, ApJ, 293, 243.

Barzel, B., & Biham, O., 2007, J. Chem. Phys., 127, 144703.

Biham, O., Furman, I., Pirronello, V., & Vidali, G., 2001, ApJ., 553, 595.

Biham, O., & Lipshtat, A., 2002, Phys. Rev. E, 66, 05610

Brackmann, R.T., & Fite, W.L., 1961, J. Chem. Phys., 34, 1572.

Caselli, P., Hasegawa, T.I., & Herbst, E., 1998, ApJ, 495, 309.

Cazaux, S., & Tielens, A. G. G. M., 2004, ApJ, 604, 222.

Cazaux, S., & Tielens, A. G. G. M. 2010, ApJ, 715, 698

Cazaux, S., Caselli, P., Tielens, A. G. G. M., Le Bourlot, J., & Walmsley, M. 2005, J. Phys. Conf, Proc., 6, 155

Chakrabarti, S.K., Das, A., Acharyya, K., & Chakrabarti, S., 2006, A&A, 457, 167

Chang, Q., Cuppen, H.M., & Herbst, E., 2005, A&A, 434, 599.

Chang, Q., Cuppen, H.M., & Herbst, E., 2006, A&A, 458, 497.

Charnley, S. B. 1998, ApJ, 509, L121

Charnley, S. B. 2001, ApJ, 562, L99

Charnley, S.B., Tielens, A.G.G.M., & Rodgers, S.D., 1997, ApJ, 482, L203.

Cuppen, H. M., & Herbst, E., 2005, MNRAS, 361, 565.

Cuppen, H. M., Morata, O., & Herbst, E., 2006, MNRAS, 367

Cuppen, H. M., & Herbst, E. 2007, ApJ, 668, 294

Cuppen, H. M. , & Hornekaer, L. 2008, J. Chem. Phys., 128, 174707

Cuppen, H. M., van Dishoeck, E. F., & Herbst, E., & Tielens, A. G. G. M. 2009, A&A, 508, 275

Cuppen, H. M., Kristensen, L. E., & Gavardi, E. 2010, MNRAS, 406, L11

Du, F., & Parise, B. 2011, A&A

Duley, W.W., & Williams, D.A., 1984, Interstellar Chemistry (Academic Press, London).

Duley, W.W., & Williams, D.A., 1986, MNRAS, 223, 177.

Farebrother, A.J., Meijer, A.J.H.M., Clary, D.C., & Fisher, A.J., 2000, Chem. Phys. Lett., 319, 303.

Gavardi, E., Cuppen, H. M., & Hornekaer, L. 2009, Chem. Phys. Lett., 477, 285

Green, N. J. B., Toniazzo, T., Pilling, M. J., Ruffle, D. P., Bell, N., & Hartquist, T. W. 2001, A&A, 375, 1111

Gould, R.J. & Salpeter, E.E. 1963, Astrophys. J., 138, 393

Hasegawa, T. I., Herbst, E., Leung, C. M., 1992, ApJS., 82, 167H

Herbst, E., & Cuppen, H. M. 2006, PNAS,103, 1‘2257

Hollenbach, D., & Salpeter, E.E., 1970, J. Chem. Phys., 53, 79.

Hollenbach, D., & Salpeter, E.E., 1971, ApJ, 163, 155.

Hollenbach, D., Werner M.W., & Salpeter, E.E., 1971, ApJ, 163, 165.

Hornekær, L., Baurichter, A., Petrunin, V.V., Field, D., & Luntz, A.C., 2003, Science, 302, 1943.

Katz N., Furman I., Biham O., Pirronello V., & Vidali G., 1999, ApJ, 522, 305

Le Petit, F., Barzel, B., Biham, O., Roueff, E., & Le Bourlot, J. 2009, A&A, 505, 1153

Manicò, G., Ragunì, G., Pirronello, V., Roser, J.E., & Vidali, G., 2001, Astrophys. J., 548, L253.

Pirronello, V., & Averna D., 1988, A&A, 201, 196.

Pirronello, V., Liu, C., Shen L., & Vidali, G. 1997a, ApJ, 475, L69.

Pirronello, V., Biham, O., Liu, C., Shen L., & Vidali, G. 1997b, ApJ, 483, L131.

Pirronello, V., Liu, C., Roser J.E, & Vidali, G. 1999, A&A, 344, 681.

Roser, J.E., Manicò, G., Pirronello, V., & Vidali, G., 2002, Ap. J., 581, 276.

Roser, J.E., Swords, S., & Vidali, G., 2003, Ap. J., 596, L55.

Sandford S.A., & Allamandolla L.J., 1993, ApJ, 409, L65.

Schutte, A., Bassi, D., Tommasini, F., Turelli, F., Scoles, G., & Herman, L.J.F., 1976, J. Chem. Phys., 64, 4135.

Shalabiea, O.M, Caselli, P., & Herbst, E., 1998, ApJ, 502, 652.

Smoluchowski, R., 1981, Astrophys. Space Sci., 75, 353.

Smoluchowski, R., 1983, J. Phys. Chem., 87, 4229.

Stantcheva T., Caselli P., & Herbst E., 2001, A&A, 375, 673.

Stantcheva, T., & Herbst, E. 2004, A&A, 423, 241

Takahashi, J, Masuda, K., and Nagaoka, M., 1999, MNRAS, 306, 22.

Vasyunin, A. I., Semenov, D. A., Wiebe, D. S., & Henning, Th. 2009, ApJ, 691, 1459

Williams, D.A., 1968, ApJ, 151, 935.

Williams, D.A., 1998, Faraday Discussions, 109, 1.

3 Kinetic Monte Carlo Studies of H_2 Formation on Grain Surfaces Over a Wide Temperature Range

3.1 Introduction

Molecular hydrogen (H_2) is a very important molecule in the interstellar medium. Almost all of the elemental hydrogen in translucent and dense molecular clouds are in its molecular form, which is also the most abundant molecular species in diffuse clouds. Moreover, H_2 is observed in large quantities in various galactic and extra galactic sources such as photon dominated regions (PDRs), jets, shocks, outflows of planetary nebula, active galactic nuclei (AGNs), and supernova remnants. The physical parameters like temperature, density can vary widely from one region to other. H_2 plays a crucial role in the dynamical and chemical evolution of these regions. It controls the mass budget in the star formation sites, it serves as an important coolant in the regions where other coolants are of little importance. Despite of its huge abundance and importance, the process of

The contents of this chapter has been published in "Iqbal, W., Acharyya, K., & Herbst, E. 2012, ApJ, 751, 581"

its formation in the diverse environments in the ISM is not entirely clear. Therefore the study of H_2 formation in the interstellar medium is of fundamental importance. Many attempts are made to explain its huge observed abundance. First attempts are through the gas phase chemistry, but the direct radiative association of two hydrogen atoms to form molecular hydrogen ($H + H \longrightarrow H_2 + \nu$) is a highly improbable process at the low temperature. There are some environments where gas phase reactions are important, especially regions of low grain abundance, e.g. early universe.

The most efficient gas phase processes are the following: 1) In the regions of high H densities ($\geq 10^8$ cm^{-3}) H_2 can form through three body reactions as shown below,

$$\begin{aligned} H + H + H &\longrightarrow H_2 + H, \\ H + H + H_2 &\longrightarrow H_2 + H_2, \end{aligned} \tag{3.1}$$

but in the ISM, densities are much lower and, therefore, these routes makes no significant contribution, and 2) in the regions of high free electron abundances H_2 can be produced through coupled reactions

$$\begin{aligned} H + e^- &\longrightarrow H^- + h\nu, \\ H^- + H &\longrightarrow H_2 + e^-. \end{aligned} \tag{3.2}$$

This route is efficient only in the regions of exposed radiation field. Except in unusual environments such as pertained in the early universe (Kreckel et al., 2010), the gas-phase formation of H_2 is inefficient, and cannot account for the observed abundance of H_2 (Gould & Salpeter, 1963). It is now well established that H_2 forms on the surfaces of the interstellar dust grains. The dust provides a surface for hydrogen atoms to meet and react and also removes enough of the reaction exothermicity so as to stabilize H_2

formation.

The experiments performed by Pirronello et al. (1997a,b, 1999) and analyzed by Katz et al. (1999), produced the first experimental data for use in astrochemical models. As mentioned, in the second chapter that it can not explain H_2 formation beyond 10 K for silicate grains and 15 K for carbonaceous grain. However, H_2 formation beyond this temperature is frequently observed. In unshielded diffuse regions, in which the temperature of mid-sized grains is around 20 K (Li & Draine, 2001), H_2 is believed to form efficiently. In addition, dust grains smaller than 0.01 μm show temperature fluctuations due to interaction with UV radiation, which frequently heat the grains up to 40 K (Cuppen, Morata & Herbst, 2006). In photo-dissociation regions (PDRs), the grain surface temperature can be above 75 K (Tielens & Hollenbach, 1985a,b), while in low-metal dwarf galaxies, dust temperatures can reach 120 K (Hirashita, Hunt & Ferrara, 2002). There are gas-grain models that posit the gas and grain temperatures to be equal so that even higher grain surface temperature can be considered. For example, Doty, Schoier & van Dishoeck (2004) considered the grain temperature of IRAS 16293-2422 to be around 250 K. Harada, Herbst & Wakelam (2010), considered H_2 formation up to 800 K for explaining molecular abundances around an active galactic nuclei. Thus it is pertinent to ask, how does H_2 form at higher temperatures?

Several attempts have been made to explain how H_2 formation can occur at surface temperatures beyond 15 K. Firstly, by introducing grains with rough or amorphous surfaces, in which all binding sites do not have the same binding energy (Chang, Cuppen & Herbst, 2005). Cuppen & Herbst (2005) were able to extend the temperature range of H_2 formation up to 40 K depending upon the roughness of the surface and whether the surface is a silicate or carbonaceous one or a mixed surface. Recent experiments by Perets et al. (2007) confirm the theoretical work, at least qualitatively. An earlier calculation of this type with similar conclusions had been performed by Hollenbach & Salpeter (1971).

Secondly, one can consider H_2 formation on surfaces that support strongly-bound binding sites, a process known as chemisorption. The first attempt to use chemisorption to produce H_2 under astronomical conditions was undertaken by Cazaux & Tielens (2002, 2004); Cazaux et al. (2005). These authors found that chemisorption extends the upper temperature limit for efficient H_2 formation considerably. More recent experiments of H_2 formation on graphite by Hornekær et al. (2006) have shown that strong binding sites are an integral part of a rather complex process at higher temperatures.

In this chapter, we develop an overall picture of the efficiency of H_2 formation on silicate and carbonaceous grains via the diffusive mechanism over a wide range of temperatures and other physical conditions with the use of the CTRW Monte Carlo method and shown that rate equation approach used for physisorption-chemisorption model of Cazaux & Tielens (2002, 2004, 2010) considerably overestimates H_2 formation efficiency. We provided rate coefficients for use in astrochemical models. Such an overall picture gives a sense of how H_2 is produced in widely differing interstellar environments. We are particularly interested in high temperatures since it is under these conditions that the detailed Monte Carlo results and the more widely used Rate equation results are likely to differ most strongly (Cazaux et al., 2005).

3.2 Processes on grain surfaces

3.2.1 Accretion

As described in the chapter 2, the first step is accretion; i.e., the landing of species onto a grain. In this case, H is the only species accreting onto the grain surface. With the assumption that sticking occurs on every collision with a grain, the accretion rate or flux ($f_{\rm H}$), of H atoms onto the surface of a dust grain, in units of monolayer per second

(ML s^{-1}) is given by the equation

$$f_{\rm H} = \frac{\upsilon_{\rm H}\ n_{\rm H}}{4\ n_s}, \tag{3.3}$$

where, $n_{\rm H}$ and $\upsilon_{\rm H}$ are, respectively, the number density and average velocity of H atoms in the gas phase, and n_s is the number density of sites on the surface of dust grain. This rate is related to the accretion rate in units of atoms s^{-1} by

$$R_{\rm H} = 4\ \sigma_{gr}\ n_s\ f_{\rm H}, \tag{3.4}$$

where σ_{gr} is the cross section of the spherical dust grain. The relation between the number of sites (N_s) on the grain surface and the grain cross section is:

$$N_s = 4\ \sigma_{gr}\ n_s. \tag{3.5}$$

Using equations (3.4) and (3.5), we obtain

$$R_{\rm H} = N_s\ f_{\rm H}, \tag{3.6}$$

which relates the accretion rate in ML s^{-1} and atoms s^{-1}.

3.2.2 Hopping, Tunneling and Desorption

Hydrogen atoms adsorbed on a grain site can move to another site via tunneling or hopping; the latter mechanism requires sufficient energy to overcome the energy barrier between the sites. We assume granular surfaces to be square lattices with four nearest neighbor sites, as on an fcc[100] plane, and that the probability of hopping or tunneling to each nearest site with the same barrier is the same. Different barriers occur between

Table 3.1: Potential Height and Width Parameters

Surface	a Å	A Å	E_P K	E_C K	E_S K	E_{SP} K	E_{SC} K	E_{H_2} K	μ	Model
Olivine	2.5	2	400	10000	100	100	5000	300	0	O1
Carbon	2.5	2	780	14000	100	100	7000	300	0	C1
Olivine	2.5	2	400	30000	100	100	15000	300	0	O2
Carbon	2.5	2	780	30000	100	100	15000	300	0	C2
Olivine	3	2	660	30000	100	100	15000	300	0	O3
Carbon	3	2	860	30000	330	100	15000	300	0	C3

different pairs of sites, which can be sites in which H atoms are weakly bound due to physisorption or strongly bound due to chemisorption. We imagine a surface on which physisorption and chemisorption sites occur at different heights and are offset horizontally from one another as well so as to form two offset planar lattices. Diffusion among chemisorption or physisorption sites occurs horizontally, while diffusion between the different types of sites has a vertical component as well. Thus, four different mobility rates are required: (1) from a physisorption site to a physisorption site (p-p), (2) physisorption site to a chemisorption site (p-c) (3) chemisorption site to a chemisorption site (c-c) and finally, (4) from a chemisorption site to a physisorption sites. These rates will be discussed in the later sections. In the standard model, physisorption sites must be entered first, corresponding to the well-known process of precursor mediated adsorption in surface science (Kolasinski, 2008). However, we also considered, adsorption directly to a chemisorption site. Based on the work of Cazaux & Tielens (2004), we utilized models O1, O2, and O3 for a flat olivine surface and C1, C2, and C3 for a flat carbon surface. The potential parameters for each model are shown in Table 3.1. We put these potential parameters in expressions given in Equation 2.2 to calculate different energy values. Obtained energy values are used to calculate transmission coefficients for tunneling, given by Equation 2.23, and thermal hopping, given by Equation 2.24.

In addition to parameters representing assorted heights for the potentials, there are parameters for potential widths (a for p-c and c-p and A for c-c and p-p) as well. The three models differ in the following parameters: Model 1 is based on "typical physical characteristics of silicate and carbonaceous surfaces," (Cazaux & Tielens (2004)) whereas, the other models are based on fits by Cazaux & Tielens (2004) to both low and high-temperature temperature-programmed desorption (TPD) results (Pirronello et al., 1997a,b, 1999; Zecho et al., 2002). In Model 2, the chemisorption binding energy is raised considerably to 30,000 K from the Model 1 values of 10,000 K (olivine) and 14,000 K (carbon). The barrier against tunneling/hopping from one such site to another, defined as 1/2 of the chemisorption energy, is also raised. In Model 3, along with the physisorption energy, the barrier width is also increased to 3 Å(Cazaux & Tielens, 2004). Essentially, in going from Model 2 to Model 3, an increase in width is counterbalanced by a decrease in the barrier height.

We integrated the transmission coefficient equations (Equation 2.23 and Equation 2.24) numerically over the energies available to H adatoms to obtain thermalized probabilities $P_{ij}(T)$ (Equation 2.25) to go from one site to another site via both tunneling and/or hopping. We then calculated the mobility (s^{-1}), or frequency of motion, of the thermalized adatom from site i to site j via

$$\alpha_{ij} = \nu_i \; P_{ij}, \tag{3.7}$$

where, ν_i, is the attempt rate or trial frequency and can be calculated by the Equation 2.26. In Figure 3.1, we show the mobility for H adatoms on the surface of olivine dust grains (Model O1) due to thermal hopping (lines without symbols) and tunneling (lines with triangles) separately. Mobilities from a physisorption to a physisorption site, a physisorption to a chemisorption site, a chemisorption site to a physisorption site, and

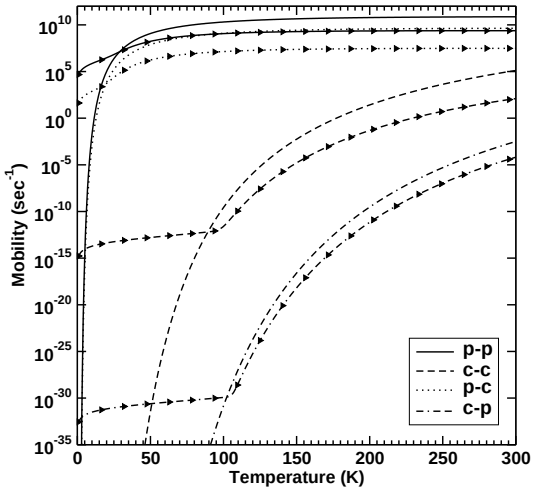

Figure 3.1: Mobility curves for H adatoms on olivine (Model O1). The lines without symbols are for mobility due to thermal hopping only whereas lines with triangles are for tunneling only.

a chemisorption to a chemisorption site is shown. It is evident from the plot that at low temperatures, the mobility due to tunneling H is greater than the mobility due to hopping. However, as the temperature is increased, the scenario changes; the p-p hopping rate is greater than the tunneling rate above 30 K, while for the p-c, c-p and c-c transitions, this cross-over temperature is 20 K, 80 K and 100 K respectively.

Figure 3.2, shows the total mobility of H adatoms due to thermal hopping and tunneling for Models 1, 2 and 3, and illustrates the strong negative effect of increasing the chemisorption binding energy E_C. The mobility of H atoms on the olivine grain models is higher than that on the carbon grain models for this reason. Differences exist among the various olivine and carbon models due to the increase in the chemisorption binding energy between O1(C1) and O2,O3 (C2,C3), while differences between the O2(C2) and O3(C3) models are due to more subtle potential effects. However, hydrogen mobility in p-p remains unchanged and p-c is slightly lower. Thus mobility of H atoms in c sites is decreased due to higher E_C, same is true for C2 model when compared with respect to C1 model. O2 and O3 models have same E_C, i.e., 30000 K but, E_P is changed from 400

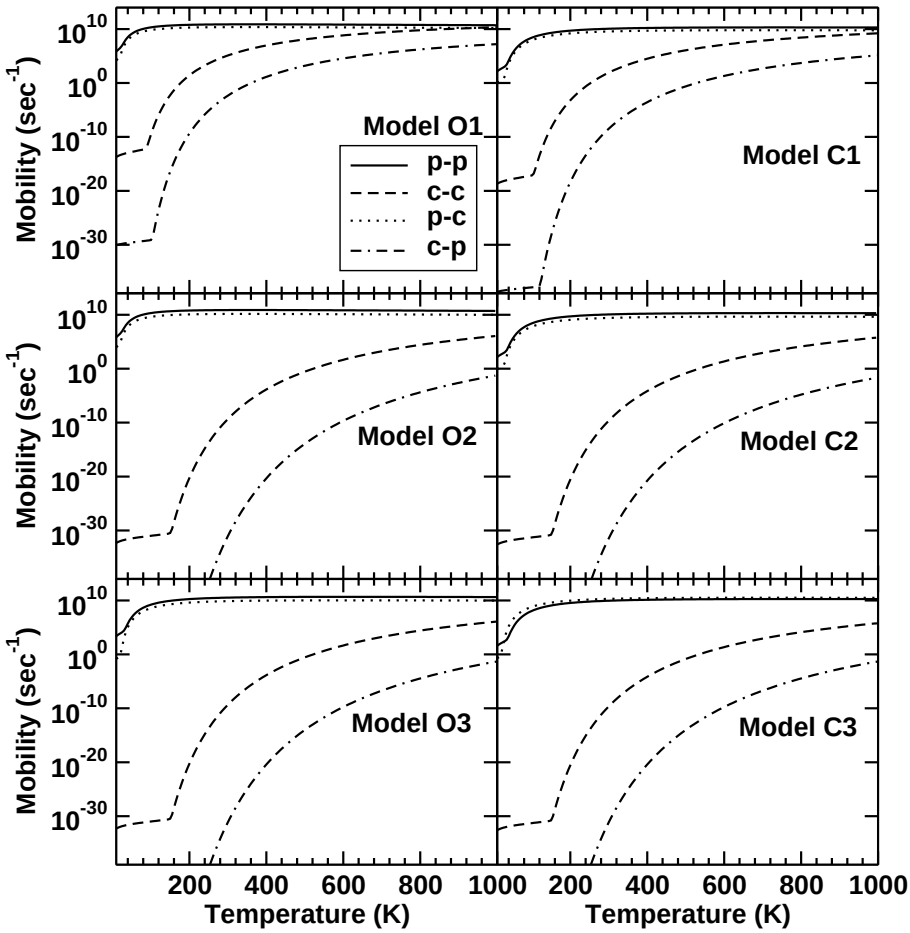

Figure 3.2: The total mobility due to hopping and tunneling for O1, C1, O2, C2, O3 and C3 models.

K to 660 K in O3 model which causes a minor change in mobility of p sites which goes almost unnoticed in the plot. In C3 model, E_P is changed from 780 K to 860 K and E_s is changed from 100 K to 330 K. This small change makes p-c mobility higher than p-p mobility which is not seen in any other model.

In competition with mobility, the adsorbed atom can desorb from site i at a rate according to the standard formula

$$W_i = \nu_i \ \exp\left(\frac{-E_i}{k\ T}\right) \tag{3.8}$$

where, E_i is the desorption energy for site i corrected for zero-point energy. Because the desorption energy from a physisorption site is much lower than the desorption energy from a chemisorption site, when an atom hops/tunnels to the latter, it will remain there unless the temperature is rather high.

3.2.3 H_2 recombination and formation efficiency

When an H atom hops or tunnels to a pre-occupied site in either the physisorption or chemisorption lattice, H_2 is formed. In addition, if an H-atom hops or tunnels from a physisorption site to a already occupied chemisorption site (or the reverse), H_2 formation can also occur. There are two mechanisms for desorption of the H_2 product as discussed in the Chapter 2: immediate release due to energy obtained from the exothermicity of reaction, and thermal desorption. In their original analysis of H_2 formation, based solely on physisorption, Katz et al. (1999) determined μ to be 0.33 and 0.413, respectively, for olivine and for amorphous carbon. However for chemisorption-physisorption analysis, Cazaux & Tielens (2004), used $\mu = 0.$. Here, we choose $\mu = 0$.

We run the code, which is discussed in more detail in the next section, until a quasi-steady state is reached in which the surface population of H atoms fluctuates around a constant value as shown in Figure 3.3.

The time to reach the quasi-steady state, mainly depends on the grain temperature and the incoming flux of hydrogen atoms among other parameters. It takes between 10^3 and 10^{10} seconds to reach a quasi steady state. The code is then run for a further time, which is at least twice the time that is required to achieve a quasi-steady state, so as to reduce the statistical noise. After the quasi-steady state has been reached initially, we keep a continuous count of the number of arriving H atoms and the number of H_2 molecules formed to determine H_2 formation efficiency (η) as described by Equation

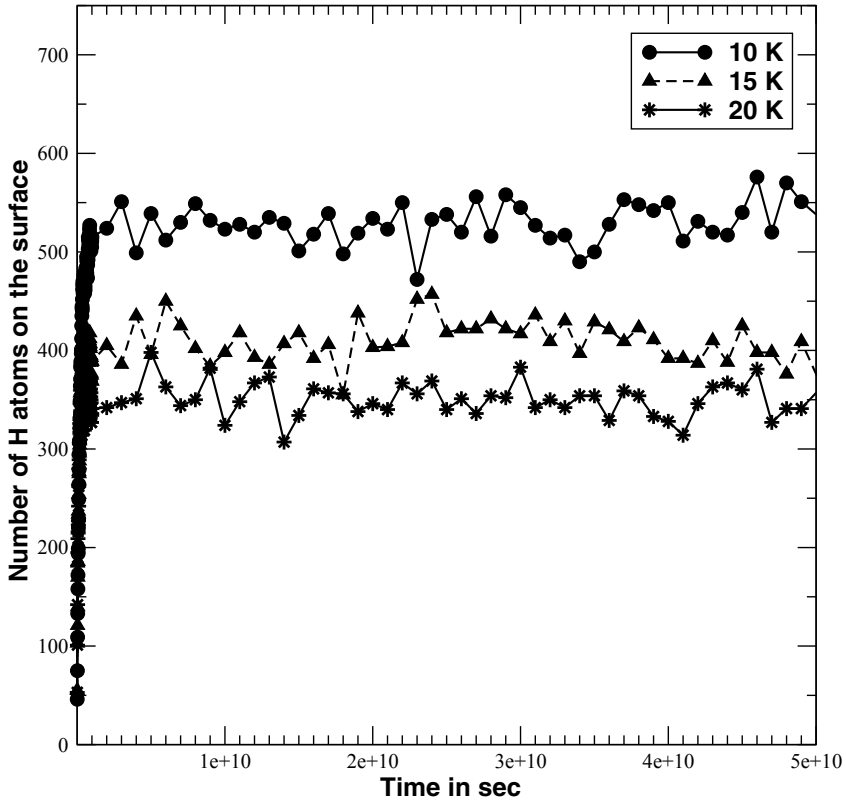

Figure 3.3: Showing steady state when coverage of H atom on the surface fluctuates around a constant number. The plots are for a dust grain with 100 × 100 number of sites and gaseous H density ($n_{\rm H}$) of 10, considering tunneling and chemisorption.

2.35. We have calculated the efficiency under a variety of different conditions, including temperature and flux, the size and chemical nature of the grain (olivine or amorphous carbon), and the degree of roughness of the surface.

3.3 Procedure

We used the CTRW Monte Carlo method for our study. In this technique, atoms and molecules are treated individually and their surface motions (accretion, hopping/tunneling, desorption, recombination) take place on a lattice depending upon the values of random numbers called in a continuous time frame (Chang, Cuppen & Herbst, 2005). In order

to mimic the spherical grain structure, we assumed periodic boundary conditions; i.e., a species that leaves the lattice on one side enters back from the opposite side. During the simulation, H atoms are deposited onto physisorption sites on the grain lattice randomly following LH mechanism. The lattice positions are simulated by a square array $G(k, l)$. The random site for a possible accretion is generated by random number (X, $0 < X < 1$), which is multiplied by the total number of sites (N_s) on the lattice. The result (y) is divided by the number of columns in the square lattice and then the integer 1 is added to the integral value of the result, which gives the k of the array. To determine the other index l, we take the result of the MOD function of y with the number of rows in the lattice and then add 1 to the integer value of it, which gives us l. Whether the H atom sticks or is rejected, a waiting time (WT_{acc}) is subsequently generated for the next accretion attempt of an H atom, assuming the accretion of H atoms to be a Poisson (memory-less) process. The waiting time for accretion is given by the following standard expression:

$$WT_{acc} = -\frac{\ln(X)}{R_{\rm H}} \tag{3.9}$$

where, X is another random number, $0 < X < 1$, and $R_{\rm H}$ is as defined in equation (3.6). The clock is then moved up from the current time t to determine the time of the next attempted accretion via

$$t_{acc} = t + WT_{acc}. \tag{3.10}$$

When an H atom in position k, l, designated $\rm H_{kl}$, moves to another site, designated k', l', another waiting time is calculated for its next move via

$$WT(\rm H_{k'l'}) = -\frac{\ln(X)}{\alpha_i + W_i}, \tag{3.11}$$

where α_i is the total mobility of the H atom from the site where it is adsorbed, and W_i is the desorption rate at that site, defined in equation (3.8). Here we assume that the mobility and desorption are also independent Poisson processes with same type of waiting time distributions, so that we can add the rates of the processes to get the total rate $(\alpha_i + W_i)$, which is then used to get the waiting time. When the time for the next move for any H atom comes, a random number (X) is generated to see if the H atom will travel to another site or desorb. If $X < W_i/(\alpha_i + W_i)$ then the H atom will desorb, otherwise it will travel to another site. If it travels (via hopping or tunneling) then another random number must be generated to determine whether the destination is a similar site or a different site. For example, if the H atom lies on a physisorption site and the generated random number $X < \alpha_{pp}/\alpha_p$, where α_{pp} is the mobility of H atoms from physisorption to physisorption site and $\alpha_p = \alpha_{pp} + \alpha_{pc}$ is the total mobility, then the H atom will travel to a physisorption site; otherwise, it will travel to a chemisorption site.

After each event we determine a new waiting time, recheck what event comes next, simulate the event at this new time, determine a new waiting time, etc., until the overall simulation ends. To investigate differences in results from the use of the kinetic Monte Carlo approach and the Rate equation approach of Cazaux & Tielens (2004), we simulated the formation of H_2 and calculated its formation efficiency using both the methods with the same parameters.

3.4 Results

In this section, we present the simulation results of H_2 formation on the ISM dust grain surface considering different ISM conditions. We used thermal hopping, tunneling or both of H adatom to simulate the H_2 formation on the surface of the dust grain. We

considered dust grains of different radii corresponding to different numbers of sites on the surface ranging from $N_s = 10 \times 10$ to 1000×1000, with a surface site density (n_s) of 2×10^{14} cm^{-2} for olivine and 5×10^{13} cm^{-2} for amorphous carbon (Biham et al., 2001). Thus for olivine, the grain radius varies between 20 Å and 2000 Å (0.2μm), and for amorphous carbon it varies between 40 Å and 4000 Å (0.4μm). We vary the H-atom flux by changing the number density ($n_{\rm H}$) of H atoms in the gas phase between 0.1 cm^{-3} and 100 cm^{-3}. Our simulation includes the dust grain with either physisorption sites or both physisorption and chemisorption sites. We also explored the role of surface roughness. For each simulation, we vary the grain temperature in the range $5 - 825$ K if possible. We discuss our results for physisorption sites first and then we discuss and compare the results with those in which chemisorption sites also exist. Our results are presented in different subsections to show the effect of tunneling, grain radius, flux of H atom and rough surface on the recombination efficiency of H_2 formation.

3.4.1 Simulation results with physisorption sites

In the following subsections we discuss our results for H_2 formation when H-atoms are adsorbed to a weakly bound physisorption sites.

3.4.1.1 Hopping vs. Tunneling

In the Figure 3.4, we have shown the H_2 formation efficiency as a function of temperature for a flat grain surface with 100×100 sites (grain radius = 200 Å) and subjected to a constant flux of 1.8×10^{-9} MLs^{-1}. The line with circle shows the H_2 formation efficiency when only thermal hopping is considered while the line with triangle shows the same but for the case when both thermal hopping and tunneling are considered. In Figure 3.5 we show corresponding coverage (in percentage) of H adatoms on the grain surface and

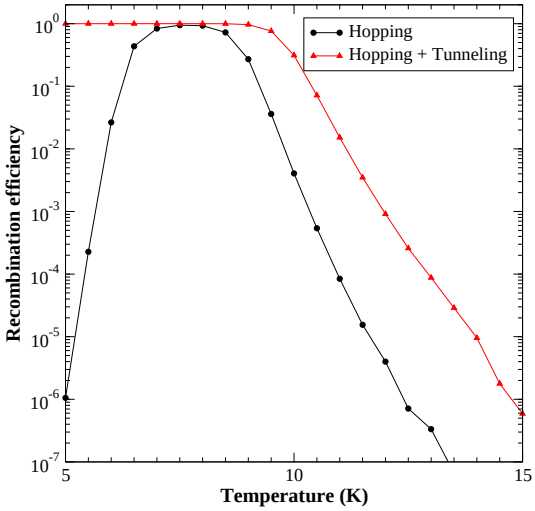

Figure 3.4: Recombination efficiency as a function of temperature for flat surface with 100×100 sites and a constant flux of 1.8×10^{-9} MLs^{-1}.

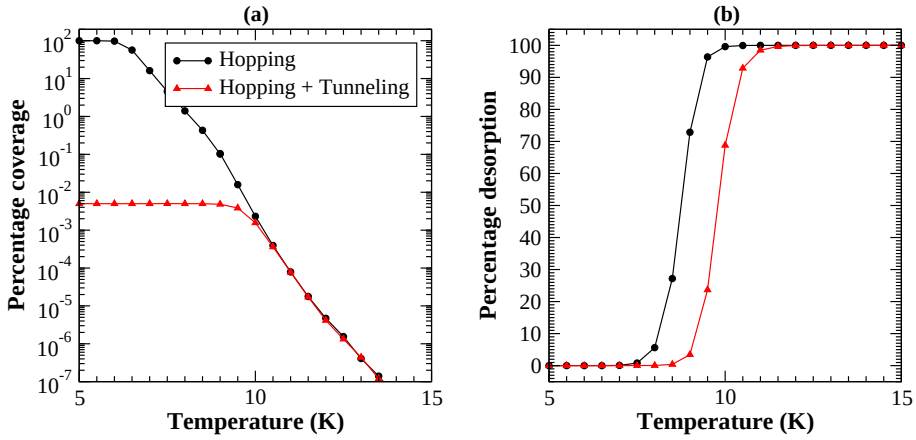

Figure 3.5: Percentage coverage and percentage desorption of H adatoms as a function of temperature for flat surface with 100×100 sites and a constant flux of 1.8×10^{-9} MLs^{-1} (legends apply to all plots).

percentage desorption of incoming H atoms. We see that in the case of thermal hopping the efficiency is high only when the surface temperature is between 6 K to 9 K while the efficiency is high for a temperature range of 5 K to 12 K when tunneling is also considered. In Figure 3.1 we see that the tunneling provides enough mobility even at 5 K to H adatom causing a high efficiency at low temperature. It is to be noted that we

have not simulated for temperatures lower than 5 K, since such a situation does not exist in ISM. At low temperature the desorption is almost negligible (see Figure 3.5(b)), since the H adatom are mobile due to tunneling, it is forming H_2. The coverage of H adatom is always below one percent (see Figure 3.5(a)) which is too low to cause noticeable rejection of incoming H atom due to the deposition of incoming H atom on the already occupied site. However, in absence of tunneling, grain is filled with immobile H-atoms at low temperature (T < 6 K) and incoming H atoms are rejected, which causes efficiency to go down as temperature is decreased. When temperature is increased above certain temperature, the efficiency decreases rapidly because of desorption of H adatom. In Figure 3.4 we see that the tunneling causes higher efficiency for temperature up to 12 K while the efficiency is low even at 10 K when tunneling is ignored. It is mainly due to the fact that tunneling rate is much higher in this temperature regime. Which increases probability of H_2 formation in this temperature regime.

3.4.1.2 Flux dependent

In Figure 3.6 we show the recombination efficiency as a function of temperature as obtained by simulation for different H flux corresponding to the number densities of, $n_{\mathrm{H}} = 0.1, 1, 10$ and 100 cm^{-3}, on the grain surface with 100×100 number of sites. We considered two different cases; one with only thermal hopping and other with both tunneling and thermal hopping. Corresponding coverage and desorption plots are shown in Figure 3.7.

We see that the efficiency curve shifts towards right as the flux of H atom increases when only hopping is considered. In presence of both hopping and tunneling, there is almost no shifting up to 8 K then it shifts towards right as temperature is increased farther. This could be explained by looking at the coverage of H adatom in the two cases. When only the thermal hopping is considered the coverage is always higher for

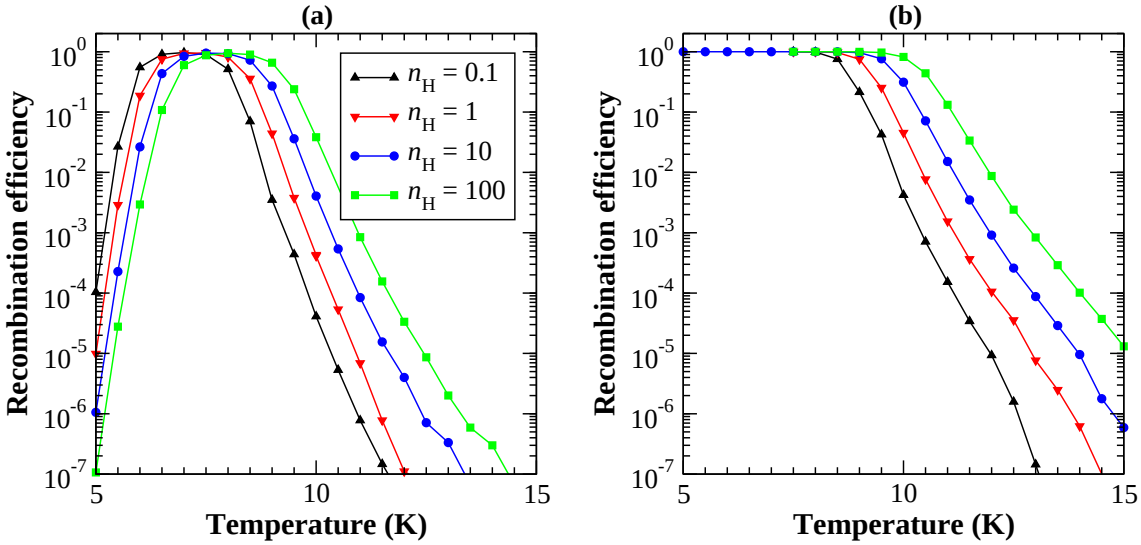

Figure 3.6: Recombination efficiency as a function of temperature as obtained by simulation for different H flux corresponding to different number densities, $n_{\rm H} = 0.1, 1, 10$ and 100 of H atoms on the grain surface with 100×100 number of sites, and considering two different cases: only thermal hopping (left-hand side plot) of adsorbed H atom and (right-hand side plot) both tunneling and thermal hopping (legends apply to both plots).

any temperature for a higher flux compared to a low flux. When temperatures is low ($\sim$ 5 K), mobility of H adatoms are highly reduced hence probability of recombination is also reduced. In addition, grain is quickly filled with immobile H adatoms which restrict farther adsorption of H atoms. Thus efficiency decreases as the flux increases at low temperature side of the efficiency curve. As temperature is increased, mobility of H adatoms also increases and consequently, coverage decreases due to recombination. Thus, at higher temperature side of the curve when the coverage is low due to high desorption rate, the efficiency is high as higher flux means there are more H adatoms in the grain which enhances H_2 formation efficiency. But when tunneling is introduced, the coverage is never high and hence the rejection of H atom does not cause any decrease in efficiency at the low temperature side of the efficiency curve. However, at high temperature side of the curve, higher flux causes higher efficiency as there are more H adatoms available on the grain for H_2 formation process.

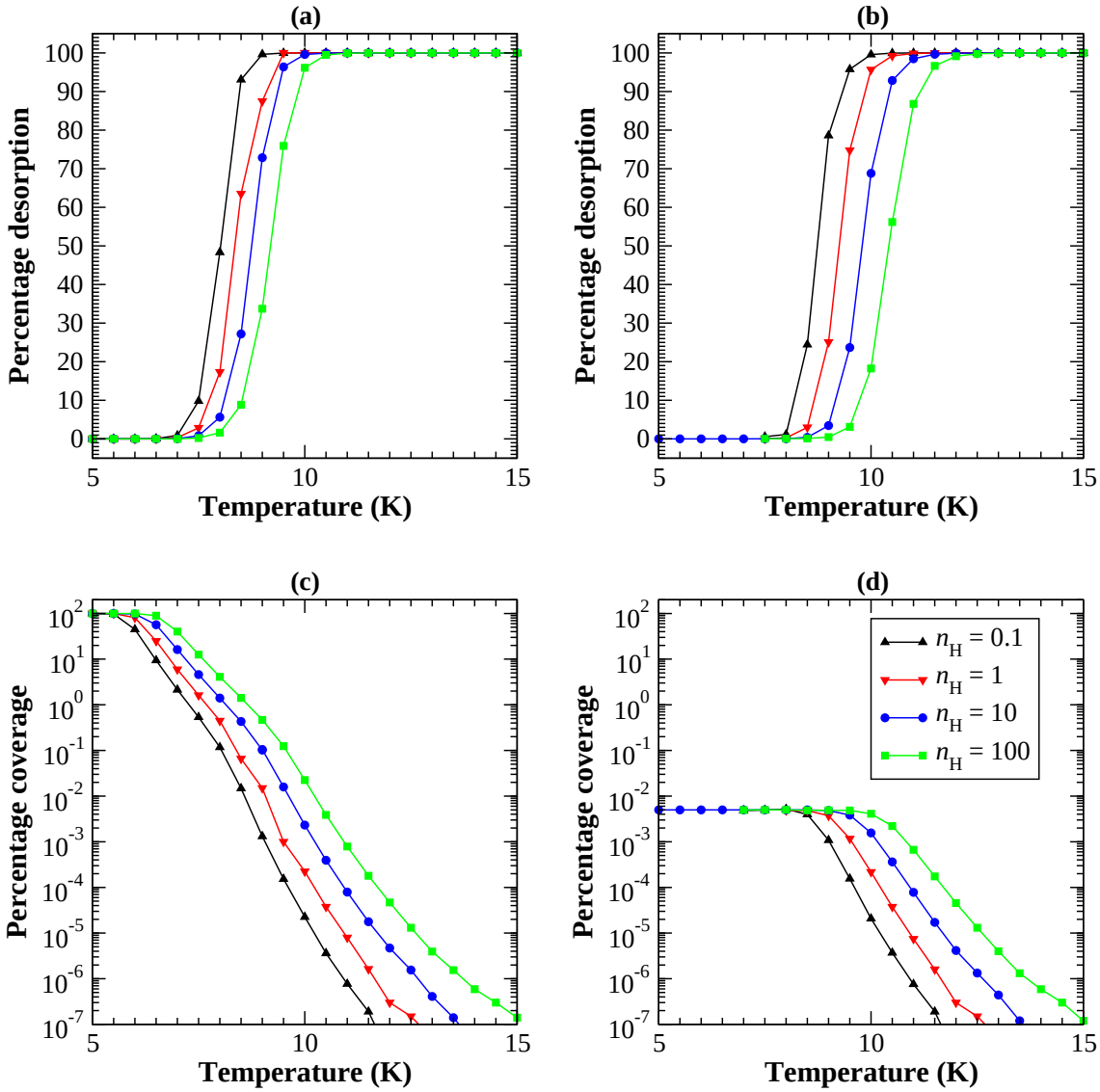

Figure 3.7: Percentage coverage (bottom) and percentage desorption (top) as a function of temperature for flat surface with 100 × 100 sites, and considering two different cases: only thermal hopping (a, c) of adsorbed H atom and (b, d) both tunneling and thermal hopping (legends apply to all plots).

3.4.1.3 Site dependence

Figure 3.8 shows the recombination efficiency as a function of temperature as obtained by simulation for different number of sites on the grain surface, $N_S = 10^2$, 10^3, 10^4, 10^5 and 10^6. Like previous calculation, we considered two cases one with hopping and other

with hopping and tunneling. Calculations are done for a constant flux of 1.8×10^{-9} MLs^{-1}. We see that there is almost no site dependence on H_2 formation efficiency when

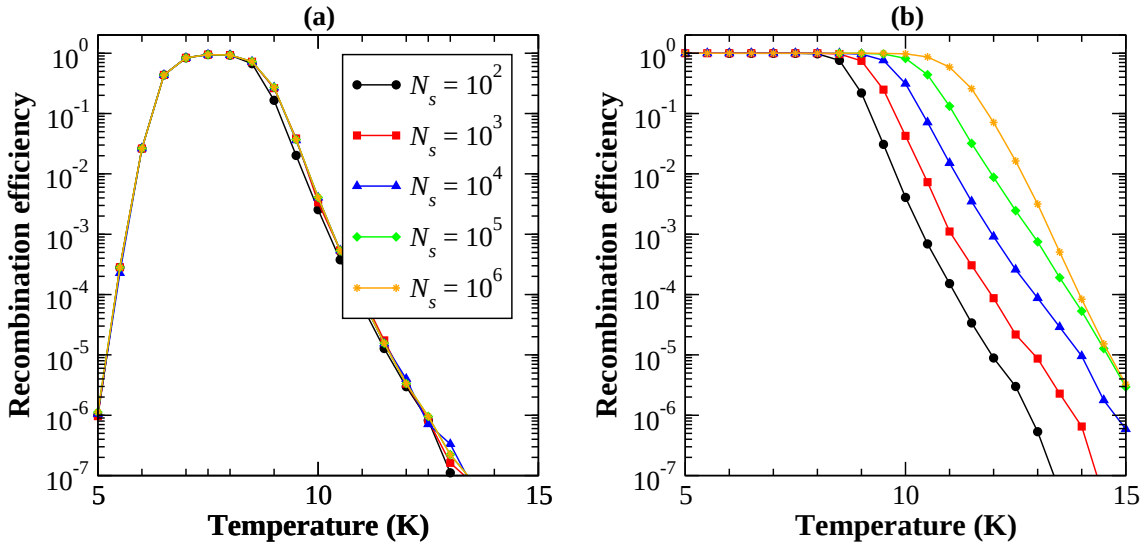

Figure 3.8: Recombination efficiency as a function of temperature as obtained by simulation for different number of sites on the grain surface, $N_S = 10^2$, 10^3, 10^4, 10^5 and 10^6, and considering two different cases: only thermal hopping (a) of adsorbed H atom and (b) considering both tunneling and thermal hopping, for a constant flux of 1.8×10^{-9} MLs^{-1} (legends apply to both plots).

only hopping is considered. However, in presence of both hopping and tunneling, below 8 K there is no site dependence. However, at temperature greater than 8 K, bigger is the grain higher is the efficiency at a given temperature. Figure 3.9 shows the coverage and desorption plots for site dependence of efficiency. It can be seen that percentage desorption does not change when there is only thermal hopping as result no change in efficiency is observed. However, we can see that when both hopping and tunneling is present, bigger is the grain lower is the percentage desorption at a given temperature. As a result efficiency is also high when grain is bigger in size.

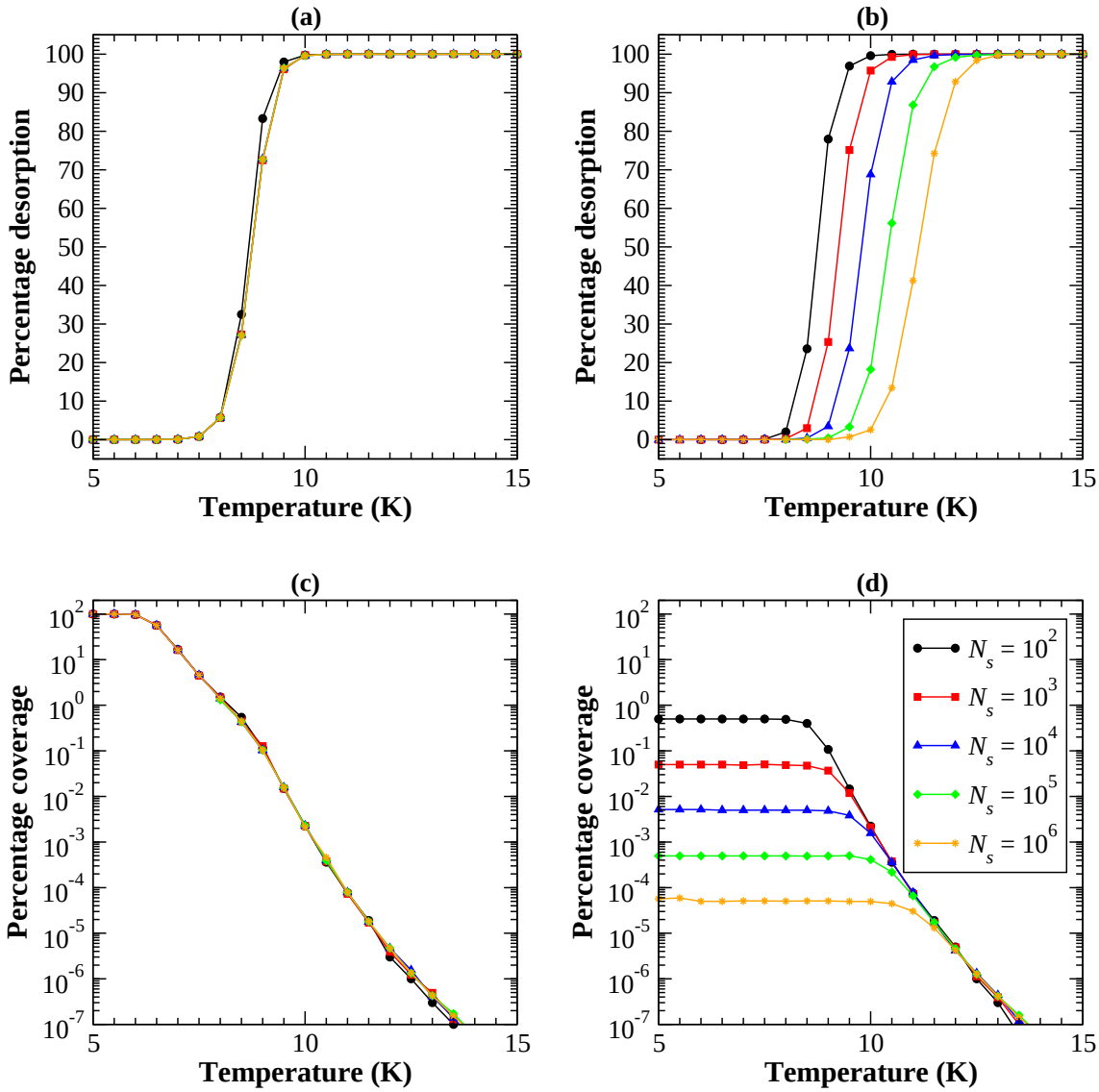

Figure 3.9: Percentage coverage (bottom) and percentage desorption (top) as a function of temperature for flat surface with different number of sites, $N_S = 10^2$, 10^3, 10^4, 10^5 and 10^6, and considering two different cases: only thermal hopping (a, c) of adsorbed H atom and (b, d) both tunneling and thermal hopping, for a constant flux of 1.8×10^{-9} MLs^{-1} (legends apply to all plots).

3.4.1.4 Effect of rough surface

Figure 3.10 shows the mobility profile of a H adatom on the physisorption site with different number of lateral bonds. We see that the mobility of H adatom on the site with no lateral bond is almost 10^4 times higher than that at a the site with four lateral

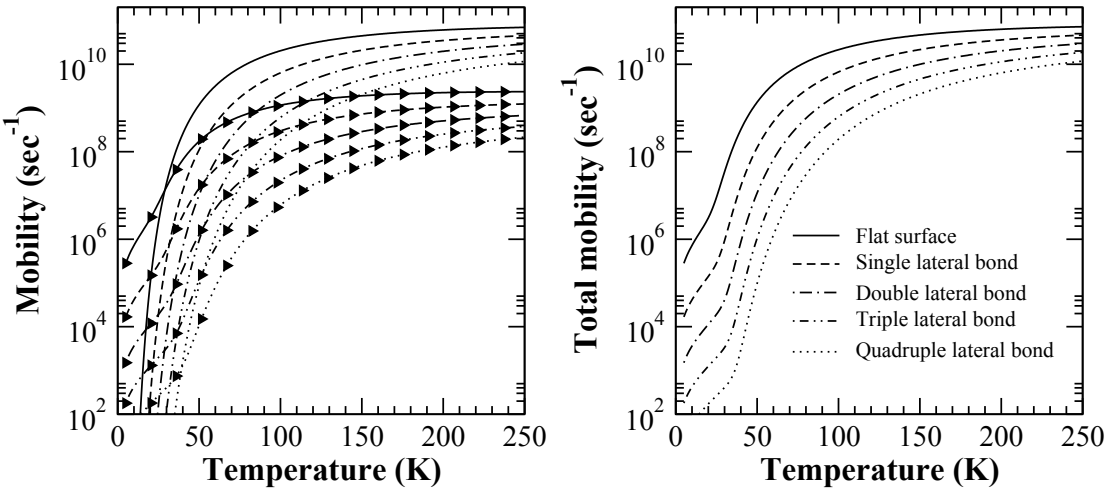

Figure 3.10: Mobility (in $\sec^{-1}$) of H adatom as a function of temperature, on physisorption site with different number of lateral bond. In the left plot, the lines without symbols show the mobility due thermal hopping and the lines with symbols are the mobility due to tunneling, the right plot shows the total mobility curve(legends apply to both plots).

bond at low temperature but as the temperature increases the difference decreases, this shows that the introduction of lateral bonds will effect the efficiency of H_2 formation at low temperature but at higher temperature the effect will not be too large.

In Figure 3.11 we illustrated the efficiency of H_2 formation on the rough surface with and without tunneling. The efficiency curve for the flat surface is also included for better comparison of the results. Corresponding coverage and desorption plots are shown in Figure 3.12. We see that in the absence of tunneling the efficiency at the rough surface is high up to a good range of temperature but when the tunneling is introduced the effect of rough surface is reduced noticeably (see the curves with triangle symbol). It is mainly due to following reason. In sites with lateral bonds H adatoms are more strongly bound due to higher binding energy. Thus H adatoms are bound to the surface up to higher temperature and when H adatoms hops to these strongly bound sites they recombine and form H_2. As a result, we find high efficiency at higher temperature, compared to the plain surface. But when the tunneling is also considered, the mobility of adatom is

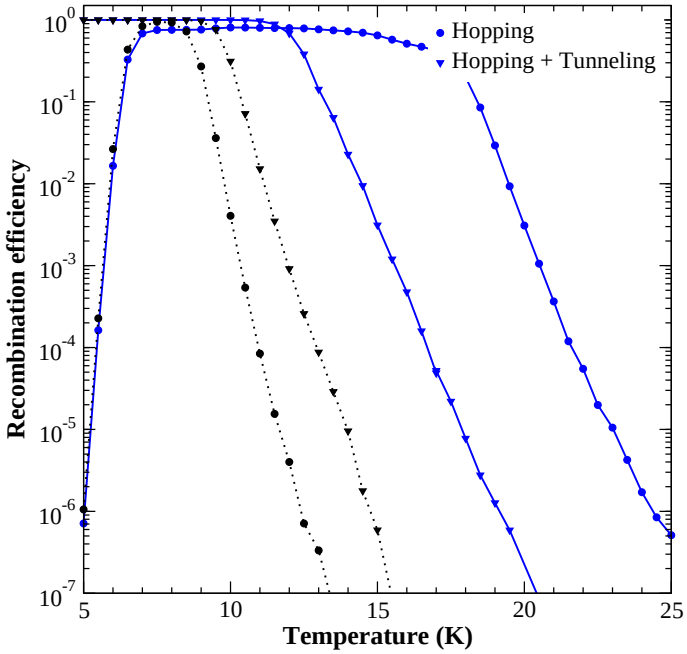

Figure 3.11: Recombination efficiency as a function of temperature, the dotted lines are for flat surface and the solid lines are for rough surface (all the plots are for a grain with 100×100 number of sites and a flux of 1.8×10^{-9} MLs^{-1}).

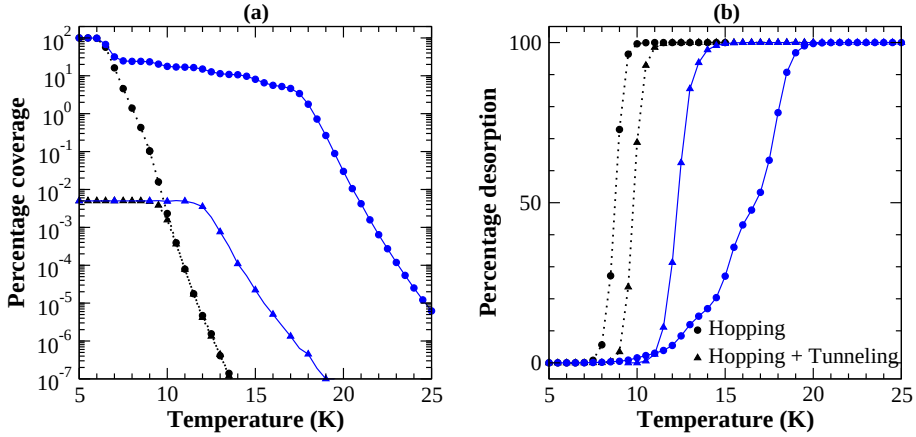

Figure 3.12: Percentage coverage and percentage desorption as a function of temperature, the dotted lines are for flat surface and the solid lines are for rough surface (all the plots are for a grain with 100×100 number of sites and a flux of 1.8×10^{-9} MLs^{-1}) (legends apply to all plots).

much higher and it does not stay bound in the rough surfaces and adatom adsorbed to a rough portion of the dust grain can tunnel to the flat part and quickly desorb back to gas phase. Thus efficiency is low compared to thermal hopping. Corresponding percentage coverage and percentage desorption as function of temperature is shown in Figure 3.12.

3.4.2 Simulation results with physisorption and chemisorption sites

Chemisorption of H atoms on the grain surface has a dominant effect on the H_2 formation on dust grain. In the presence of chemisorption together with physisorption the range of temperature in which the efficiency of H_2 formation is high, stretches beyond 200 K or more ($\sim$ 800 K) depending upon the depth of the chemisorption well, this gives a good explanation for the observed H_2 formation at temperature beyond 30 K.

Figure 3.13 shows the variation of molecular hydrogen formation efficiency as a function of temperature for all six models (O1, O2, O3, C1, C2, and C3), at a density for $n_{\rm H}$ of 10 cm^{-3}, which corresponds to a flux of $1.8 \times 10^{-10}\sqrt{T}$ ML s^{-1} for olivine and $7.2 \times 10^{-10}\sqrt{T}$ ML s^{-1} for carbon. The solid lines are results from the kinetic Monte Carlo simulation while the dashed lines are from the Rate equation method (Cazaux & Tielens, 2004).

The basic reason for the relatively high H_2 formation efficiency at higher temperatures for physisorption-chemisorption models, compared with pure physisorption models, is the higher binding energy for chemisorption, which enables chemisorption sites to retain H atoms on the grain up to much higher temperatures so that H_2 formation can still occur. Nevertheless, it can be seen that for all six models, the efficiency calculated by the Monte Carlo simulation lies below that calculated with the use of Rate equations at all but the lowest temperatures. This effect occurs because the Rate equation method does not take into account fluctuations, and utilizes average abundances. As a result,

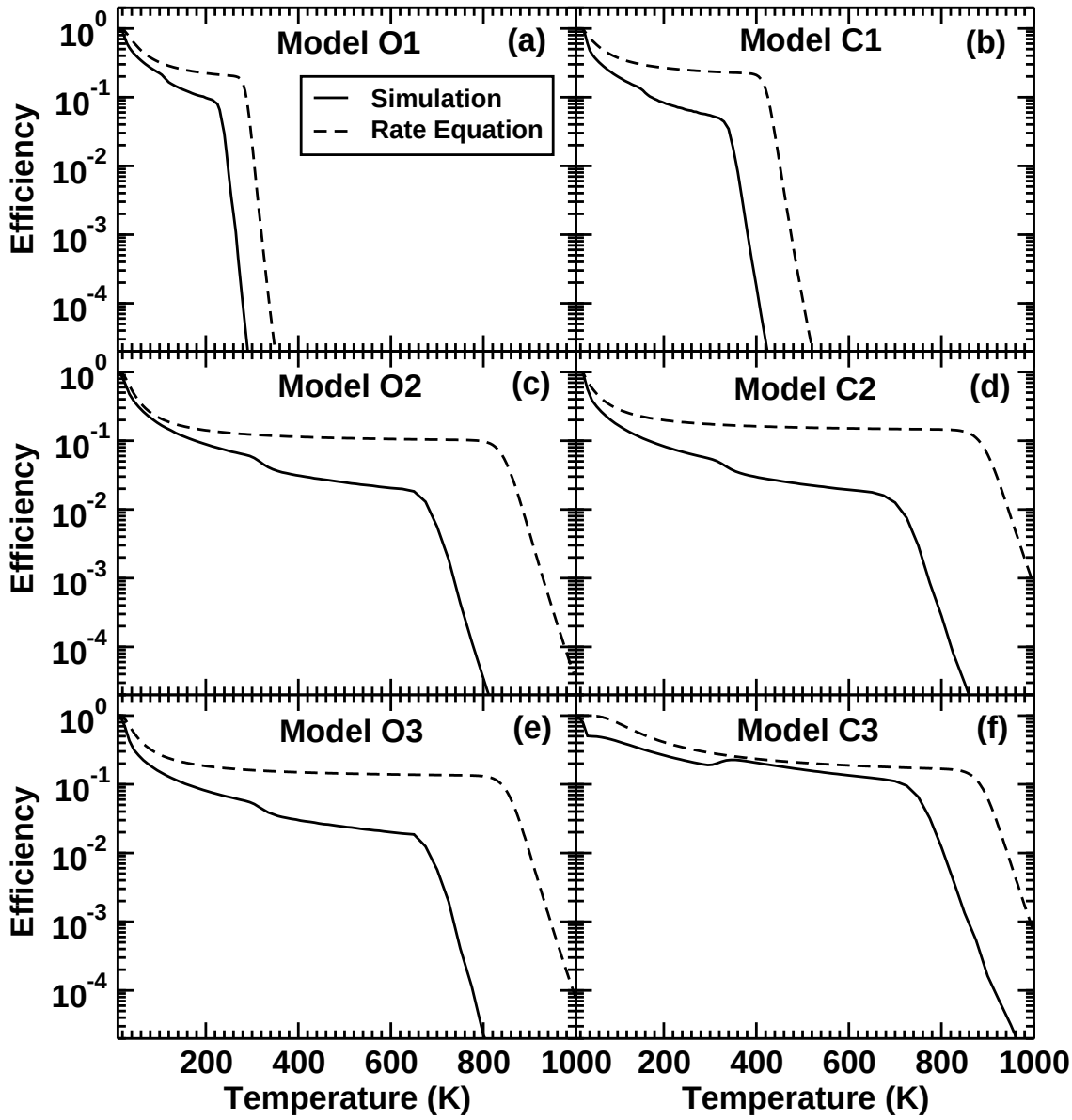

Figure 3.13: Recombination efficiency as a function of temperature for a flat surface with $N_s = 100 \times 100$ and a constant density $n_{\rm H}$ of 10 cm^{-3}, which corresponds to a flux of $1.8 \times 10^{-10}\sqrt{T}$ ML s^{-1} for olivine and $7.2 \times 10^{-10}\sqrt{T}$ ML s^{-1} for carbon. These parameters represent our standard models. Solid lines: kinetic Monte Carlo simulation; dashed lines: Rate equation method.

it overestimates the H_2 formation efficiency by a negligible to small (factor of a few) amount at low temperatures but by a much larger amount at high temperatures. At high temperatures, the average population of H atoms on a grain is more likely to be

less than unity, while the minimum number of H atoms needed on a grain to produce H_2 is obviously two. For example in Model O1, the discrepancy factor becomes larger than an order of magnitude at 250 K.

At lower temperatures, one must make a distinction between the overall coverage and the coverage of the physisorption layer, since diffusion of physisorbed atoms to filled physisorption or chemisorption sites becomes the dominant mechanism leading to reaction. The overall coverage exceeds one H atom per grain (10^{-2} %) while the coverage in the reactive physisorption layer can be less than 1 per grain. The small discrepancy at the lowest temperatures is due to a very small abundance of physisorbed H atoms (≤ 1 atom per grain) which provide all of the reactants at these temperatures.

A previous Monte Carlo approach to H_2 formation was reported briefly by Cazaux et al. (2005), who obtained little difference with the results from their Rate equation approach, as shown in their Figure 3, although the authors stated that at still higher temperatures, a difference was to be expected, for the same reasons given here.

In addition to this effect, one also sees that for both approaches the efficiency decreases with increasing temperature, mainly due to the increasing rate of H atom desorption. For Model O1, the efficiency calculated by our simulation drops to lower than 0.1 at 200 K, whereas with Rate equations, it remains at 0.2 between 100 K and 300 K and then goes down very sharply. The trends for Model C1 are similar but are shifted to higher temperatures; here the Monte Carlo method shows a dropping efficiency of 0.05 at 350 K while the Rate equation method shows a constant value of 0.3 between 100 K and 420 K before dropping sharply. In Models O2 and C2, with a much higher chemisorption well depth, the efficiency of H_2 formation at 800 K remains as high as 0.1 - 0.2 with the Rate equation approach, while our Monte Carlo simulations show that by 700 K, the efficiency is down to ≈ 0.01. We observe a similar trend for Model O3,

whereas Model C3 is somewhat different; here the Monte Carlo efficiency is closer to that calculated from Rate equations until 700 K before dropping sharply. This latter result, which is closest to that of Cazaux et al. (2005), arises from potential effects that produce a p-c rate larger than the p-p rate, which means that a physisorbed H atom has a greater probability to hop to a chemisorbed site than to a physisorbed site, although hopping still has to compete with desorption. This effect results in a greater H atom population in chemisorbed sites and a higher reaction efficiency.

3.4.2.1 Hopping vs. Tunneling

In Figure 3.1, we see that the mobility of H adatoms on chemisorption sites for Model O1 is many orders of magnitude lower than the mobility on physisorption sites for both tunneling and thermal hopping through 300 K. For physisorption sites, the mobility due to tunneling dominates up to $\approx$ 20 K, and above 20 K thermal hopping dominates, while for chemisorption sites, the tunneling dominates up to $\approx$ 100 K, while above 100 K thermal hopping dominates. A similar situation occurs for the other models. How do the relative mobilities for tunneling and hopping translate into H_2 recombination efficiency?

Figure 3.14 shows the recombination efficiency for Model O1 as a function of temperature. In the presence of tunneling, the efficiency is higher up to $\approx$ 40 K, while above this temperature tunneling plays little role. At very low temperatures ($<$ 7 K), the efficiency goes down rapidly if only hopping is included; when tunneling is included, it remains constant at near unity.

More detail about what is happening can be obtained by looking at the H atom surface coverage in physisorption and chemisorption sites as a function of temperature for Model O1. Figure 3.15 shows the percentage site coverage (100$\times$ the fractional

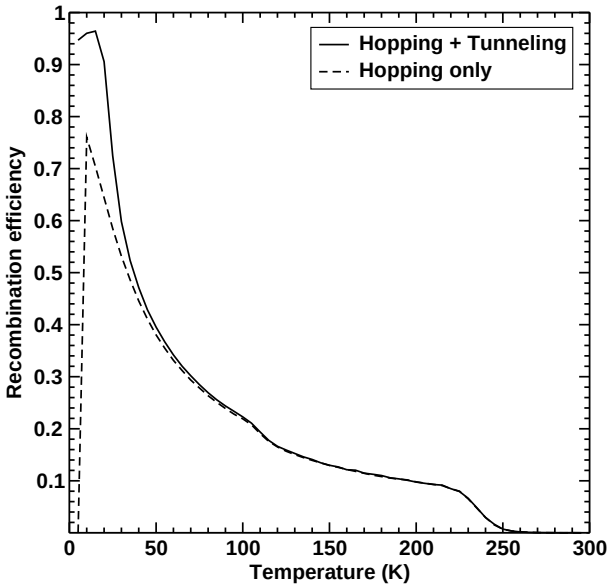

Figure 3.14: Recombination efficiency as a function of grain temperature for Model O1, with $N_s = 100 \times 100$, and flux $= 1.8 \times 10^{-10}\sqrt{T}$ ML s^{-1}. The solid line shows the efficiency when both hopping and tunneling are included while the dashed line shows the efficiency when only hopping is considered.

number of monolayers) for H as a function of temperature both in the presence and absence of tunneling. In the absence of tunneling (hopping only), the very high coverage at temperatures below 8 K is mainly due to immobile H atoms locked in physisorption sites because hopping is inefficient. At $\approx$ 8 K, mobility increases and reactions begin to occur even in the absence of tunneling. By 10 K, the H-coverage starts to decrease very slowly and is almost constant at $\approx$ 5% until 100 K. This effect occurs because once the physisorbed H-atoms have enough mobility, a fraction of H-atoms are moved to chemisorption sites and remain there due to low mobility and a negligible desorption rate. While the coverage is dominated by chemisorbed H atoms, H_2 formation occurs mainly via the hopping of physisorbed H atoms onto chemisorption sites filled with atomic hydrogen. When tunneling is included, the coverage is low at very low temperatures

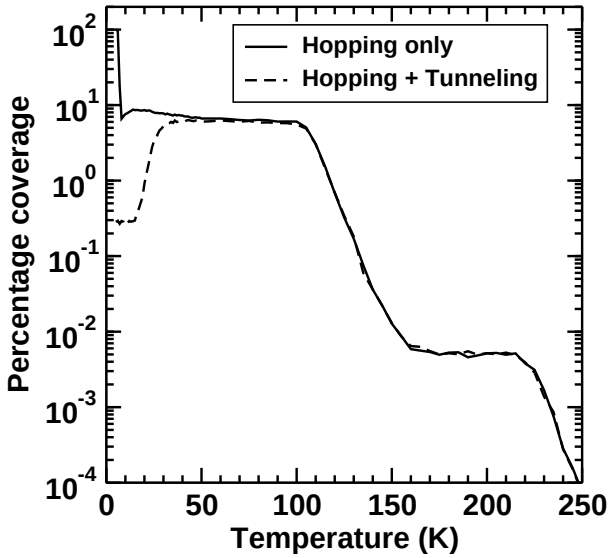

Figure 3.15: Percentage coverage as a function of temperature for O1 model shown in Figure 3.14.

because of the higher efficiency of reaction, but rises to 5% by 30 K, when the coverage is once again dominated by chemisorbed H atoms. Around 30 K, a stable ratio of physisorbed to chemisorbed adatoms is reached, and the coverage no longer differs from the case with tunneling. This coverage leads to an average of 500 H atoms on the physisorption and chemisorption binding sites of an average grain, mainly on the latter, which is still a high enough number that the Rate equation approximation should be reasonably accurate although leading to efficiencies that are somewhat large.

This discrepancy might be caused by the small number of physisorbed H atoms, since at these temperatures, H_2 formation mainly depends on the transfer of an H atom from a physisorbed site to a pre-occupied chemisorbed site. As temperatures rise above 100 K, chemisorbed adatoms become mobile (see Figure 3.1), which causes an increase in H_2 production so that the H-atom coverage starts to decrease strongly again. However, at this temperature, desorption can still not occur from a chemisorption site, so that an almost constant 1% coverage starts as the temperature reaches 150 K. Around 200

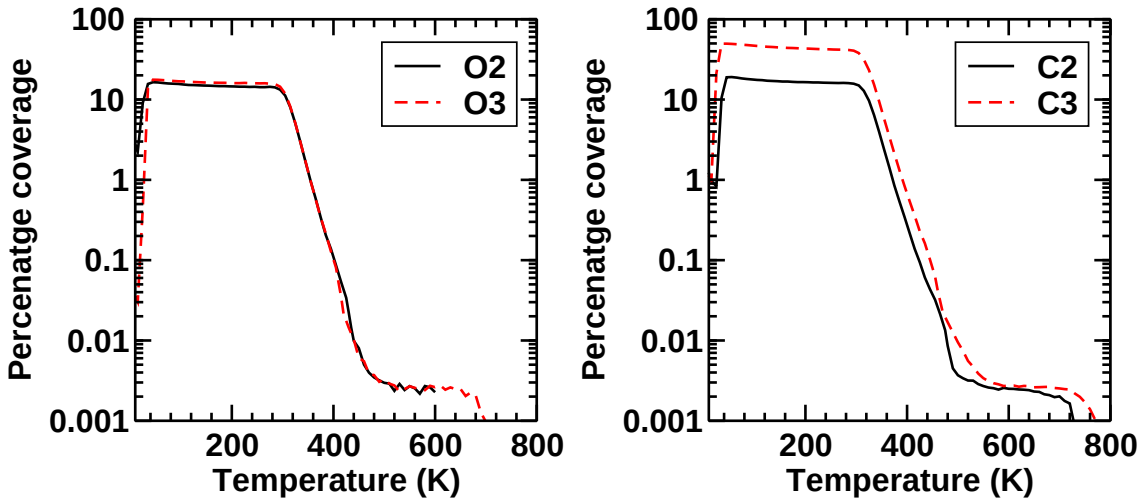

Figure 3.16: Percentage coverage as a function of temperature for Models O2, O3, C2 and C3 with "standard" parameters as in Figures 3.13.

K, the desorption of chemisorbed H atoms starts, hence the coverage begins to decrease yet again. Because there are no more binding sites with higher energy, the coverage goes down very rapidly. At these temperatures, the average number of H atoms on the binding sites becomes less than unity and the Rate equation approximation becomes a poor one. Above 250 K, however, it becomes almost impossible to perform kinetic Monte Carlo simulations because there hardly any H atoms on the grain, and hardly any reactions that occur.

For completeness, Figure 3.16 shows a coverage vs temperature plot for Models O2, O3, C2, and C3 in which both hopping and tunneling are included. It is clear that for Model C3, the coverage is always higher, so one expects the calculated efficiency to be much closer to the Rate equation result, which is indeed the case.

3.4.2.2 Flux and size dependence

Figure 3.17 shows the dependence of the recombination efficiency on flux (or H-atom density) for a dust grain with $N_s = 100 \times 100$, when Model O1 is used. Within the density

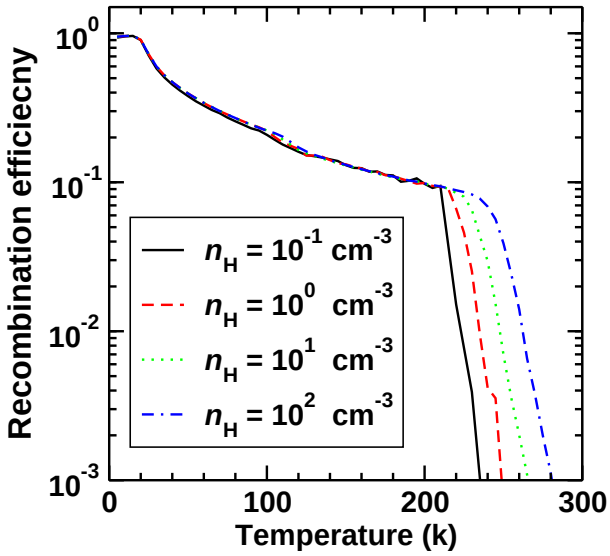

Figure 3.17: H_2 formation efficiency for different hydrogen atom densities using Model O1 considering both hopping and tunneling.

range $n_{\rm H} = 10^{-1} - 10^{2}$ cm^{-3}, there are only two regions where a significant dependence exists. Otherwise, the increase in flux translates into a proportional increase in H_2 production, so that the efficiency (if not the rate) stays the same. The first zone, with a weaker dependence, lies between 90 K and 120 K. The second zone lies above 200 K, when the desorption rate is very high. Under these conditions, a higher flux means a higher number of H atoms on the grain, hence the probability to form a H_2 molecule is also higher.

Figure 3.18 shows the percentage coverage plot, from which we see that in these zones, the greater the flux the greater the coverage.

In Figure 3.19 we show efficiency plots with the O1 model of H_2 formation for grains with different numbers of sites, N_s, which are related to the square of the radii. Here we see that the recombination efficiency is almost independent of the number of sites except for temperatures above 210 K. Here the coverage of adatoms becomes very low, so that there are not more than one or two adatoms per grain at a time. The smaller

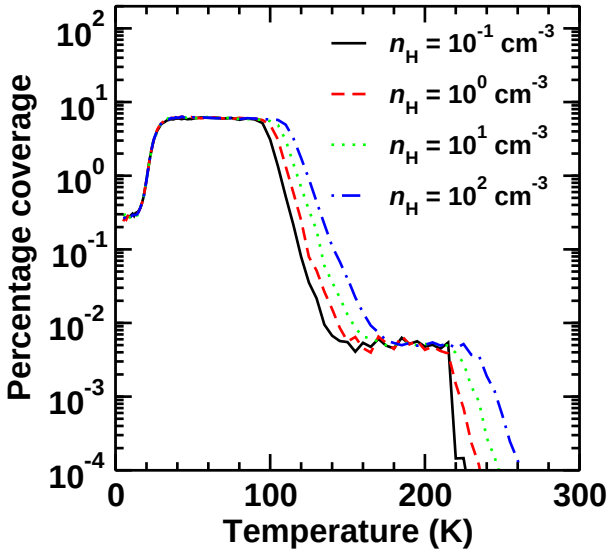

Figure 3.18: Percentage coverage for models shown in Figure 3.17.

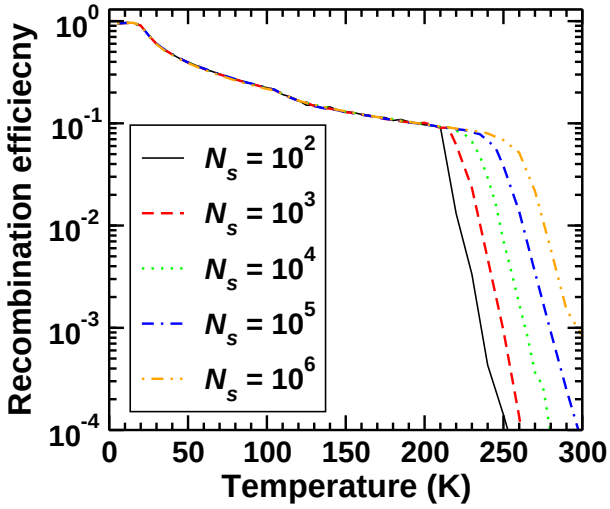

Figure 3.19: Recombination efficiency plots of H_2 formation using Model O1 for different numbers of sites on a grain, considering both hopping and tunneling.

the size of the grain, the greater the time separation between two incoming H atoms. The probability of having two hydrogen atoms simultaneously on the grain surface is lower for smaller grains, especially at such a high temperature, and the efficiency of H_2 recombination is less. Thus, the smaller the grain, the lesser the probability to form H_2.

3.4.2.3 Effect of rough surface

To examine the effect of a rough surface on the recombination efficiency, we have generated a simple rough surface that has five different physisorption binding energies depending on lateral bonds as prescribed by Chang, Cuppen & Herbst (2006). To this we add chemisorption sites, all with the same binding energy.

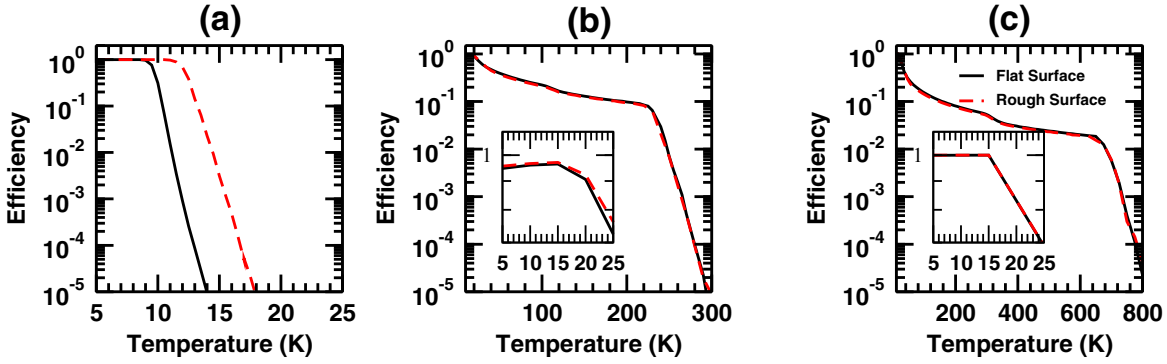

Figure 3.20: Recombination efficiency as a function of temperature for both flat and rough surfaces. Panel (a) contains results for physisorption sites only, Panel (b) contains results for Model O1, while Panel (c) contains results for Model O2. Other parameters are the same as used for Figure 3.14.

In Figure 3.20, we show the recombination efficiency as a function of temperature for a regular (flat) surface and our rough surface. Figure 3.20(a) represents the efficiency for olivine when only physisorption sites are considered. The panel shows that incorporation of a rough surface broadens the temperature window for higher efficiency. This result is discussed by Chang, Cuppen & Herbst (2006) in more detail, although the rough surface has certain similarities to the addition of chemisorption sites to physisorption sites in an otherwise flat surface, which can be thought of as a quasi-rough surface with two different types of sites. Given this analogy, one expects that if Models 1 and 2, with physisorption and chemisorption sites, are roughened for physisorption, little additional

effect will occur, because the chemisorption sites are so much deeper than the roughened physisorption sites. Indeed, panels (b) and (c) of Figure 3.20 show that there is little to no effect of a rough surface on Models O1 and O2 respectively. Moreover, it is clear that the addition of chemisorption sites has a much larger effect on the efficiency as a function of temperature than does the addition of roughness to physisorption.

3.4.2.4 Barrierless direct chemisorption

Although our calculations have been based on a joint physisorption-chemisorption model in which physisorption sites are the only entrance sites, there are some systems in which direct barrierless chemisorption can occur without a precursor. It should be noted, however, that experiments and calculations indicate that H atoms can chemisorb onto graphite and graphene only after surmounting a barrier of 0.2 eV (Jeloaica & Sidis, 1999; Ivanovskaya et al., 2010). Nevertheless, we consider a model for barrierless chemisorption in which only chemisorption sites are available, based on Models O1 and O2. The results

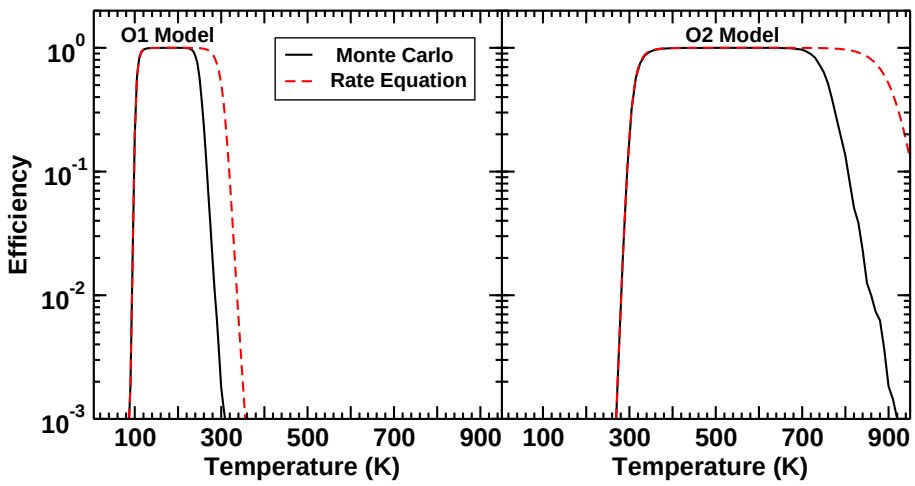

Figure 3.21: Recombination efficiency as a function of temperature for direct chemisorption models in which 100% of the initially encountered sites involve chemisorption (C sites).

are shown in Figure 3.21, where we can see that the efficiency with the O1 model lies near unity between 100 K and 250 K, dropping off sharply at lesser and greater temperatures. The efficiency for the O2 model follows a similar pattern except that it occurs at higher temperatures: the efficiency is near unity from 400 K through 750 K. These models with barrierless direct chemisorption yield high efficiencies only at intermediate temperatures because at lower temperatures, the efficiency is low due to low mobility and at higher temperatures it is low because of rapid desorption. The Rate equation approach has also been used, by solving the following equations in which H_2 product is again assumed to desorb spontaneously:

$$\dot{\mathrm{H}}_C = F - 2\alpha_{cc}\mathrm{H}_C^2 - W_{\mathrm{H}_C}\mathrm{H}_C, \tag{3.12}$$

$$\dot{\mathrm{H}}_2 = \alpha_{cc}\mathrm{H}_C^2. \tag{3.13}$$

Although the two methods yield similar results (high efficiencies for intermediate temperatures), the range of high efficiency is larger for the rate equation approach, as expected, given the low surface coverage at high temperatures. The existence of an entrance channel barrier of 0.2 eV (2300 K) will depress the high efficiency region of the O1 model more strongly than the O2 model because of the lower temperature range of the former.

3.4.3 Rate of H_2 production

In chemical simulations of interstellar clouds, it is the rate of H_2 formation, R_{H_2}, that is the critical process. The rate, which is in units of $\mathrm{cm}^{-3}\ \mathrm{s}^{-1}$, depends on the calculated efficiency η as well as other parameters, as given by the expression

$$R_{\mathrm{H}_2} = \frac{1}{2}\ \eta\ \upsilon_{\mathrm{H}}\ n_{\mathrm{H}}\ \sigma_g\ n_g\ S_{\mathrm{H(T)}} \tag{3.14}$$

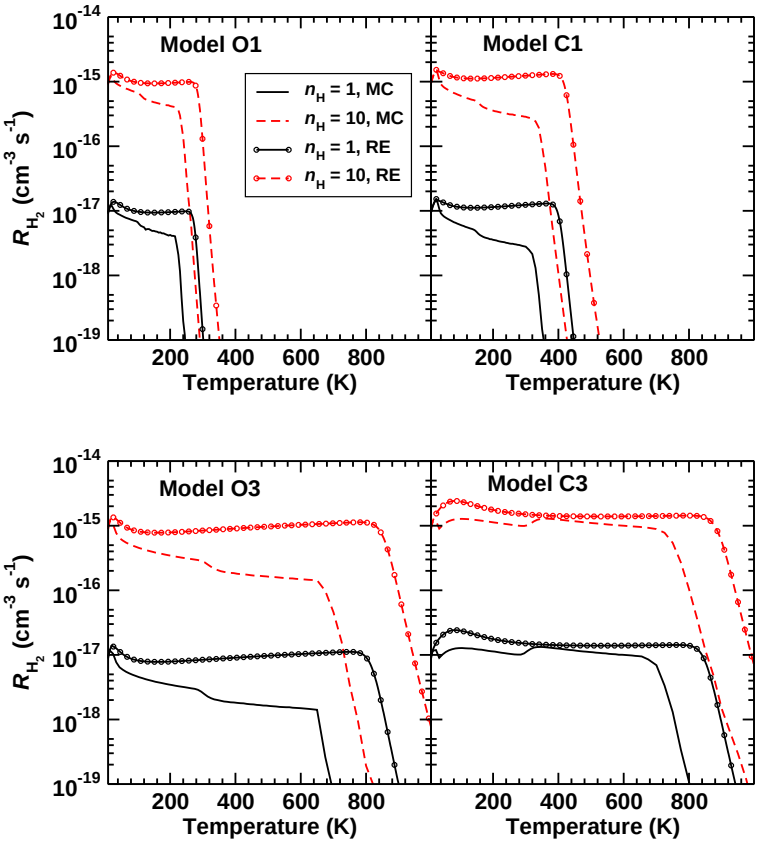

Figure 3.22: Rate of H_2 production for Models O1, C1, O3, and C3 as a function of grain temperature for different atomic hydrogen densities. The results of both Rate equation and Monte Carlo models are shown. The plot is for grains of radius 0.1 μm.

where n_g is the grain number density and $S_{\rm H}$ is the sticking coefficient of the H atoms. There are no experimental data regarding the value of the sticking coefficient as a function of temperature, and we therefore use the expression of Hollenbach & McKee (1979):

$$S_{\rm H(T)} = \left(1 + 0.4 \times \left(\frac{T_g + T_D}{100}\right)^{0.5} + 0.2 \times \frac{T_g}{100} + 0.08 \times \left(\frac{T_g}{100}\right)^2\right)^{-1}. \qquad (3.15)$$

where T_g and T_D are the gas and dust temperatures, respectively, which are here assumed to be the same. Equation (3.14) can also be written in the simple form

$$R_{\mathrm{H}_2} = k n_{\mathrm{H}} (n_{\mathrm{H}} + 2 n_{\mathrm{H}_2}), \tag{3.16}$$

where k is a rate coefficient with units cm^3 s^{-1}. Equation (3.16) is derived using the dust-to-gas number density ratio to convert the grain density to the density of hydrogen nuclei. This ratio is normally taken to be 1.3×10^{-12} for grains with radius 0.1μm.

To obtain overall rates, we use two values of the atomic hydrogen density, $n_{\mathrm{H}} =$ 1 cm^{-3} and $n_{\mathrm{H}} = 10$ cm^{-3}, and neglect any hydrogen in molecular form. The absolute rates we obtain do not really apply to cold dense clouds, where the surface is covered with ices.

Our plots of calculations of R_{H_2} in Figure 3.22 for Models O1, C1, O3, and C3 as a function of temperature for grains of radius 0.1 μm do show the effect of chemisorption in extending the temperature range of large rates to much higher temperatures as compared with pure physisorption models, especially for Models O3 and C3. These models contain deep chemisorption wells, as can be seen in Table 3.1, but differ slightly from O2 and C2 in having a slightly wider and shallower physisorption-chemisorption barrier (Cazaux & Tielens, 2004). We plot results for both the Rate equation approach and our Monte Carlo simulation; as expected from our efficiency calculations, the rates for H_2 formation obtained by the former tend to be larger and to extend to higher temperatures.

Table 3.2: Calculated Efficiencies for H_2 Recombination as a Function of Temperature for Models O3 and C3. (^{a} atomic hydrogen density in units of cm^{-3})

T (K)	Olivine (Model O3) η_o		Carbon (Model C3) η_c	
	$n_H = 1^a$	$n_H = 10$	$n_H = 1$	$n_H = 10$
5	1.00(+00)	9.99(-01)	9.87(-01)	9.87(-01)
15	1.00(+00)	1.00(+00)	9.91(-01)	9.90(-01)
25	6.90(-01)	6.90(-01)	7.86(-01)	7.87(-01)
35	4.28(-01)	4.28(-01)	5.01(-01)	5.04(-01)
45	3.16(-01)	3.16(-01)	5.00(-01)	4.99(-01)
55	2.62(-01)	2.62(-01)	4.94(-01)	4.94(-01)
65	2.25(-01)	2.25(-01)	4.82(-01)	4.84(-01)
75	1.97(-01)	1.97(-01)	4.67(-01)	4.69(-01)
85	1.77(-01)	1.77(-01)	4.51(-01)	4.51(-01)
95	1.60(-01)	1.60(-01)	4.32(-01)	4.32(-01)
105	1.46(-01)	1.46(-01)	4.12(-01)	4.12(-01)
115	1.34(-01)	1.34(-01)	3.90(-01)	3.91(-01)
125	1.24(-01)	1.24(-01)	3.71(-01)	3.73(-01)
135	1.16(-01)	1.16(-01)	3.56(-01)	3.55(-01)
145	1.09(-01)	1.09(-01)	3.38(-01)	3.38(-01)
155	1.02(-01)	1.02(-01)	3.22(-01)	3.22(-01)
165	9.65(-02)	9.65(-02)	3.09(-01)	3.07(-01)
175	9.14(-02)	9.14(-02)	2.95(-01)	2.94(-01)
185	8.67(-02)	8.67(-02)	2.80(-01)	2.81(-01)
195	8.24(-02)	8.24(-02)	2.69(-01)	2.69(-01)

Continued on next page

Table 3.2 – *Continued from previous page*

205	7.88(-02)	7.88(-02)	2.59(-01)	2.58(-01)
215	7.52(-02)	7.52(-02)	2.48(-01)	2.48(-01)
225	7.21(-02)	7.21(-02)	2.38(-01)	2.39(-01)
235	6.93(-02)	6.92(-02)	2.29(-01)	2.30(-01)
245	6.66(-02)	6.65(-02)	2.21(-01)	2.22(-01)
255	6.40(-02)	6.42(-02)	2.13(-01)	2.14(-01)
265	6.17(-02)	6.19(-02)	2.07(-01)	2.07(-01)
275	5.94(-02)	5.96(-02)	2.01(-01)	2.00(-01)
285	5.65(-02)	5.75(-02)	1.98(-01)	1.94(-01)
295	5.20(-02)	5.49(-02)	2.03(-01)	1.90(-01)
305	4.67(-02)	5.15(-02)	2.17(-01)	1.92(-01)
315	4.21(-02)	4.66(-02)	2.30(-01)	2.01(-01)
325	3.91(-02)	4.24(-02)	2.38(-01)	2.14(-01)
335	3.69(-02)	3.88(-02)	2.38(-01)	2.23(-01)
345	3.56(-02)	3.67(-02)	2.37(-01)	2.26(-01)
355	3.42(-02)	3.46(-02)	2.32(-01)	2.26(-01)
365	3.28(-02)	3.33(-02)	2.26(-01)	2.23(-01)
375	3.20(-02)	3.23(-02)	2.20(-01)	2.18(-01)
385	3.11(-02)	3.14(-02)	2.14(-01)	2.13(-01)
395	3.05(-02)	3.06(-02)	2.09(-01)	2.08(-01)
405	2.97(-02)	2.96(-02)	2.04(-01)	2.03(-01)
415	2.90(-02)	2.89(-02)	1.99(-01)	1.98(-01)
425	2.85(-02)	2.83(-02)	1.94(-01)	1.93(-01)
435	2.76(-02)	2.77(-02)	1.88(-01)	1.89(-01)
445	2.70(-02)	2.69(-02)	1.85(-01)	1.85(-01)

Continued on next page

Table 3.2 – *Continued from previous page*

455	2.65(-02)	2.63(-02)	1.80(-01)	1.80(-01)
465	2.58(-02)	2.59(-02)	1.75(-01)	1.76(-01)
475	2.53(-02)	2.54(-02)	1.72(-01)	1.72(-01)
485	2.47(-02)	2.48(-02)	1.68(-01)	1.68(-01)
495	2.43(-02)	2.43(-02)	1.65(-01)	1.65(-01)
505	2.38(-02)	2.38(-02)	1.62(-01)	1.61(-01)
515	2.34(-02)	2.35(-02)	1.58(-01)	1.58(-01)
525	2.29(-02)	2.29(-02)	1.55(-01)	1.55(-01)
535	2.24(-02)	2.25(-02)	1.52(-01)	1.52(-01)
545	2.20(-02)	2.20(-02)	1.49(-01)	1.49(-01)
555	2.17(-02)	2.17(-02)	1.46(-01)	1.46(-01)
565	2.15(-02)	2.13(-02)	1.43(-01)	1.43(-01)
575	2.10(-02)	2.10(-02)	1.41(-01)	1.41(-01)
600	2.01(-02)	2.00(-02)	1.35(-01)	1.35(-01)
625	1.92(-02)	1.92(-02)	1.29(-01)	1.29(-01)
650	1.83(-02)	1.86(-02)	1.23(-01)	1.24(-01)
675	3.31(-03)	1.24(-02)	1.08(-01)	1.18(-01)
700	9.08(-04)	5.73(-03)	8.66(-02)	1.11(-01)
725	2.23(-04)	1.95(-03)	4.11(-02)	9.54(-02)
750	4.15(-05)	4.08(-04)	1.57(-02)	6.55(-02)
775	1.23(-05)	1.13(-04)	4.06(-03)	3.20(-02)
800	2.34(-06)	2.24(-05)	1.26(-03)	1.22(-02)
825	7.69(-07)	1.02(-05)	4.15(-04)	4.14(-03)

For modelers interested in running high-temperature models that include H_2 forma-

tion on surfaces with deep chemisorption wells, we have provided Table 3.2, in which Monte Carlo results for H_2 recombination efficiencies using Models O3 and C3, which show the largest high-temperature efficiencies, are listed as a function of temperature for two different atomic hydrogen densities: 1 cm^{-3} and 10 cm^{-3}. To use Table 3.2, one needs to use the following formula to calculate the H_2 formation rate:

$$R_{H_2} = \frac{1}{2} \left(\eta_o \theta + \eta_c \phi\right) \upsilon_H \, n_H \, \sigma_g \, n_g \, S_{H(T)}. \tag{3.17}$$

Here θ and ϕ are the fractions of silicate and carbonaceous grains respectively, η_o is the efficiency on silicate grains and η_c is the efficiency on carbonaceous grains and all other factors are the same as in Equation (3.14). It is to be noted that, for Models O3 and C3, the efficiency does not depend on atomic hydrogen number density in the range calculated (0.1 - 100 cm^{-3}) below 650 K. This effect is similar to what occurs in Model O1, where the efficiency does not depend on hydrogen number density below 200 K, as shown in Figure 3.17. Thus, although the efficiency values tabulated in Table 3.2 are for atomic hydrogen number densities of 1 and 10 cm^{-3}, these values can be used for a cloud with any atomic hydrogen number density (including warm dense clouds) in the range calculated provided the dust temperature is below 650 K. A similar story concerns grain size: although grains of radius 0.1μm were used to determine the efficiencies, there is little dependence of efficiency on granular size below 650 K.

3.5 Summary

With the simple physisorption-chemisorption model of Cazaux & Tielens (2004) and the use of the CTRW Monte Carlo method, we have studied the formation of H_2 on the surface of interstellar dust grains of olivine and carbon over a wide dust temperature

range from 5 - 825 K. Our major conclusion is that reasonable efficiencies for H_2 recombination can occur at temperatures up to $\approx$ 700 K if deep chemisorption wells (30,000 K) coexist with weak physisorption sites. Our results are only in fair agreement with those obtained by the Rate equation approach at lower temperatures (Cazaux & Tielens, 2004, 2010). As the temperature increases, the discrepancy increases strongly. The Rate equation method gives a much wider range of temperatures for reasonable production of H_2, approaching a high-temperature limit of 1000 K for models with deep chemisorption wells.

Both the Monte Carlo method and the Rate equation method show that the temperature range of efficient recombination decreases as the chemisorption wells are made more shallow, and that for pure physisorption the temperature range is minuscule and at very low temperature only for both olivine and carbon, confirming the work of Katz et al. (1999). Using a rough rather than a flat surface enlarges the temperature range somewhat, as in the prior work of Cuppen & Herbst (2007), but the effect of roughness is much smaller than the effect of even relatively weak chemisorption wells.

We investigated the mechanism of H_2 formation in some detail, and confirmed the result of Cazaux & Tielens (2004) that tunneling, if it actually occurs, plays a significant role in H_2 formation at low temperatures, but with the increase of surface temperature, the thermal mobility of adatoms increases rapidly and thermal hopping of H atoms dominates. We also investigated the dependence of the recombination efficiency over a wide temperature range on the hydrogen atom flux and on grain size. For grains with physisorption and chemisorption sites, we found that the effects were strong only at the highest temperatures, where higher fluxes and larger grain sizes lead to higher efficiencies over larger temperature ranges. Throughout the paper, we have looked at fractional surface coverage as a method of determining in detail what processes are occurring, but coverage can be a misleading indicator if not looked at carefully. For

example, low coverage could mean a very high efficiency, in which all H atoms landing on the grain quickly react to form H_2, which is immediately ejected. Or low coverage can mean low efficiency, because the atoms desorb quickly rather than react. At higher temperatures, where desorption is rapid, low coverage would tend to correlate with low efficiency, whereas at lower temperatures, where desorption can be slow, low coverage can correlate with high efficiency. Only at high temperatures with rapid desorption is the simple explanation that low coverage leads to a discrepancy between the kinetic Monte Carlo calculations and Rate equation calculations correct. The explanation is even more complex with our physisorption-chemisorption models.

We also considered a model, based on models O1 and O2, that incorporates direct adsorption into barrierless chemisorption sites and diffusion only into other chemisorption sites. We found a simple temperature dependence in which the H_2 formation efficiency is high only at intermediate temperatures. The results obtained with Rate equations are similar to those from our kinetic Monte Carlo calculation except at high temperatures, where the efficiency with Rate equations is higher because of the low coverage.

For use in chemical simulations of interstellar clouds, we tabulated the efficiency of H_2 formation obtained with our Monte Carlo simulations for our standard physisorption-chemisorption model using flat models (O3 and C3), which contain deep chemisorption wells for both olivine and carbon surfaces with features that allow H_2 formation at the highest temperatures. Table 3.2 lists our results over the dust temperature range 5 - 825 K for two values of the atomic hydrogen density. At temperatures under 650 K, the results are independent of atomic hydrogen density and grain size over the range calculated. The tabulated efficiencies can then be used in the formula for the rate of molecular hydrogen formation, as shown in Equation (3.17).

References

Acharyya, K., Chakrabarti, S. K., & Chakrabarti, S. 2005, MNRAS, 361, 550

Biham, O., Furman, I., Pirronello, V., & Vidali, G., 2001, ApJ., 553, 595.

Cazaux, S., Caselli, P., Tielens, A. G. G. M., Le Bourlot, J., & Walmsley, M. 2005, J. Phys. Conf, Proc., 6, 155

Cazaux, S., & Tielens, A. G. G. M., 2002, ApJ, 575, L29.

Cazaux, S., & Tielens, A. G. G. M., 2004, ApJ, 604, 222.

Cazaux, S., & Tielens, A. G. G. M. 2010, ApJ, 715, 698

Chang, Q., Cuppen, H.M., & Herbst, E., 2005, A&A, 434, 599.

Chang, Q., Cuppen, H.M., & Herbst, E., 2006, A&A, 458, 497.

Cuppen, H.M., & Herbst, E., 2005, MNRAS, 361, 565.

Cuppen, H. M., & Herbst, E. 2007, ApJ, 668, 294

Cuppen, H.M., Morata, O., Herbst, E., 2006, MNRAS, 367

Doty, S. D., Schoier, F. L. & van Dishoeck, E. F., 2004, A&A 418, 10211034

Gould, R.J. & Salpeter, E.E. 1963, ApJ, 138, 393.

Hirashita, H., Hunt, L. K., & Ferrara, A., 2002, MNRAS, 330, L19-L23.

Hollenbach, D., & McKee, C. F. 1979, ApJS, 41, 555

Hollenbach, D., & Salpeter, E.E., 1970, J. Chem. Phys., 53, 79.

Hollenbach, D., & Salpeter, E.E., 1971, ApJ, 163, 155.

Hornaeker, L. et al. 2006, Phys. Rev. Letters, 96, 156104

Iqbal, W., Acharyya, K., & Herbst, E. 2012, ApJ, 751, 581

Ivanovskaya, V. V., Zobelli, A., Teillet-Billy, D., Rougeau, N., Sidis, V., & Briddon, P. R. 2010, Eur. Phys. J., B76, 481

Jeloaica, L., & Sidis, V., 1999, Chemical Physics Letters, 300, 157.

Katz N., Furman I., Biham O., Pirronello V., & Vidali G., 1999, ApJ, 522, 305

Kolasinski, K. W. Surface Science (Chichester, John Wiley Ltd)

Kreckel, H., Bruhms, H., Ĉížek, M., Glover, S. C. O., Miller, K. A., Urbain, X., & Savin, D. W. 2010, Science, 329, 69

Li, A., & Draine, B.T., 2001, ApJ, 554, 778.

ch3:Messiah, A., 1961, Quantum Mechanics, Vol. 1, (Amsterdam: North-Holland).

Harada, N., Herbst, E. & Wakelam, V., 2010, ApJ, 721, 1570

Perets, H. B. et al. 2007, ApJ, 661, L163

Pirronello, V., Liu, C., Shen L., & Vidali, G. 1997a, ApJ, 475, L69.

Pirronello, V., Biham, O., Liu, C., Shen L., & Vidali, G. 1997b, ApJ, 483, L131.

Pirronello, V., Liu, C., Roser J.E, & Vidali, G. 1999, A&A, 344, 681.

Tielens, A. G. G. M. & Hollenbach, D., 1985, ApJ, 291, 722.

Tielens, A. G. G. M. & Hollenbach, D., 1985, ApJ, 291, 747.

Zecho, T., Guttler, A., Sha, X., Jackson, B., & Kuppers, J. 2002, J. Chem. Phys., 117, 8486

4 H_2 Formation in Diffuse Clouds: A New Kinetic Monte Carlo Study

4.1 Introduction

In the Chapter 3, we discussed H_2 formation over a wider range of parameters for fixed size grains. However, in reality grains are distributed in various sizes. The effect of size distribution on molecular formation is relatively unexplored aspect. How does the presence of different sized grains with different temperature affects the molecular formation is an important qustion to ask. In this chapter, we will discuss affects of size distribution for molecular hydrogen formation. In the next chapter we will discuss it for water formation.

Recent studies established two facts: (i) H_2 formation efficiency is highly temperature sensitive and (ii) efficiency of H_2 formation is dependent on grain size, although not as profusely as its dependence on temperature but efficiency for bigger grains is higher than the smaller grains. Astrophysical environments, have grains which are distributed in various sizes (Mathis et al. (1977); Weingartner & Draine (2001)) and having different

The contents of this chapter has been published in "Iqbal, W., Acharyya, K., & Herbst, E., 2014, ApJ, 784, 139"

temperature. Although, a number of studies of the size-dependence of rates of surface reactions have been undertaken using stochastic techniques (Lipshtat et al., 2004; Cuppen et al., 2006; Iqbal et al., 2012). However, these studies do not evolve different size grains simultaneously. To the best of our knowledge, no study has been undertaken to understand how the diversity of grain sizes with their temperature affects, molecular hydrogen formation in the diffuse interstellar medium. In this chapter, we address this issue.

One goal of this work is to generalize the previous study of Cuppen et al. (2006) for H_2 formation in normal diffuse clouds by including three types of grain surfaces, based on olivine, amorphous silicate, and amorphous carbon, a second granular size distribution, that of Weingartner & Draine (2001), a more diverse collection of surfaces including two with chemisorption binding sites, and two different treatments of the relation between temperature and grain size, one of which derives from the work of Draine & Lee (1984), where average temperatures are used for each grain size, and one in which temperature fluctuations for the smaller grains are followed stochastically. As in the studies of Cuppen et al. (2006) and Iqbal et al. (2012), we utilize the CTRW approach and calculate the efficiency as a function of grain size. Our approach to the calculation is different; however, we utilize a parallel computational algorithm to calculate the efficiencies of different sized grains at the same time. Another goal of this work is to determine whether any granular surface and bonding model can yield a large enough rate coefficient for hydrogen formation to produce the observed amount of H_2 in diffuse clouds within a reasonable amount of time. Finally, we list rates, rate coefficients, and efficiencies η for the formation of H_2 at the initial time, and final efficiencies η_f after 10^7 yr on grains for modelers interested in using them.

The remainder of this chapter is organized as follows, in the first section, we describe the various grain size distributions utilized and their implementation, as well as the gas

and grain temperatures used in our study. In the next section, we briefly discuss various physical processes that are involved in H_2 formation, then in the following section, we discuss our chemical model. In the last section we show our results for various models.

4.2 Grain-size Distributions and Temperatures

In earlier calculations done on dense cloud chemistry by (Acharyya et al., 2011), they used two distributions, labeled MRN and WD according to the last names of the authors (Mathis et al., 1977; Weingartner & Draine, 2001). In the MRN distribution, the normalized number density of grains in the radius range r to $r + dr$ is given by the expression

$$\psi = \frac{1}{n_{\rm H}} \frac{dn_{\rm gr}}{dr} = Cr^{-3.5}; r_{min} < r < r_{max} \tag{4.1}$$

where C is the grain constant and r is the grain radius. This relation is valid between $r_{min} = 50$Å (5 nm) and $r_{max} = 0.25$ μm. The grain constant C is $10^{-25.13}$ ($10^{-25.11}$) cm$^{2.5}$ for carbon (silicates) according to Weingartner & Draine (2001). These authors also derived different size distributions for silicates and carbonaceous material. Their silicate distribution has a smaller negative exponent for the grain radius than the MRN distribution, while their carbonaceous distribution, which extends down to a grain radius of 3.5 Å, has three peaks, one for classical grains, one for "very small grains," and one for PAH's. The WD size distribution contains many parameters, among which we chose values suitable for diffuse interstellar clouds: $R_v = 3.1$, Case A, and $b_c = 3 \times 10^{-5}$ from Table 1 of Weingartner & Draine (2001).

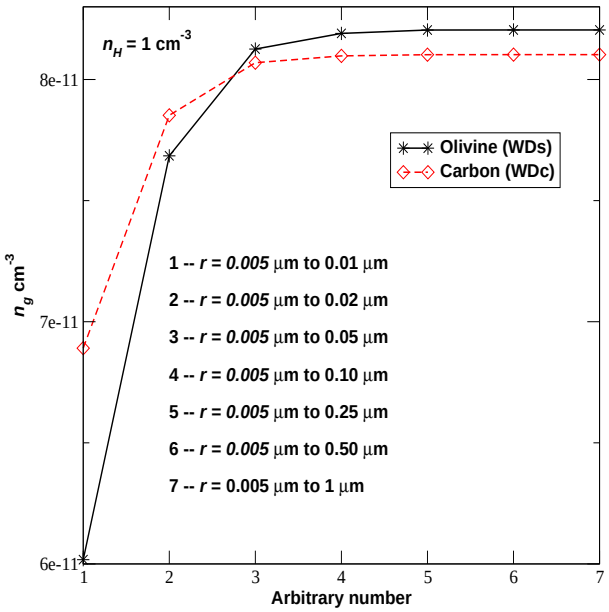

Figure 4.1: Integrated grain number density over various ranges marked as 1, 2 ..,7 for WD model.

4.2.1 Implementation of Grain Size Distributions

Studying H_2 formation using the CTRW Monte Carlo method requires a large amount of computational time. In addition, if one makes such a study with a distribution of grain sizes, the problem is magnified even if, as done here, the calculation is performed using a large number of parallel processors so that the grains can be studied simultaneously. To keep the computational time manageable, one also needs to pay attention to two factors. First, a size distribution has a wide range of sizes and the larger the grain size the longer the computational time. Secondly, a size distribution essentially refers to an infinite number of grains; however, considering a very large number of grains is also impractical from the computational viewpoint. To address the first question, for a cloud of gas density $n_{\rm H} = 1$ cm^{-3}, we calculated the integral grain number density for various size ranges from a minimum radius of 0.005 μm to assorted maximum radii, using the WD size distributions and plotted the results in Figure 4.1. It can be seen that points 4, 5, 6 and 7 lie almost in a straight horizontal line, which implies that olivine and

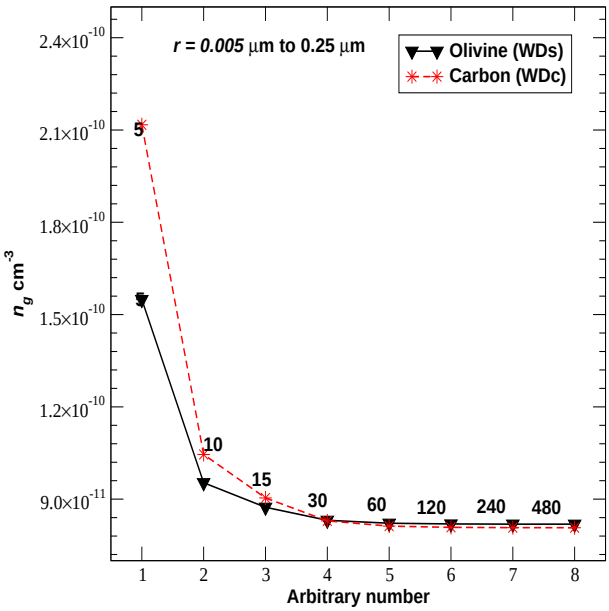

Figure 4.2: Integrated grain number density for various number of intermediate points in between 0.005 μm and 0.25 μm.

carbonaceous grains with a radius larger than 0.1 μm provide almost no contribution to the total grain number density and hence can be neglected. To be safe, we considered grains with radii between 0.005 μm and 0.25 μm.

Because the WD size distributions are complex functions, a sizable number of points in between the minimum and maximum radii is needed to simulate them. Moreover, the distributions for silicate and carbonaceous grains are significantly different. Consequently, we divided the entire range of sizes to be studied into ranges defined by various numbers of logarithmically equally-spaced intermediate points (e.g. 5, 10, 15, 30 ... 480). We then determined the total grain number density in the range between the minimum and maximum radii as a function of the number of intermediate points for both the silicate (WDs) and carbonaceous (WDc) distributions. The results are plotted in Figure 4.2, which shows that there is no appreciable change in the integrated grain number density when the number of points lies above 60. Based upon available computer nodes, we performed our calculations with 78 differently sized grains in between 0.005 μm and

0.25 μm. Schematic of HPC nodes is shown in Figure 4.3. Thus we have 78 grain radii

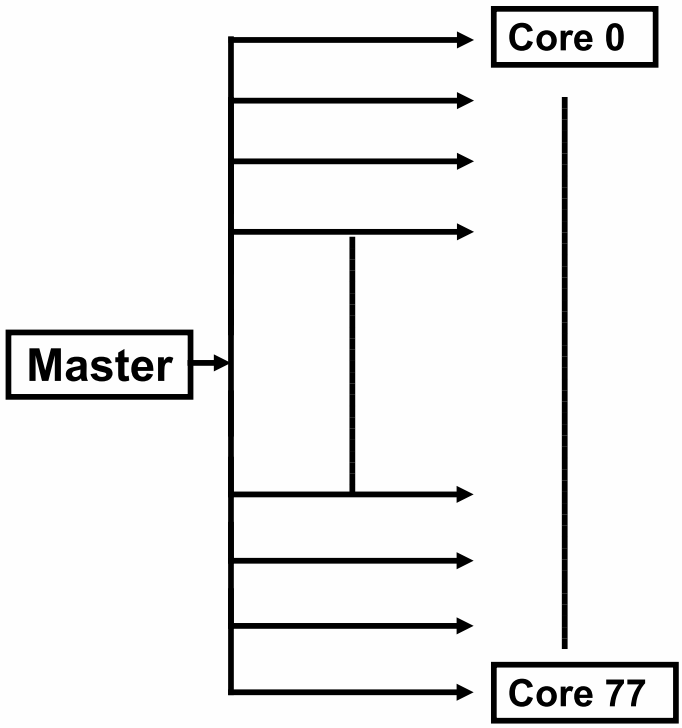

Figure 4.3: Schematic diagram of parallel computing nodes, each core exchange data using MPI scheme.

and 78 grain number densities in the overall range. Integrations over the range of grain radii for rates and rate coefficients are carried out discretely with results first obtained for the binned range around each of the 78 radii. A similar approach was undertaken in earlier papers (Acharyya et al., 2005, 2011), but with a much smaller number of different grain sizes. Since the integrated grain number density in the MRN model is a definite integral, little error is introduced even if we consider fewer points. Moreover, there is little difference in the MRN size distributions for silicate and amorphous carbon grains.

Under certain circumstances, the surface area of a grain is critical for the rate of formation of H_2, as will be shown later. We obtained effective cross sections, $\sigma_{r,i}$, by multiplying the actual grain cross section by the fractional number density of grains in

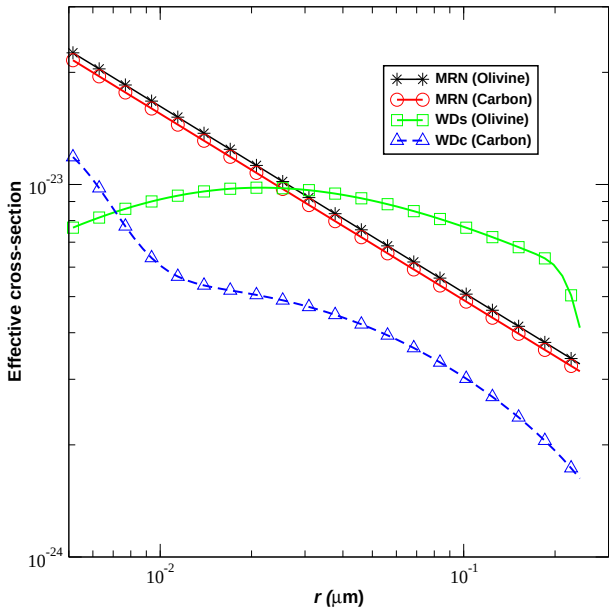

Figure 4.4: Effective cross-section as a function of grain radius for various grain size distributions is plotted.

each binned range. The total effective cross section for each distribution, $\sigma_{r,t}$, is the sum of the $\sigma_{r,i}$. Figure 4.4 shows the effective cross sectional area vs granular size for all the size distributions utilized, while Table 4.1 shows the total effective cross sections. It is clear from Figure 4.4 and Table 4.1 that the MRN models have the largest total effective cross sectional area, with very little difference between them. For the WD distributions; however, the total effective surface area for WDs is nearly 1.8 times larger than for WDc. Another important point is that, in the MRN and WDc cases, the smallest grains have the largest effective surface area, while for the WDs case, the intermediate grains have the highest effective surface area. Note that the effective surface area for the MRN model follows a simple $r^{-1/2}$ dependence, which comes from the fact that unlike the continuous distributions, our discrete distributions in terms of number density, which are divided into binned ranges, follow an $r^{-2.5}$ rather than an $r^{-3.5}$ law.

Table 4.1: Effective total surface area for different models.

Effective Surface area (cm^2)	Model
5.94(-22)	Olivine (MRN)
4.97(-22)	Olivine (WD)
5.68(-22)	Carbon (MRN)
2.82(-22)	Carbon (WD)

4.2.2 Gas and Grain Temperatures

We fixed the gas temperature at 90 K, which is appropriate for a diffuse cloud. Several different densities were used, as discussed below. The grain temperature greatly depends on its composition, the interstellar radiation field, and the size of the grain. It is already established through various experimental and numerical simulation results that the molecular hydrogen formation efficiency is highly sensitive to the grain temperature (Katz et al., 1999; Cuppen & Herbst, 2005; Iqbal et al., 2012). For a flat surface, the efficiency of the process is high (near unity) only over a very narrow temperature range of a few degrees (Katz et al., 1999), depending upon the flux of incident H atoms to some extent and whether or not tunneling occurs. For rough surfaces, with sites of different desorption energies and diffusive barriers, the temperature range of high efficiency can be broadened to higher temperatures significantly (Cuppen & Herbst, 2005), whereas for surfaces with chemisorption sites, the efficiency can remain high for grain temperatures above 500 K (Iqbal et al., 2012). Therefore, it is important to assign an appropriate temperature for each granular size. To optimize the computational time, and to get a full picture, we have not calculated grain temperatures using radiative transfer calculations for all models. For most models, we used the steady-state grain temperature as a function of grain radius calculated by Draine & Lee (1984) for $A_V = 0$. Our value of carbon comes from their calculations using graphite. An erratum for graphite suggests that errors of 15% may have occurred. For olivine, the average grain temperature ranges

from 18 K at a radius of 0.01 μm to 15 K at a radius of 0.2 μm, while for carbon, the analogous range is from 20 K to 17 K. The variation of temperature with grain size has the effect of broadening the temperature range of reasonable efficiency. For selected runs, we calculated the temperature fluctuations as a function of granular size, and used the fluctuating temperatures in our determinations of the H_2 formation efficiency, rate, and rate coefficient.

The rate of photons absorbed by a grain depends on its position in the cloud and on its optical properties. The distribution of photons absorbed by the grain per second per wavelength interval as a function of wavelength is given by

$$P_\lambda = \pi r^2 I_\lambda Q_{abs}(\lambda) D_\lambda, \tag{4.2}$$

with r the radius of the grain, I_λ the interstellar radiation field in photons per unit area per second per unit wavelength, Q_{abs} the wavelength-dependent absorption coefficient, and D_λ the reduction factor due to attenuation of the radiation field by dust. For the interstellar radiation field I_λ, in the wavelength range of 91.2 - 250 nm, we used an expression provided by Sternberg (1988), and for wavelengths between 250 nm and 1 cm, from Zucconi, Walmsley & Galli (2001). The interstellar radiation field at wavelengths above 0.1 μm can be represented by the sum of four contributions: (1) an optical-NIR component peaking at $\lambda_{\rm p} = 1$ μm, due to the emission of disk dwarf and giant stars; (2) the diffuse FIR emission from dust grains, peaking at $\lambda_{\rm p} = 100$ μm; (3) mid–IR radiation from small non–thermally heated grains in the range 5–100 μm and (4) the cosmic background radiation, peaking at $\lambda_{\rm p} = 1$ mm. The value of Q_{abs} for low photon energy is obtained from (Bohren & Huffman (1983)), and, for smaller wavelengths, the r dependent value of Q_{abs} is determined following Draine & Lee (1984). Extinction

dependent D_λ, is given by

$$D_\lambda = \exp\left(-0.8\frac{A_\lambda}{A_V}A_V\right). \tag{4.3}$$

We then used table of A_λ/A_V values in Mathis (1990) and Whittet (2003).

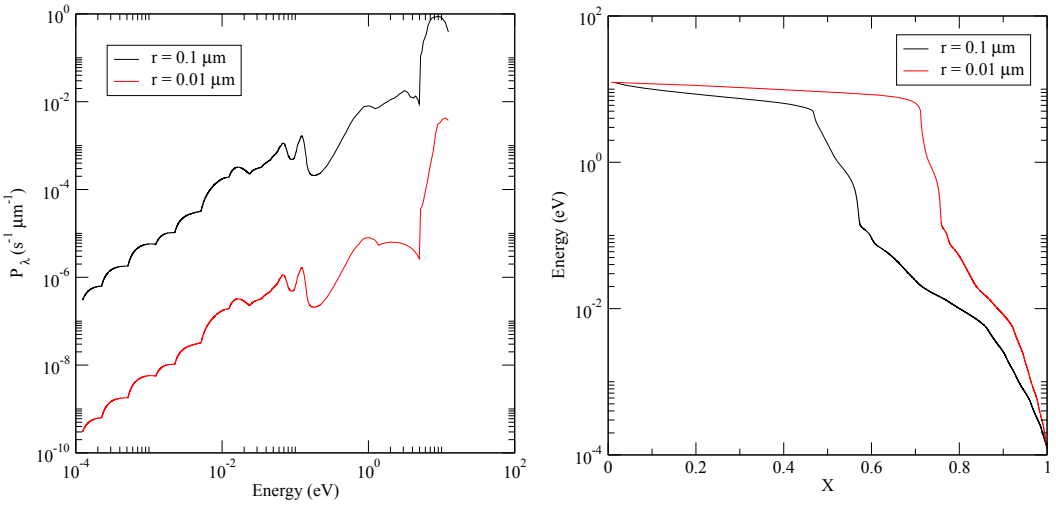

Figure 4.5: Right Panel: The absorbed photon flux in photons per second per wavelength interval for different grain sizes, $r = 0.01$ and 0.1 μm. Left Panel:The relation between the random number and the photon energy for different grain sizes, $r = 0.01$ and 0.1 μm.

The absorbed photon flux in photons per second per wavelength interval for different grain sizes, $r = 0.01$ and 0.1 μm is shown in Figure 4.5(Right Panel). The rate (s^{-1}) of photons absorbed by a grain is

$$R_{photon} = \int_{91.2\text{nm}}^{10\text{mm}} P_\lambda \mathrm{d}\lambda, \tag{4.4}$$

Here we considered photons in the wavelength range 91.2 nm-10 mm. The time between two photon hits is determined using a random number X between 0 and 1. If the grain absorbs a photon, the energy E of the photon is picked from the distribution in Equation (4.2) using a random number. The plot in Figure 4.5 (Left Panel), indicates the relation between the random number, X_λ, and the photon energy. This figure is

obtained using the relation

$$X_\lambda = \frac{\int_{91.2\mathrm{nm}}^{\lambda} P_\lambda \mathrm{d}\lambda}{R_{photon}}, \tag{4.5}$$

which gives a value between 0 and 1 for a given wavelength λ. This value is a function of grain sizes and visual extinctions. The r dependence comes from the absorption coefficient. The new temperature of the dust grain is then obtained by solving

$$E = \int_{T_{old}}^{T_{new}} c(T)\mathrm{d}T, \tag{4.6}$$

for T_{new}, where $c(T)$ is the heat capacity. According to (Draine & Li, 2001; Aannestad & Kenyon, 1979; Purcell, 1976), olivine can be approximated by a Debye solid with a Debye temperature of 500 K. The temperature of the grain is recalculated at certain time intervals using,

$$\Delta t = -\int_{T_{new}}^{T_{old}} \frac{c(T)}{\frac{\mathrm{d}E}{\mathrm{d}t}}\mathrm{d}T, \tag{4.7}$$

where, $\frac{\mathrm{d}E}{\mathrm{d}t}$ is given by

$$\frac{\mathrm{d}E}{\mathrm{d}t} = 4\pi\left(\pi a^2\right)\int_0^\infty Q_{em}\left(\lambda\right)B_\lambda\left(T\right)\mathrm{d}\lambda, \tag{4.8}$$

with Q_{em}, the emission coefficient and B, the Planck function. We have taken the values of Q_{em} from Cuppen et al. (2006). We integrated Equation (4.8) numerically over the range 91.2 nm $< \lambda \leq$ 10 mm and solved Equation (4.7) to obtain the new temperature. Temperature fluctuations for selected grain sizes are shown in Figure (4.6). Two important aspects of this plot are (i) as the grain size increases, the temperature fluctuations decrease significantly in intensity, and (ii) the number of photons hitting the grains per unit time increases with the increase in grain radius, so that the number of temperature spikes per unit time increases as well. Thus an increase in grain size smears out the effect of the temperature spikes until an average temperature is reached.

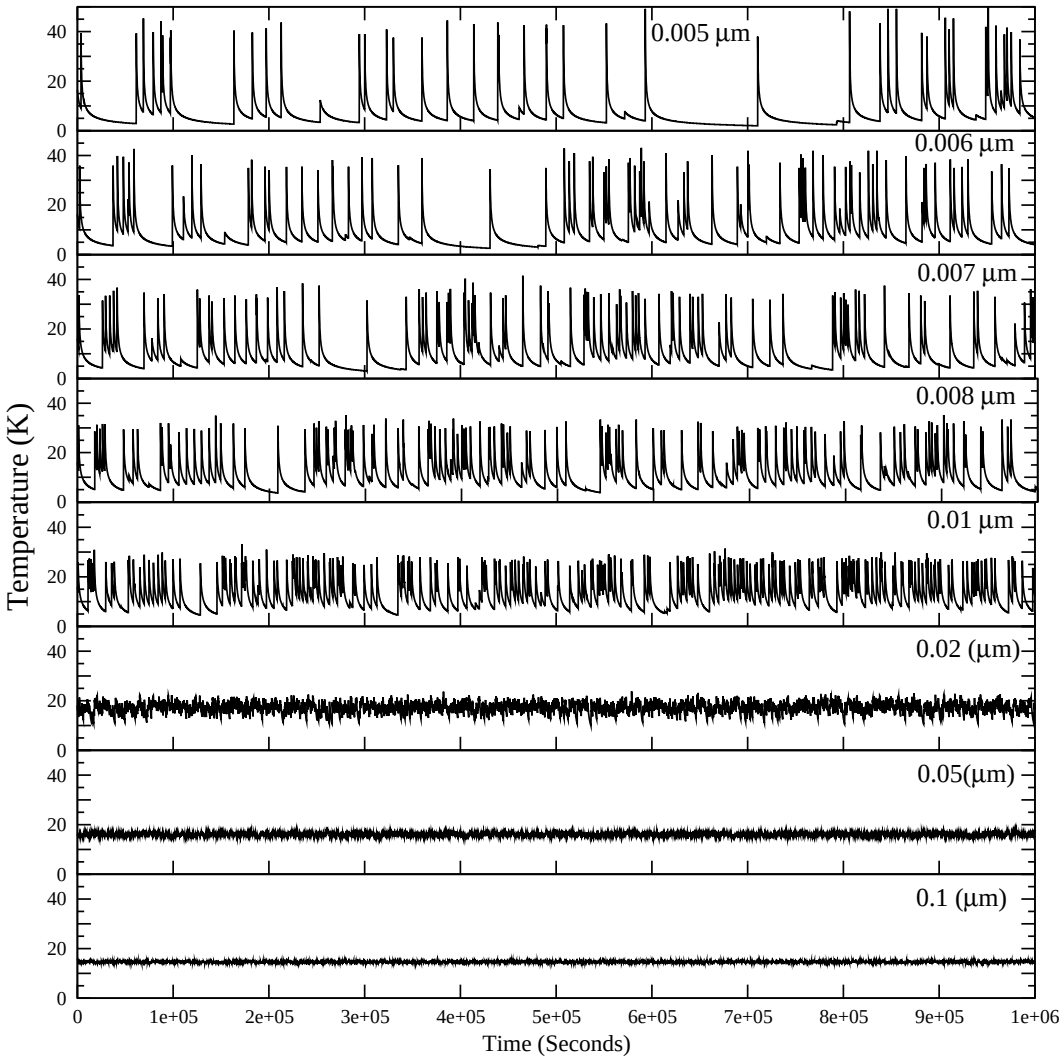

Figure 4.6: Temperature fluctuation for various grain sizes.

Thus, although smaller grains have fewer incoming photons per given time interval, the temperature fluctuations are much larger, which is a consequence of the r^3 term in the heat capacity. For a grain size (radius) of 0.005 μm, fluctuations of up to 50 K occur, while for a grain size of 0.05 μm, an almost constant temperature is obtained. Furthermore, it can be noticed that the minimum temperature reached before each photon hit is almost independent of the height of the temperature increase given the rapid initial cooling. Draine (2003) shows similar graphs for carbonaceous grains, in which the temperature for the grains has similar fluctuations both in amplitude and in

modal temperature.

4.3 Physical Processes for H_2 formation and CTRW approach

Details of physical processes are discussed in Chapter 2, in this Chapter, we discuss, few terms and parameter which are related to this work only. First, we define, rate coefficient k (cm^3 s^{-1}) by the following kinetic equation

$$d[\mathrm{H_2}]/dt = kn(\mathrm{H})n_{\mathrm{H}}, \tag{4.9}$$

where $n(H)$ is the concentration of H atoms and n_{H} is the overall concentration of protons. The expression for k is given by

$$k = \frac{\int_{r_{min}}^{r_{max}} \frac{1}{2}\ v_{\mathrm{H}}\ \eta\ \xi\ \sigma_{\mathrm{gr}}\ [dn_{\mathrm{gr}}(r)/dr]\ dr}{n_{\mathrm{H}}}, \tag{4.10}$$

where $n_{gr}(r)$ is the grain density as a function of radius r, σ_{gr} is the granular cross section, v_H is the thermal speed of gas-phase H atoms, $\eta(r)$ is the efficiency of reaction and ξ is the sticking coefficient of H atoms. For this study we used temperature dependent sticking coefficient, given by the following equation,

$$\xi = \left(1 + 0.4 \times \left(\frac{T_g + T_D}{100}\right)^{0.5} + 0.2 \times \frac{T_g}{100} + 0.08 \times \left(\frac{T_g}{100}\right)^2\right)^{-1}. \tag{4.11}$$

Here, T_g and T_D are the gas and dust temperatures, respectively. At low grain temperatures, the sticking coefficient lies close to unity, but is computed for each grain size using the relevant dust temperatures. The sticking expression relates to the formation of

weak physisorption bonds, which do not involve intermediate barriers. Barriers against the formation of a strong chemisorption bond by an H atom do often exist (Jeloaica & Sidis, 1999; Bachellerie et al., 2009; Ivanovskaya et al., 2010), In Equation 4.10, the integration is over all granular radii from a minimum to a maximum. If all grains have the same radius of 0.1 μm, the gas-to-dust ratio is 10^{12} by number, and the efficiency and sticking coefficient are both unity, the value for k at 100 K is $\approx 2 \times 10^{-17}$ cm^3 s^{-1}. This value is what is needed to reproduce the H_2 abundance in diffuse clouds at steady-state (Jura, 1974). The values of k obtained by Cuppen et al. (2006) in the bare interstellar radiation field at a gas kinetic temperature of 60 K are 1-2 orders of magnitude lower except for the very rough surface, for which k is $1 - 2 \times 10^{-17}$ cm^3 s^{-1}.

In the simulation reported here, H atoms are deposited on a grain lattice. For those models in which physisorption sites are entered first, the standard Langmuir-Hinshelwood rejection mechanism is used, where the incoming H atoms rebound back into the gas if they land on sites already occupied by other H atoms or H_2 molecules. This rejection is removed when direct chemisorption is considered, leading to an Eley-Rideal chemistry. An adsorbed H atom in a physisorption site can hop or tunnel with equal probability to any of the neighboring physisorption sites and with different but equal probability to any of the neighboring chemisorption sites in models where chemisorption exists. If another H atom is sitting on the site reached by a diffusing H atom, an H_2 molecule is formed and either instantly released into the gas phase or left remaining on the site until thermal desorption occurs, depending upon the parameter μ. In our models with direct entry into chemisorption sites, H atoms are not allowed to move, and can only react via the Eley-Rideal mechanism. Similarly, an adsorbed H atom can also desorb from the surface when it gets enough thermal energy to overcome the desorption energy of the grain surface.

To improve the efficiency of the CTRW calculation, we employed parallel compu-

tation. As discussed earlier, a total of 78 CPU's were used, one for each grain size. The relationship between grain size and the size of the square lattice used to represent the grain is defined through the surface site density (Katz et al., 1999) with periodic boundary conditions. The use of parallel architecture reduces the time needed by n-fold, where n is the number of jobs running simultaneously. The approach is useful if we have a problem where we can separate out independent subsystems, such as the grains of different sizes here, yet pass information between them. We used the Message Passing Interface (MPI) scheme for information exchange between CPU's. This approach differs from our previous method in that the gas-grain interaction is coupled. The gas number density is adjusted after a certain time step, say, "dt". As in any parallel computation, one needs to pass information after certain time steps for which one can separate time scales. In this calculation, all grains evolve simultaneously but interact with each other after every step.

So,we start the simulation in parallel computing facility for all 78 grains together. At $t = 0$, the algorithm calculates the accretion rate using an initial atomic hydrogen number density. Since the accretion rate is a function of the granular cross-section, each size grain will have a different accretion rate. All the grains are simultaneously evolved until a quasi steady state is reached. After reaching steady state we calculate efficiency for each of 78 grains. Once the efficiency is calculated, it can be used to calculate the rate coefficient k, as shown in equations (4.9) and (4.10). It can also be used to calculate the total rate R_{H_2} ($\mathrm{cm^{-3}\ s^{-1}}$), given by,

$$R_{\mathrm{H_2}} = \int_{r_{min}}^{r_{max}} \frac{1}{2}\, n(\mathrm{H})\ v_{\mathrm{H}}\ \eta\ \xi\ \sigma_{\mathrm{gr}}\ [dn_{\mathrm{gr}}/dr]\ dr, \tag{4.12}$$

where, the parameters were defined above for equation (4.10). Note that equation (4.12) can be reduced to equation (4.9) by converting n_{gr} to the total proton density n_H through

the dust-to-gas number ratio. Because the formula for the rate contains the concentration of gaseous atomic hydrogen, the rate will have an additional time dependence, especially when the amount of molecular hydrogen builds up significantly. The time dependence is less significant for the rate coefficient and the efficiency, because they do not dependent explicitly on the atomic hydrogen density.

We must then reduce the gas phase atomic hydrogen number density as some portion of it has been converted to molecular hydrogen. To implement this conversion, we further evolve the grains until 0.1 % of atomic hydrogen is converted to H_2. After this conversion occurs, we re-calculate the accretion rate by reducing the H-atom gaseous number density by an equivalent amount. This process of recalculation continues with further equal increments of H-atom loss until all grains evolve for 10^7 yr. For models in which H_2 formation is so slow that it can not convert even 0.1 % atomic H in this time interval, we calculate the H_2 formation rate, rate coefficient, and efficiency after 10^7 yr. It also is to be noted that, since production is very low in the second scenario, the statistical fluctuation is large and the values are only upper limits. This procedure is a major change from earlier models, in which the efficiency is calculated with a fixed number density of atomic hydrogen.

4.4 Results

We have utilized five sets of physical models for the grain surfaces, which are run for olivine, amorphous silicate, and amorphous carbonaceous surfaces, and consider both thermal diffusion (hopping) and tunneling for H-atom mobility. Tunneling probabilities were calculated using the procedure in Cazaux & Tielens (2004, 2010). The models are as follows:

- Model 1 possesses a "flat", or "plain", surface with a single desorption energy and diffusion barrier due to physisorption. Both the diffusion barrier and the desorption energies for H atoms on olivine and amorphous carbon were taken from Katz et al. (1999), while these energies for amorphous silicate were taken from Perets et al. (2007).

- Model 2 possesses multiple binding energies and diffusion barriers, and can be regarded as "rough." The differences are due to lateral bonds as discussed initially by Cuppen & Herbst (2005). This model is very similar to Surface (iii) of Cuppen et al. (2006).

- Model 3 possesses both physisorption and chemisorption binding sites, with diffusion barriers and desorption energies taken from Cazaux & Tielens (2004, 2010). Adsorption occurs into physisorbed sites only, which act as precursors for diffusion over and through barriers into other physisorption and chemisorption sites. Some evidence against this model is discussed in Section 4.4.3.

- Model 4 is based on surfaces with only chemisorbed sites. Adsorption onto these sites is direct and barriered. Molecular hydrogen is formed only by an ER-type, or abstraction, mechanism.

- Model 5 follows temperature fluctuations due to photon bombardment for Models 1 and 3.

In the calculations discussed below, we start with a hydrogen atomic flux corresponding to three different densities: $n(\mathrm{H}) = 1$, 10, and 100 cm^{-3}. We present our simulation results for all of the models in the following subsections. These results consist primarily of efficiencies, rates, and rate coefficients as functions of granular size for the production of H_2 from atomic H. The atomic hydrogen is assumed to be at its initial abundance.

Calculations at times late enough for a significant fraction of the initially atomic gas to become molecular hydrogen will yield different results. To keep track of when this change occurs, we also define a parameter called η_f, which is the percentage of hydrogen atoms that are converted to H_2 in 10^7 yr. Unless stated to the contrary, tunneling is included in the calculations reported.

4.4.1 Model 1: Three Flat Surfaces

As mentioned previously, for olivine, the H-atom diffusion barrier is 287 K and the desorption energy is 373 K (Katz et al., 1999), for amorphous silicate the H-atom diffusion barrier is 406 K and the desorption energy is 510 K (Perets et al. (2007)), and for amorphous carbon these energies are 511 K and 658 K respectively (Katz et al., 1999). The variation of H_2 formation efficiency as a function of grain size and initial H atom density is shown for olivine (labeled crystalline silicate), amorphous silicate, and amorphous carbon in Figure 4.7 (a), (b) and (c), respectively. It can be seen that the H_2 formation efficiency increases with increasing granular size and is strongly dependent on incoming H-atom flux for all surfaces, although the efficiencies for carbon and amorphous silicate are much larger and approach near unity at the largest radii studied for the three gas densities. For olivine grains smaller than 0.02μm, we cannot produce any H_2 over 10^7 yr for the two lower gas densities.

Figure 4.7 (d), (e) and (f) shows the initial rate of hydrogen molecule production as a function of granular size for the same three surfaces. The lines without circles are for calculations with the MRN granular size distribution whereas the lines with circles are for the WD distribution. It can be seen that for both olivine and amorphous silicate with both the MRN and WD distributions, there is little size dependence to the rate above granular radii of 0.1μm, whereas for carbon, the lack of size dependence onsets at

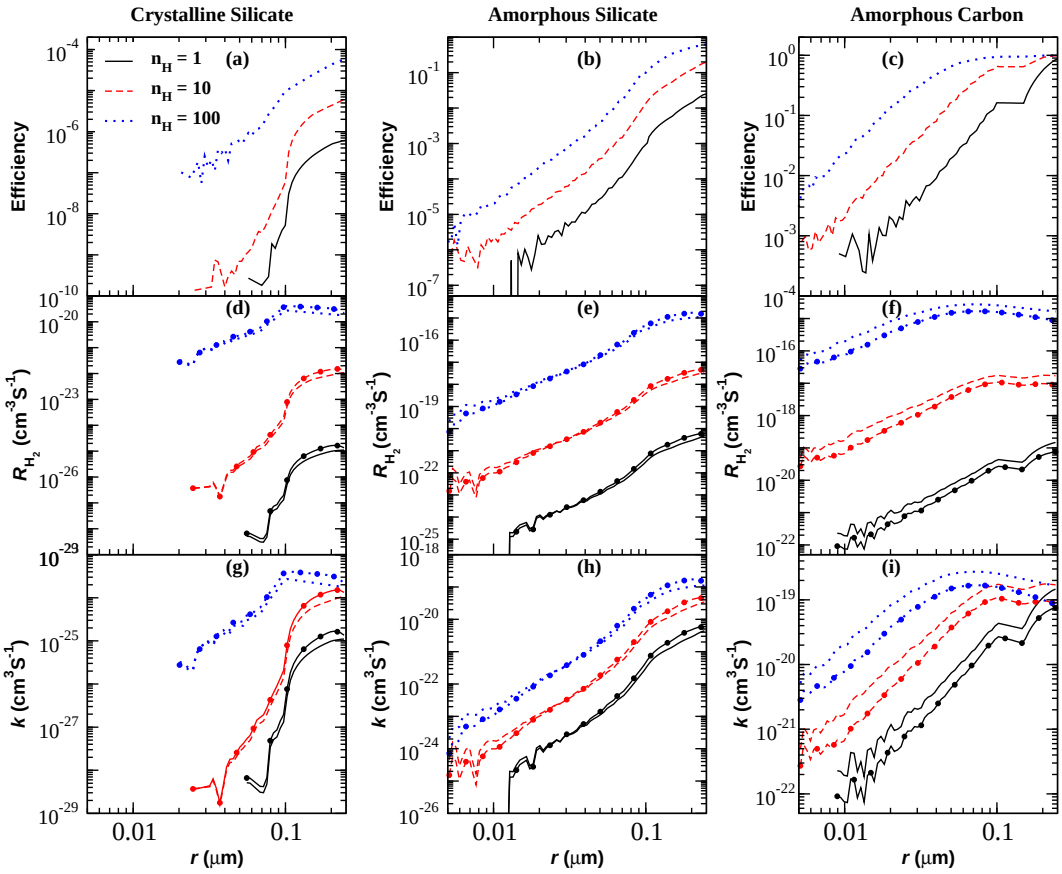

Figure 4.7: Variation of H_2 formation efficiency (a, b and c), formation rate (d, e and f) and rate coefficient (g, h and i) as a function of grain radius for three plain surfaces at times when the atomic hydrogen density (cm^{-3}) is near its initial value ($n(H) = n_H$). The lines with circles are for the WD distributions in this and subsequent figures.

a lower granular radius. When we compare the contribution to the total H_2 formation for each individual grain size for olivine using the MRN distribution, we see that although the effective surface area increases with decreasing grain size, the H_2 recombination rate decreases, initially slowly but beyond 0.1 μm very rapidly. This effect is primarily due to the higher average temperature of the smaller grains. Therefore, a higher effective surface area does not always guarantee more H_2 production because the H_2 recombination rate is a very strong function of temperature. A similar effect is also observed for the WD distribution. For the case of carbon, we found that for $n(H) = 1$ cm^{-3}, the smallest

grains that can produce H_2 have radii of 0.009 μm with fluctuations visible due to very limited H_2 formation. However, for $n(H) = 10$ cm^{-3} and 100 cm^{-3}, all the grains can form H_2 although statistical fluctuations can be found for grains smaller than 0.01 μm.

Panels (g), (h) and (i) of Figure 4.7 show the initial rate coefficients k vs grain radius for the same three surfaces. The olivine values at each radius considered are all quite low, although they increase with grain radius and track the rate curves in Figure 4.7 (d) closely, as expected at times before there is much loss of gaseous atomic hydrogen. The amorphous silicate surface shows a similar trend but possesses rate coefficients higher by 4-5 orders of magnitude. For the case of carbon, the peak rate coefficient occurs in the middle of the range depending somewhat on gas density and grain-size distribution used. The largest rate coefficient occurs with the MRN distribution at a density of 100 cm^{-3} at a grain size of 6-7 $\times 10^{-2}$ μm.

In Table 4.2, we show the total H_2 formation rate R_{H_2}, and the total rate coefficient k at the initial time, as well as η_f, the conversion efficiency (%) of H into H_2 over 10^7 yr, for all the three plain surfaces obtained by integration over the range of grain sizes. The fraction η_f of atomic hydrogen that is converted into molecular hydrogen in 10^7 yr is really an upper limit to the conversion rate since no destruction processes for H_2 are considered. It is found that the conversion of H into H_2 is very inefficient for flat olivine grains and for flat amorphous silicate and carbon grains at the lower gas densities chosen. In fact, the reported rates for olivine at the lowest gas density should be taken with caution, because the number of H_2 atoms formed is not statistically significant even after evolving the system for 10^7 yr.

The MRN distribution H_2 recombination rates for olivine and carbon are lower and higher, respectively, than those with the WD distributions, generally following the effective surface area of large grain sizes that show high reaction efficiencies. Since amorphous

Table 4.2: Integrated H_2 Formation Rate (R_{H_2}), Conversion Efficiency (η_f), and Rate Coefficient (k) for Assorted Models of Types 1, 2, and 3.

Units: η_f unitless (%), R_{H_2} (cm^{-3} s^{-1}), k (cm^3 s^{-1})							
Olivine		MRN			WDs		
Model	Parameter	$n_H = 1^a$	$n_H = 10$	$n_H = 100$	$n_H = 1$	$n_H = 10$	$n_H = 100$
1.	R_{H_2}	1.10(-24)	1.10(-21)	5.31(-19)	1.80(-24)	1.70(-21)	8.09(-19)
	η_f	<1.0(-7)	<1.0(-5)	<8.16(-4)	<1.0(-7)	<1.0(-5)	<5.11(-04)
	k	1.10(-24)	1.10(-23)	5.31(-23)	1.80(-24)	1.70(-23)	8.09(-23)
2.	R_{H_2}	5.2(-21)	5.0(-18)	2.05(-15)	8.0(-21)	7.7(-18)	3.10(-15)
	η_f	<3.0(-4)	<0.03	<2.59	<5.0(-4)	<0.05	<3.92
	k	5.2(-21)	5.0(-20)	2.05(-19)	8.0(-21)	7.7(-20)	3.10(-19)
3.	R_{H_2}	4.1(-17)	4.2(-15)	4.11(-13)	3.5(-17)	3.5(-15)	3.45(-13)
	η_f	<2.6	<26.1	<72.19	<2.2	<21.9	<68.49
	k	4.1(-17)	4.2(-17)	4.11(-17)	3.5(-17)	3.5(-17)	3.45(-17)
Amorphous silicate		MRN			WDc		
Model	Parameter	$n_H = 1$	$n_H = 10$	$n_H = 100$	$n_H = 1$	$n_H = 10$	n_H=100
1.	R_{H_2}	3.60(-20)	3.16(-17)	1.57(-14)	5.55(-20)	4.89(-17)	2.43(-14)
	η_f	< 0.002	< 0.20	< 9.90	< 0.0035	< 0.31	< 15.39
	k	3.60(-20)	3.16(-19)	1.57(-18)	5.55(-20)	4.89(-19)	2.43(-18)
Amorphous Carbon		MRN			WDc		
Model	Parameter	$n_H = 1$	$n_H = 10$	$n_H = 100$	$n_H = 1$	$n_H = 10$	n_H=100
1.	R_{H_2}	1.6(-18)	5.1(-16)	1.10(-13)	9.2(-19)	3.0(-16)	6.30(-14)
	η_f	<0.1	<3.2	<41.10	<0.05	<1.9	<28.55
	k	1.6(-18)	5.1(-18)	1.10(-17)	9.2(-19)	3.0(-18)	6.30(-18)
3.	R_{H_2}	4.1(-17)	4.1(-15)	4.06(-13)	2.0(-17)	2.0(-15)	2.01(-13)
	η_f	<2.6	<25.6	<71.92	<1.3	<12.7	<55.92
	k	4.1(-17)	4.1(-17)	4.06(-17)	2.0(-17)	2.0(-17)	2.01(-17)

[a] Total proton density in units of cm^{-3}

carbon grains have a much higher binding energy, they can retain atomic hydrogen for much longer periods of time at higher temperatures; therefore, even relatively smaller grains can also form H_2 on their surface. Amorphous silicate lies in between since it has a binding energy in between crystalline silicate and amorphous carbon.

The integrated rate coefficients for the three surfaces differ strongly. For olivine, the rate coefficients lie in the range 10^{-22} - 10^{-24} cm^3 s^{-1} and for amorphous silicate between 3.16×10^{-19} and 2.43×10^{-18}. These values lie, respectively, 5-7 orders of magnitude and 1-2 orders of magnitude below the standardly used value of $k \approx 10^{-17}$ cm^3 s^{-1} (Jura,

1974). For carbon, on the other hand, the rate coefficients for flat surfaces lie at more reasonable values, with slightly larger ones for the MRN distribution, with its larger total effective surface area. Note that although in ordinary chemical usage, the rate coefficient should be a constant at a given temperature or set of temperatures, the efficiency term in the formulae for both rate and rate coefficient increases with increasing H-atom flux and density so that these parameters tend to increase with increasing gas density. Thus, users of the rate coefficients reported here should choose the results closest to the density of interest.

We also ran these models without tunneling so that the H-atom mobility is due to hopping only. In this case, neither olivine nor amorphous carbon can produce enough H_2 on the grain surface. The residence time at diffuse cloud grain temperatures is sufficiently small that adsorbed H atoms desorb back to the gas phase before they hop and meet another H atom to form H_2. Tunneling is far more efficient than classical random walk diffusion since the tunneling rate is much higher than the thermal diffusion rate at temperatures in the diffuse cloud regime according to the model of Cazaux & Tielens (2004, 2010). Even then, the H_2 recombination rate is insufficient to build up the diffuse cloud H_2 abundance for olivine and is marginal for amorphous silicate.

4.4.2 Model 2: A Rough Surface

For Model 2, we generated a rough surface for olivine by adding sites with 1, 2, 3, or 4 lateral bonds to the square lattice structure (Chang et al., 2006). We distributed these rough sites randomly such that the total number of any of these sites with a given number of lateral bonds is 10 % of the total number of sites. Thus, if the total number of sites is 100, then 10 sites have 1 lateral bond and another 10 have 2 lateral bonds and so on. Incorporation of a range of desorption energies and diffusion barriers improves

the H_2 formation efficiency for olivine.

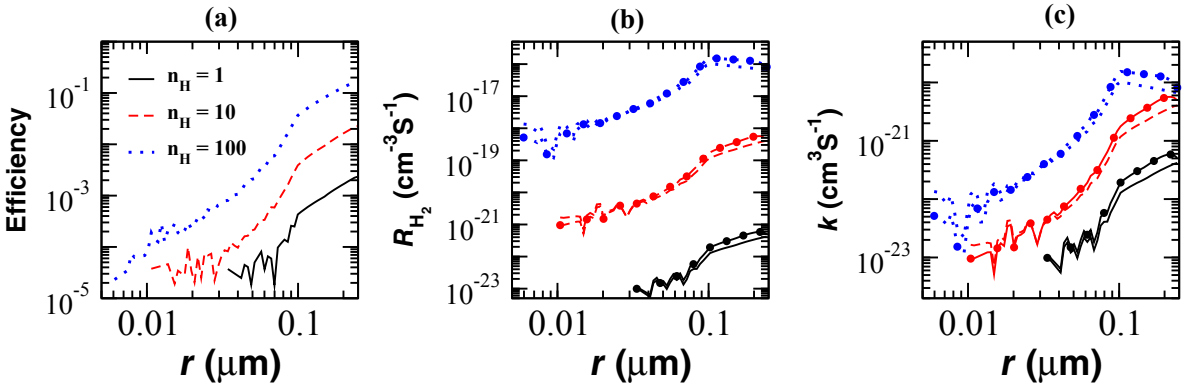

Figure 4.8: Variation of H_2 formation efficiency, formation rate, and reaction rate coefficient as functions of grain radius for olivine (crystalline silicate) with a rough surface at times when the atomic hydrogen density is near its initial value.

Figure 4.8 shows the H_2 formation efficiency, formation rate, and reaction rate coefficient as a function of grain radius for olivine (crystalline silicate). The efficiency is higher by almost four orders of magnitude when compared with the flat surface; however, it is still not adequate to convert even 1% of H into H_2 with either the MRN or the WD distribution and $n_H = 1$ cm^{-3} and $n_H = 10$ cm^{-3} by 10^7 yr, as seen in Table 4.2. For n_H = 100 cm^{-3}, $\sim$ 3-4 % of H is converted to H_2 during this time range. For $n_H = 1$ cm^{-3}, olivine grains smaller than 0.04 μm cannot form H_2 while for $n_H = 10$ cm^{-3}, grains larger than 0.01 μm form H_2 on the surface. However, for $n_H = 100$ cm^{-3} all the grains form H_2 on the surface albeit at low efficiency for the smaller grains. Indeed, the H_2 recombination rate for sizes lower than 0.1 μm goes down rapidly. For small grains, the number of H_2 molecules formed is very small and our results come with large statistical fluctuations. Similar to the case for the flat surface, the H_2 formation efficiency and rate both go down with decreasing grain radius although the small grains have a larger

effective surface area.

The overall rate coefficient for H_2 formation on olivine, shown in Table 4.2, is very low and confirms the result that even at a density of 100 cm^{-3}, H_2 cannot be made efficiently. The value for the MRN distribution at this density can be compared with the value at $A_V = 0$ of Cuppen et al. (2006). Their value is two orders-of-magnitude larger than ours because of the more important role played by small grains in their calculation, which are cooler than ours when modal temperatures are used.

4.4.3 Models 3 and 4: Precursor Mediated and Direct Chemisorption

For implementing chemisorption, we have to consider the role of assorted barriers carefully. One approach to chemisorption, known as precursor-mediated adsorption (Model 3) (Kolasinski, 2002), involves the initial barrierless formation of a weak physisorption bond between the adsorbate and the surface. Reaction can occur via standard Langmuir-Hinshelwood diffusion among the physisorption sites, or the adsorbates can diffuse into a lower layer of chemisorption sites, presumably somewhat offset from the physisorption sites. Reactions occur when two hydrogen atoms reach the same site, either a physisorption or chemisorption site, and unite in a barrierless fashion (Cazaux & Tielens, 2004, 2010). With the standard parameters used for olivine, the efficiency of reaction via this mixed physisorption-chemisorption approach is reasonably high for grain temperatures up to a few hundred Kelvin (Iqbal et al., 2012) and then drops sharply, whereas there is evidence that chemisorption does not begin to take place until much higher temperatures (Perets & Biham, 2006). The discrepancy occurs because the barrier used between precursor physisorption sites and chemisorption sites is rather low - 300 K (26 meV) - compared with measured and calculated values for the barrier to chemisorption. The

second approach (Model 4) is a barriered ("activated") direct chemisorption of the first hydrogen atom onto the surface followed by attack of a second hydrogen atom, leading to reaction and ejection into the gas. Two notations are used to describe the second process: surface scientists refer to it as an Eley-Rideal (ER) mechanism (Kolasinski, 2002), while chemists often label it as an abstraction (Mennella , 2008). In the pure form of this mechanism, no surface diffusion occurs. Two barriers can be involved: the chemisorption barrier of the initial hydrogen atom (Jeloaica & Sidis, 1999), and the barrier against the subsequent chemical reaction. Because several authors have suggested a negligible second (reaction) barrier (Morisset et al., 2004; Mennella , 2008), we assumed the actual reaction to be barrierless.

4.4.3.1 Model 3

For Model 3, we followed a procedure described in detail in Cazaux & Tielens (2004, 2010) and Iqbal et al. (2012) and used chemisorption binding energies, E_C, from Model 1 of Iqbal et al. (2012); i.e., 10,000 K and 14,000 K for olivine and amorphous carbon, respectively. In the dust temperature regime studied, once an H-atom sticks on a chemisorbed site it can neither move nor desorb back in to the gas phase, since the binding is sufficiently strong to prevent these two processes (Iqbal et al. (2012)).

We found that both olivine and amorphous carbon grains can form H_2 efficiently for surfaces with chemisorption sites. As can be seen in Table 4.2, approximately 2.6 %, 26.1 % and 72.2 % of hydrogen are converted into H_2 at 10^7 yr for $n_H = 1$, 10, and 100 cm^{-3} respectively for olivine. For carbon the numbers are similar. This large improvement over the other two models occurs because the presence of chemisorption sites greatly enhances the residence time of H atoms on the grain surface and hence H_2 formation efficiency, especially for the smaller grains. As shown in (Iqbal et al., 2012), the results

are nearly identical if tunneling is removed. Panels (a) and (b) of Figure 4.9 show the H_2 formation efficiency as a function of grain radius for olivine and amorphous carbon respectively. The efficiencies are near unity for both surfaces and all grain sizes.

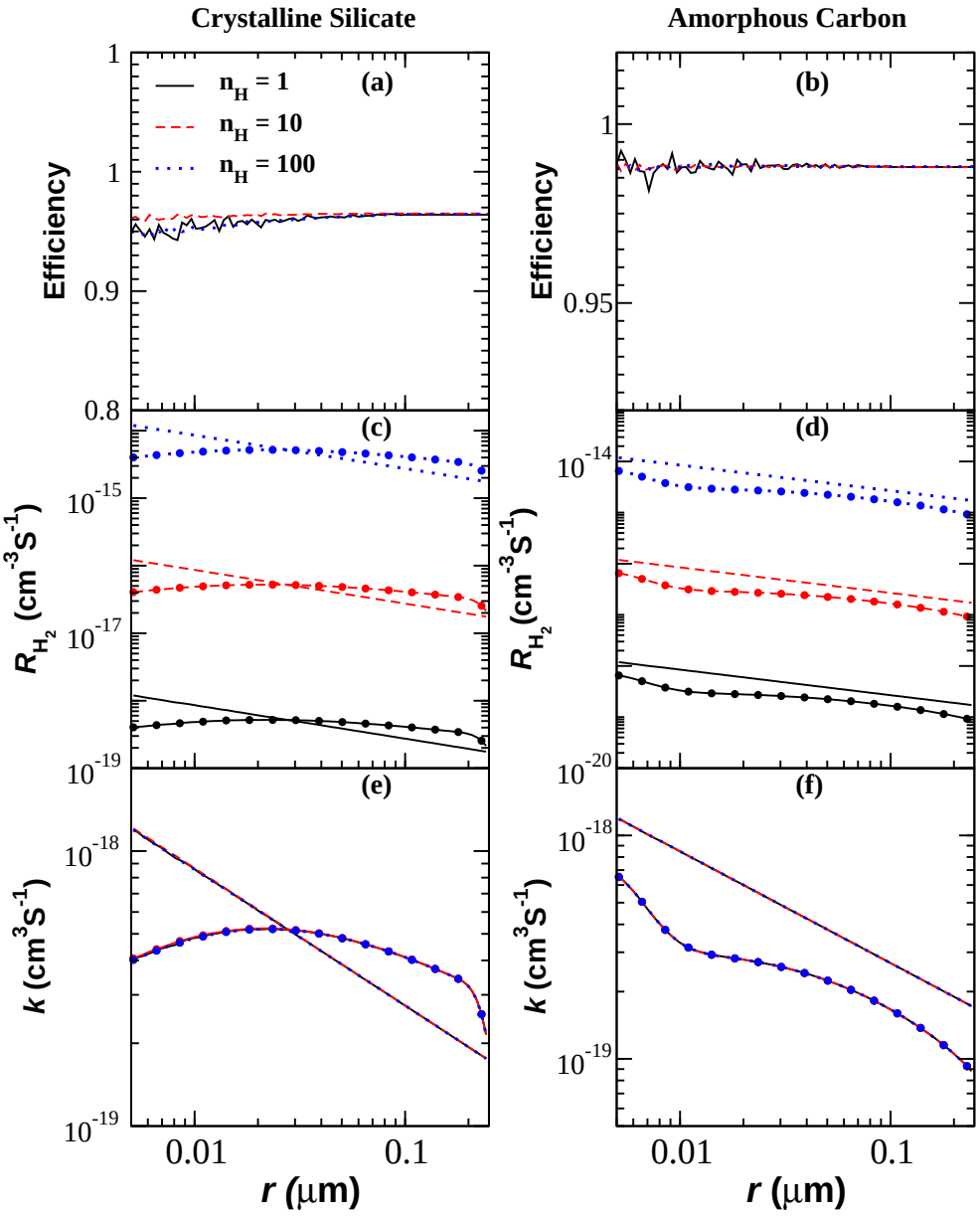

Figure 4.9: Variation of H_2 formation efficiency (panels (a) and (b)), rate of reaction (panels (c) and (d)) and rate coefficient (panels (e) and(f)) as a function of grain radius for Model 3 at times when the atomic hydrogen density is near its initial value. Gas density in cm^{-3}. Olivine ("crystalline silicate") and amorphous carbon surfaces are considered.

As for the overall rates, which can be seen in panels (c) and (d) of Figure 4.9, the contribution to the overall rate for olivine increases with decreasing grain radius with the MRN distribution. On the other hand, with the WDs distribution, there is a small increase with decreasing grain size, except at the smallest sizes where there is a decrease with decreasing radius below 0.02 μm. For amorphous carbon grains, with the MRN distribution, we see once again a rise in H_2 formation with decreasing grain size and on the other hand, for the WDc distribution, there is a somewhat sharper increase in the rate of H_2 formation for those grains smaller than 0.02 μm. Thus, looking at the effective size distributions in Figure 4.4, we conclude that the contribution to the overall rate for each grain radius scales with the effective size distribution. This implies a constant efficiency, which in this model is near unity for both surfaces. To summarize, for the MRN and WDc distributions, the maximum contribution derives from small grains, while for olivine, the maximum contribution is from medium size grains with the WDs distribution. The same information can be seen in panels (e) and (f) of Figure 4.9 for the dependence of the rate coefficient on granular size. Note that for these rate coefficients, there is no dependence on gas density since the efficiency is near 100%. The overall rate coefficients, as listed in Table 4.2, are all at or near the Jura (1974) value, which is consistent with the high efficiency.

Figure 4.10 shows the evolution of the atomic and molecular hydrogen abundances with overall proton densities of $n_{\rm H} = 10$ cm^{-3} and 100 cm^{-3}. The values for the H_2 fraction at 10^7 years are equal to the corresponding η_f values in Table 4.2.

4.4.3.2 Model 4

In the second chemisorption model, we considered H_2 formation by abstraction of an H-atom that is already chemisorbed on the grain surface. We have done calculations

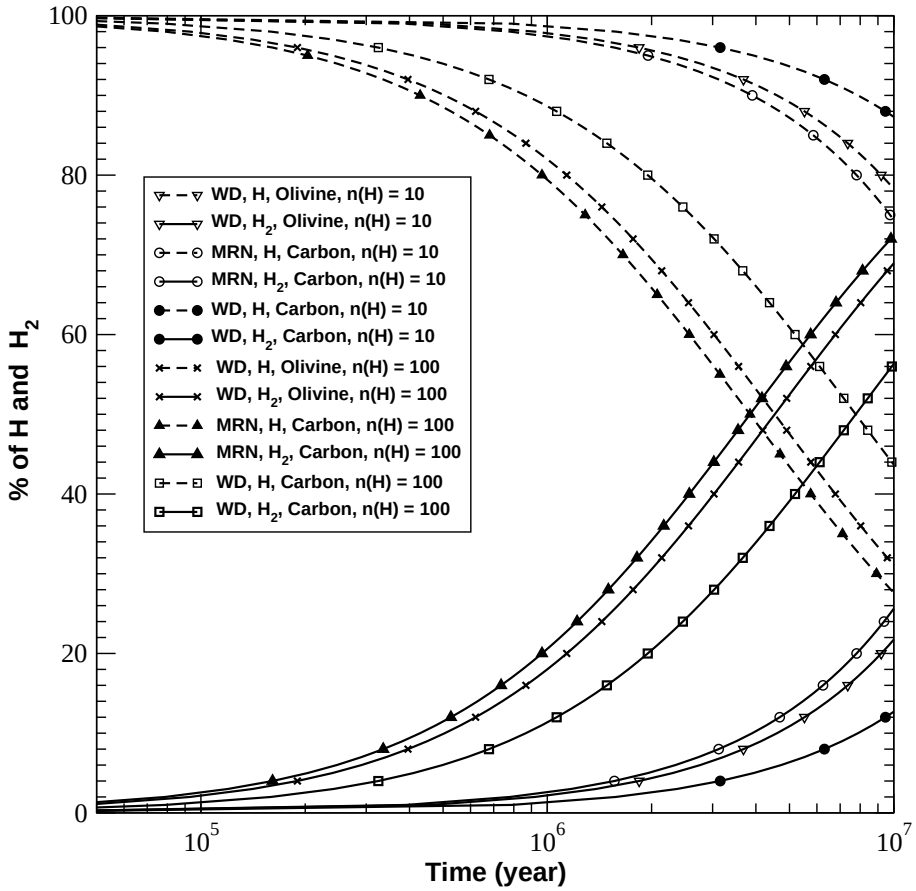

Figure 4.10: Time variation of gaseous H and H_2 abundances for Model 3 neglecting destruction processes for H_2, where the surface has both physisorption and chemisorption binding sites. The total proton density n_H is 10 or 100 cm^{-3} . The % of H_2 refers to the total number of H atoms in the form of H_2; i.e., % H_2 = 100 $\times 2n(H_2)/n_H$.

for two different barriers against chemisorption, 25 meV (290 K) and 162 meV (1880 K) respectively, based on calculations of extreme values concerning the (010) surface of forsterite (a crystalline silicate) by Garcia-Gil et al. (2013). We considered two different fluxes which correspond to $n_H = 10$ cm^{-3} and for $n_H = 100$ cm^{-3}, respectively.

A similar effect was observed as in Model 3; i.e., the reaction efficiency is constant at a certain value for all grain sizes. For a barrier of 25 meV, a constant efficiency of 0.6 was found, and for a barrier of 162 meV, the efficiency is 0.13, which is significantly less compared with the efficiency using the other chemisorption method. Formation rates

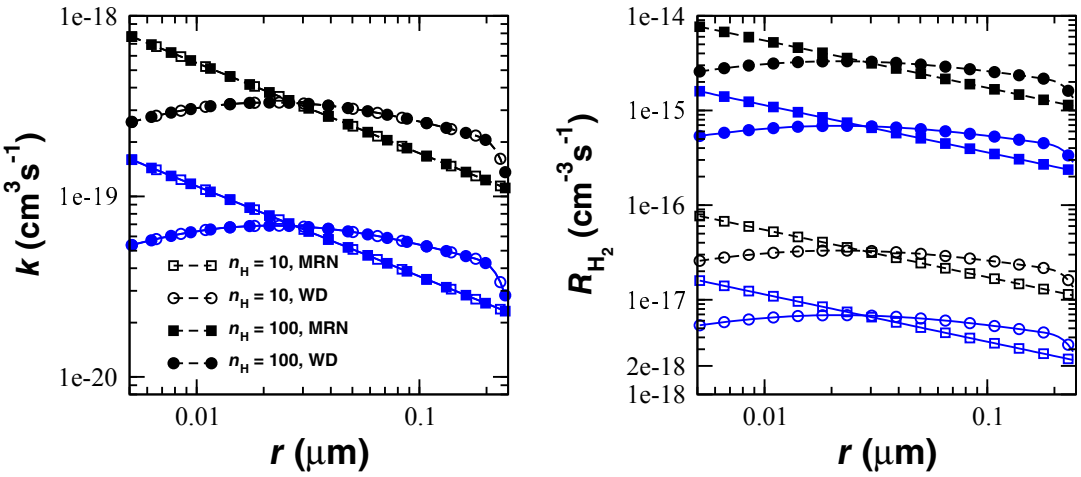

Figure 4.11: Rate of H_2 formation and rate coefficient as functions of grain radius for the ER method at times when the atomic hydrogen density is at its initial value. The gas densities shown are in units of cm^{-3}. Dashed lines correspond to barrier against chemisorption of 25 meV and solid lines are for a barrier of 162 meV.

and rate coefficients as a function of grain radius are shown in Figure 4.11. For this model also, the contribution to the overall rate for each grain radius scales with the effective size distribution. In Table 4.3, we have listed the overall rate of reaction, the conversion efficiency over 10^7 yr, and the overall rate coefficient for the two different chemisorption barriers. It can be seen that for a barrier of 25 meV, the rate coefficient is nearly half when compared with the other chemisorption method, whereas for a barrier of 162 meV, it is nearly one order of magnitude smaller. As discussed by Perets & Biham (2006), the gas temperature of 90 K in diffuse clouds may allow a greater penetration of the barrier than for Model 3, where the hydrogen atom is first thermalized to the grain temperature.

Table 4.3: Integrated H_2 formation rate, efficiency over 10^7 yr, and rate coefficient for Model 4 (ER Mechanism)

Olivine (ER mechanism)		MRN		WDs	
Model 4		$n_H = 10^a$	$n_H = 100$	$n_H = 10$	$n_H = 100$
162 meV	R_{H_2} (cm^{-3} s^{-1})	5.46(-16)	5.46(-14)	4.56(-16)	4.56(-14)
	η_f (%)	<3.33	<25.60	<2.80	<22.32
	k (cm^3 s^{-1})	5.46(-18)	5.46(-18)	4.56(-18)	4.56(-18)
25meV	R_{H_2} (cm^{-3} s^{-1})	2.63(-15)	2.63(-13)	2.19(-15)	2.19(-13)
	η_f (%)	<14.21	<62.35	<12.15	<58.04
	k (cm^3 s^{-1})	2.63(-17)	2.63(-17)	2.19(-17)	2.19(-17)

[a] Total proton density in units of cm^{-3}

4.4.4 Model 5: Models with Temperature Fluctuations

In the previous sections we presented results assuming an average temperature for each grain size. However, in a diffuse cloud, there will be temperature fluctuations, especially for small grains, due to their interaction with UV photons. During an event of photon hitting, the grain temperature will rapidly increase for a short interval of time. Then the grain will cool down at a time scale that is much longer. To determine the effect of temperature fluctuations on the formation of H_2, we treated photon interactions with the grain stochastically, as described in Section 4.2.2. For this model, the concept of parallel computation could not be applied since to achieve the first round of calculations took nearly 20 days. Therefore we could not run it for 10^7 years.

The H_2 formation efficiency as a function of grain radius for plain olivine and amorphous silicate is plotted in Figure 4.12. For both surfaces, the efficiency is higher when the temperature fluctuation is considered, as can be seen by comparison with the plotted efficiencies in Figure 4.7. Another important difference is the sharp rise in efficiency for amorphous silicate grains larger than 0.02 μm and for olivine grains larger than 0.05 μm. When these results are compared with those of Cuppen et al. (2006), who used a single modal temperature for each grain size, we find that the level of agreement depends on

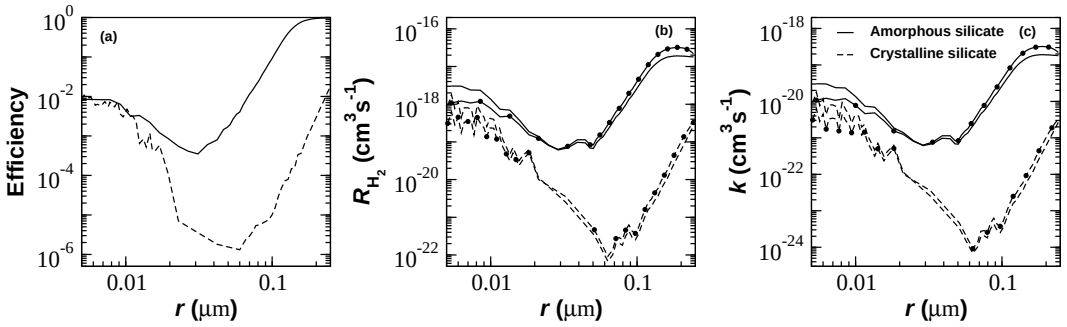

Figure 4.12: Panel (a): reaction efficiency as a function of grain radius for flat models of olivine and amorphous silicate with grain temperature fluctuation. Panels (b) and (c) are for the reaction rate and reaction rate coefficient, respectively. Plots are for $n_{\rm H} = 10$ cm^{-3}.

the type of surface. For two of their surfaces (surface - I and surface - II), they found that the efficiency increases as grain radius decreases (see their Figure 8) and for surface - III they found the reverse. Surface-I corresponds to flat olivine, so is best compared with our results, which show a more complex pattern with a minimum in efficiency in the middle of the radius range. In addition, we obtained much lower efficiencies for plain olivine.

Table 4.4: Integrated H_2 formation rate, efficiency over 10^7 yr, and rate coefficient for Model 5 (with temperature fluctuations)

Olivine		MRN	WDs
Model 5		$n_H = 10^a$	$n_H = 10$
Crystalline Silicate (olivine)	R_{H_2} (cm^{-3} s^{-1})	1.26(-17)	6.41(-18)
	η_f (%)^b	<0.08	<0.04
	k (cm^3 s^{-1})	1.26(-19)	6.41(-20)
Amorphous Silicate	R_{H_2} (cm^{-3} s^{-1})	2.76(-16)	4.18(-16)
	η_f (%)	<1.74	<2.64
	k (cm^3 s^{-1})	2.76(-18)	4.18(-18)

[a] Total proton density in units of cm^{-3}
[b] η_f for this model is calculated using initial rate

The calculated overall quantities are shown in Table 4.4. It can be seen that the

overall rate coefficients for olivine and amorphous silicate are much higher than the analogous values without temperature fluctuations, but that only the amorphous silicate surface leads to values that are nearly large enough to form H_2 efficiently.

We have also run the physisorption precursor model for carbon with chemisorbed sites in the presence of temperature fluctuations. However, we did not observe any difference in efficiency with the addition of temperature fluctuation. This result was expected, since for physisorption precursor chemisorption models, rates and rate coefficients do not depend on the grain size and grain material. Instead, they scale with effective surface area only, because in this temperature regime, H_2 formation occurs only when one physisorbed H-atom lands on a site occupied by a chemisorbed species. For this reason, this class of models will not be affected by temperature fluctuations.

4.5 Summary

Using the continuous-time random walk (CTRW) Monte Carlo technique (Montroll & Weiss, 1965), we have studied the formation of molecular hydrogen on olivine (a crystalline silicate), amorphous silicate, and amorphous carbon granular surfaces under diffuse cloud conditions, and calculated the efficiency of the process, its rate coefficient, and its total rate. Unlike many previous studies, we have considered the role of granular sizes and used grains that are distributed in various sizes, each of which possesses a different temperature. We used grain size distributions from Mathis et al. (1977) (MRN) and Weingartner & Draine (2001) (WDs and WDc), and, in most of our calculations, we took the dependence of average grain temperature with granular radius and surface composition from Draine & Lee (1984). In several calculations, however, we actually followed the temperature fluctuations of the small grains according to the approach of Cuppen et al. (2006). A parallel computational algorithm written in Fortran 95 was

used to carry out the simulations. Since larger grains are much smaller in numbers, we restricted consideration of grains to those with radii between 0.005 μm and 0.25 μm. We used 78 CPU's for the calculation, dividing the range of grain sizes into 78 values, each grain size to a CPU. Different sets of binding energies, barriers and other assumptions were used in models of H_2 formation for the three different surfaces. Model 1 consists of a flat surface with only one type of physisorption binding site and energy barrier, and reaction occurs via hopping over and tunneling under the physisorption barrier; Model 2 consists of a rough surface with a number of different binding energies and diffusion barriers caused by lateral bonds; Model 3 possesses both physisorption and barrierless chemisorption sites, with the physisorption sites used as precursors to the chemisorption ones, while Model 4 allows only direct chemisorption, which occurs over or through a barrier followed by an ER mechanism in which a gaseous hydrogen atom abstracts the first H atom off of the grain to form H_2. Model 5 is defined by following temperature fluctuations for small grains directly according to the approach of Cuppen et al. (2006) with plain olivine and amorphous silicate plus, for amorphous carbon, the physisorption precursor model for chemisorption.

If one looks at the calculated rate coefficients for H_2 formation in Tables 4.2 and 4.3, one can compare the results of most our models with the value of $\approx 10^{-17}$ cm^3 s^{-1} found by Jura (1974) to be needed to produce enough molecular hydrogen to explain observations in diffuse clouds. The tables also include the efficiency of conversion over 10^7 yr and the overall rate of the process at the initial time. We found that for olivine, neither the flat surface nor the rough one can account for the molecular hydrogen abundance in a diffuse cloud for either of the size distributions at any gas density used. Only a few larger grains form H_2 on their surface and in rather small numbers. For amorphous silicate, the calculated rate coefficients are much larger but still lie below the necessary value for efficient H_2 formation. For amorphous carbon, both surfaces used –

the smooth physisorption surface (Model 1), and the precursor mediated chemisorption surface (Model 3) – show reasonable to high efficiencies, with the surface with chemisorption sites showing high efficiencies for considerable portions of the range of grain sizes. These high efficiencies lead to high overall rate coefficients and, at the higher densities especially, to high overall rates of conversion from H to H_2 in 10^7 yr. In Model 3, where both chemisorption and physisorption sites are considered, molecular hydrogen is produced very efficiently in diffuse clouds at all grain sizes for both olivine and amorphous carbon. Indeed, for a flux corresponding to $n_H = 100$ cm^{-3}, H_2 reaches an upper limit of $\approx 70\%$ of the total proton density in 10^7 yr. Model 4, in which direct chemisorption onto olivine followed by abstraction is considered, leads to high overall rate coefficients for H_2 formation at the lower barrier of 25 meV and slightly lower rate coefficients with the higher barrier of 162 meV. Finally, when we consider temperature fluctuations in Model 5 for olivine and amorphous silicate, the formation efficiency increases for plain olivine and amorphous silicate as a function of grain radius, leading to increases in overall rate coefficient although the value of k for even the plain amorphous silicate is insufficient. For the physisorption precursor model for carbon, on the other hand, no change was found upon adding temperature fluctuations.

When these results are viewed against the back drop of measured diffuse cloud H_2 abundances, it can be seen that, according to our calculations, the standardly held assumption that the formation of H_2 occurs in a facile manner on grains with radii in the size range 0.005 - 0.250 μm is somewhat fragile in the sense that the rate of formation depends strongly on the surface used and its topology, the mechanism for the reaction, as well as on the type of binding of H. In addition, it is clear that a complete understanding of the H_2 formation rate for grains in the size range 0.005 - 0.250 μm will not be attained until the temperature dependence on grain size is fully resolved and the role of tunneling is further clarified with more accurate potentials (Taquet et al., 2013).

References

Acharyya, K., Hassel, G. E, & Herbst, E. 2011, ApJ, 732:73

Acharyya, K., Chakrabarti, S. K., & Chakrabarti, S. 2005, MNRAS, 361, 550

P. A., Kenyon S. J., 1979, Ap&SS, 65, 155

Bachellerie, D., Sizum, M., Aguillon, F., Teillet-Billy, D., Rougeau, N., & Sidis, V. 2009, PCCP, 11, 2715

C. F., Huffman D. R., 1983, Absorption and Scattering of Light by Small Particles. New York: Wiley, 1983

Cazaux S., & Tielens A. G. G. M. 2004, ApJ, 604, 222

Cazaux, S., & Tielens, A. G. G. M. 2010, ApJ, 715, 698

Chang Q., Cuppen H. M., & Herbst E. 2006, A&A, 458, 497

Cuppen, H. M., & Herbst E. 2005, MNRAS, 361, 565

Cuppen, H. M., Morata O., & Herbst E. 2006, MNRAS, 367

Draine, B. T., & Lee H. M. 1984, ApJ, 285, 89. Erratum: 1987, ApJ, 318, 485

Draine B. T., Li A., 2001, ApJ., 551, 807

Draine B. T., 2003, ARAA, 41, 241

Garcia-Gil, S., Teillet-Billy, D., Rougeau, N., & DSidis, V. 2013, J. Phys. Chem. A, 117, 12612

Iqbal, W., Acharyya, K., & Herbst, E., 2012, ApJ, 751, 581

Iqbal, W., Acharyya, K., & Herbst, E., 2014, ApJ, 784, 139

Ivanovskaya, V. V., Zobelli, A., Teillet-Billy, D., Rougeau, N., Sidis, V., & Briddon, P. R. 2010, Eur. Phys. J., B76, 481

Jeloaica, L., & Sidis, V., 1999, Chem Phys Lett., 300, 157.

Jura, M. 1974, ApJ, 191, 375

Katz N., Furman I., Biham O., Pirronello V., & Vidali G. 1999, ApJ, 522, 305

Kolasinski, K. W., 2002, Surface Science: Foundations of Catalysis and Nasnoscience (West Sussex, England: John Willey & Sons, Ltd.), p. 117

Lipshtat A., Biham O., & Herbst E. 2004, MNRAS, 348, 1055

Mathis J. S., Rumple W., & Nordsieck K. H. 1977, ApJ, 217, 425 (MRN)

J. S., 1990, ARA&A, 28, 37

Mennella, V., 2008, ApJ, 684, L25

Montroll, E., & Weiss, G. H, 1965, J. Math. Phys., 6, 167

Morisset, S., Aguillon, F., Sizun, M., & Sidis, V., 2004, The Journal of Physical Chemistry A, 108, 8571

Perets, H. B., & Biham, O. 2006, MNRAS, 365, 801

Perets, H. B., Lederhendler, A., Biham, O., et al. 2007, ApJ, 661, L163

E. M., 1976, ApJ., 206, 685

Smoluchowski, R. 1983, J. Phys. Chem., 87, 4229

Sternberg A., 1988, ApJ., 332, 400

Taquet, V. et al. 2013, A&A, 550, id. A127

Weingartner, J. C., & Draine, B. T. 2001, ApJ, 548, 296 (WD)

Whittet D. C. B., 2003, Dust in the Galactic Environment.Institute of Physics, Bristol

Zucconi A., Walmsley C. M., Galli D., 2001, A&A, 376, 650

5 Formation of water on the surface of interstellar dust grains.

5.1 Introduction

Water is probably the most important molecule in biological systems. Astronomers have detected water in gaseous/solid form, in various astrophysical environments such as planets, comets, meteorites, rotating disks surrounding young stars, interstellar clouds and star forming regions (Ehrenfreund et al. (2003); Dartois (2005)). The presence of water ice in the interstellar medium was proposed by Eddington (1937), but almost after four decades later, it was directly detected in dark interstellar clouds through infra-red at 3 μm by (Gillett and Forrest (1973)). In cold and dense regions of the interstellar medium, icy mantles are formed over dust grains, thickness of such icy mantles can be of few 100 monolayers, these mantles are mainly made of water. Thus water is the most important constituent of icy mantles over which many other complex molecules are formed. Life on earth is not possible without water. Earth has huge abundance of water in all three forms, gas, liquid and solid. But, abundance of water on the planet earth is still a subject of debate (Morbidelli et al. (2000)).

In standard gas-phase chemistry, water is formed through ion-molecule reactions starting with the formation of OH^+ via following reactions:

$$O + H_3^+ \rightarrow H_2 + OH^+ \tag{5.1}$$

$$O + H_2^+ \rightarrow H + OH^+, \tag{5.2}$$

Then a series of rapid hydrogen abstraction reactions with H_2 leads to H_3O^+, which can dissociatively recombine to form H_2O and OH with branching ratios of ~ 0.33 % and $\sim$ 66 % respectively. However, this route is not efficient enough to reproduce the observed abundances in dark clouds, especially that found in its solid form (Parise et al. (2005); Ceccarelli et al. (2007)). Thus accretion of water ice from the gas phase to grain surface is not sufficient to account for water on the grain surface, instead, it must form directly on the dust grains. This makes the study of gas grain interaction in the ISM of immense importance. Only a proper understanding of synthesis of water in the ISM can make us understand the mystery of formation of more complex organic molecules that form on it under these conditions.

Tielens and Hagen (1982) suggested that H_2O formation would be initiated by H-atoms reacting with O, O_2 and O_3. The O_3 + H pathway was considered the most effective and was proposed that O_2 would play more a catalytic role in the formation of water. More recent Monte Carlo simulations by Cuppen and Herbst (2007) show that while the main route to water formation on the interstellar dust grains in diffuse and translucent clouds is the reaction H + OH. Whereas in dense clouds the principal source of water formation is the reaction between H_2 and OH.

In recent experimental works, Dulieu et al. (2010) studied the synthesis of water formation on a realistic analogue of grain surface in dense clouds, i.e., amorphous water ice. In their experiment, by exposing O and D-atoms to an amorphous water ice substrate

held at 10 K, deuterated water molecules were formed with a high efficiency (~ 0.5). Thus their results imply that the O + H reaction pathway is an important route for water formation in interstellar environments with a number density greater than $10^4/cm^3$. These authors also believe that the same mechanism is the most efficient in diffuse clouds and (particularly) in the boundary layers of dense clouds where UV photons and atomic species dominate.

One unexplored area is water formation in the diffuse clouds. It is important because it can give us information that at what point water begin to form efficiently on the grain surface when interstellar cloud evolves from a diffuse cloud to a dense cloud during gravitational collapse. In this Chapter, we explored water formation in diffuse clouds using, our model that is used for studying H_2 formation in the Chapter 4. In this work, we used a small network involving O and H atoms and molecules that form from these two species. We considered accretion of only H and O from the gas phase and used CTRW Monte Carlo technique as described in Chapter 2. We studied temperature dependence, flux dependence and size dependence on water formation. In the next section, we discussed our model, then we discussed water formation pathways and various physical parameters that are used for this study. Finally, we discussed our main results and summery.

5.2 Model

In this work we modify our previously discussed CTRW Monte Carlo model to incorporate formation of many molecules in the simulation, previous model could simulate formation of only a single molecule and only a monolayer formation of molecules was possible. However this model handles multi-layer formation of various molecules. In simple words, the previous model was basically a 2D scheme of chemical evolution on

the surface of dust grains where each atom or molecule could have at most four neighbours but this modified version simulates a 3D grid of lattice points and each atom or molecule can have six neighbours (one at the top and one at the bottom in addition to 4 side neighbours). Molecules like water, can not desorb back efficiently at temperatures representative of diffuse (10 to 25 K) and dense cloud (5 to 15 K) and gets accumulated on the grain surface and forms several layers. To incorporate this aspect, we considered a 3 D structure. A cartoon diagram 3D structure is shown in the Figure 5.1. It is clear that, we need two sets of binding energies, first binding energies of various species with the bare silicate grain, and, second, binding energy of any species with the particular species lying beneath it.

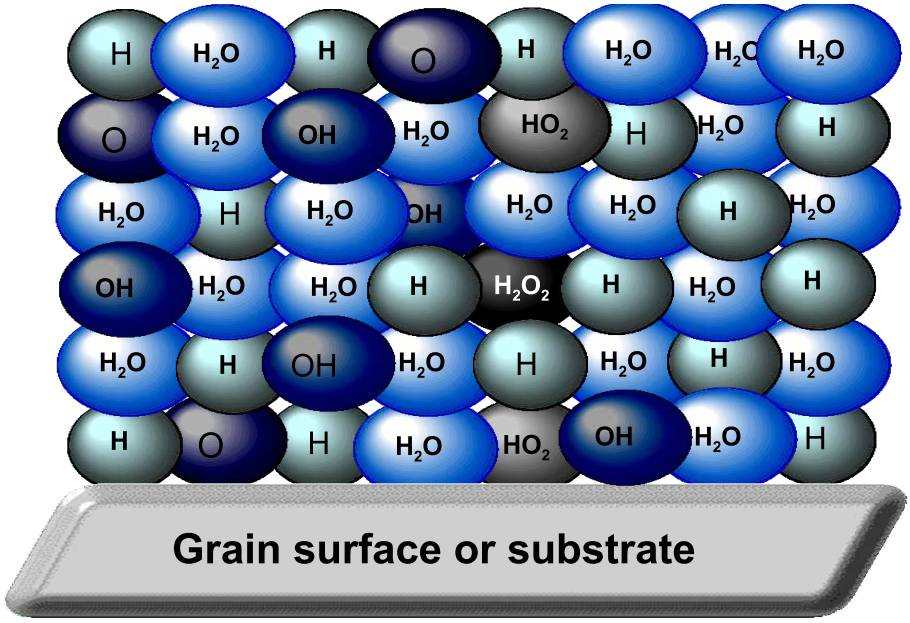

Figure 5.1: A cartoon diagram of 3D layers on the interstellar dust grains.

In this model we start with a square lattice with boundary conditions as described in earlier model in previous chapters. When an atom accrets, it is given a random site to adsorb. There are two possible scenarios, depending on whether the site is already occupied or not. If the site is not occupied, then the accreted species can sit on the

surface of the bare grain/species at the randomly generated (h,k)th location. However, if the site is occupied then either a reaction between the incoming and the stationary species will occur, provided the reaction is permitted, forming a new molecule, or the incoming species will sit at the top of the species and moves to a neighbouring site in next hopping interval. Basic accretion, hopping and desorption mechanism and equations used to calculate their respective waiting times are same as discussed in Chapter 2.

5.3 Grain surface chemistry and formation route of water

Water mainly forms on the grain surface via LH mechanism. There are mainly four formation routes for water (van Dishoeck et al. (2013)).

Formation route 1, starting from O: In this series of reactions, both atomic H and atomic O accrete onto a grain, diffuse toward one another, and form the radical OH. A second H atom lands on the grain and diffuses to the OH to form water:

$$\mathrm{H + O \rightarrow OH} \quad ; \quad \mathrm{OH + H \rightarrow H_2O} \tag{5.3}$$

Formation route 2, starting from O_2: This mechanism starts with the diffusive formation of molecular oxygen,

$$\mathrm{O + O \rightarrow O_2} \tag{5.4}$$

The molecular oxygen can then add atomic H twice to form the HO_2 radical and then H_2O_2,

$$\mathrm{O_2 + H \rightarrow HO_2} \quad ; \quad \mathrm{HO_2 + H \rightarrow H_2O_2} \tag{5.5}$$

It is also possible for the second step to occur with molecular rather than atomic hydrogen, although the amount of H_2 on or in the ice mantle is poorly determined. Moreover, the reaction between HO_2 and H_2 may have an activation energy barrier. Once hydrogen peroxide is produced, it can react with atomic hydrogen to form OH and H_2O:

$$H_2O_2 + H \rightarrow OH + H_2O \tag{5.6}$$

The newly formed OH can react once again with H to form H_2O.

Formation route 3, starting from O_3: Once O_2 is formed in the grain surface, addition of another surface/ice oxygen atom can produce ozone. The ozone can then react with H to form OH and O_2, followed by reaction of OH with H to form water, as already discussed.

Formation route 4, using H_2: The reaction between surface OH and molecular hydrogen to form water and H is controversial. There is a newly measured rate coefficient that suggests that the reaction can occur via tunneling, although this reaction possesses considerable activation energy in the gas-phase.

In our calculations, we considered first three formation mechanism for water formation along with the other reactions. We considered accretion of H and O on the grain surface and followed their motion over the surface. We considered following possible reactions,

$$H + H \longrightarrow H_2 \tag{5.7}$$

$$H + O \longrightarrow OH \tag{5.8}$$

$$OH + H \longrightarrow H_2O \tag{5.9}$$

$$H + O_2 \longrightarrow H_2O \tag{5.10}$$

$$H + O_2 \longrightarrow HO_2 \tag{5.11}$$

$$H + HO_2 \longrightarrow H_2O_2 \tag{5.12}$$

$$H + H_2O_2 \longrightarrow H_2O + OH \tag{5.13}$$

$$O + O \longrightarrow O_2 \tag{5.14}$$

$$O + O_2 \longrightarrow O_3 \tag{5.15}$$

$$O + OH \longrightarrow O_2 + H \tag{5.16}$$

Thus we have in total, ten possible reactions between two atomic species (H and O) and seven molecular species ($H_2, O_2, O_3, OH, H_2O, H_2O_2, HO_2$). Energy values required to calculate the mobility and desorption rate of all these species are shown in Table 5.1.

Figure 5.2 shows the mobility of H and O on the surface calculated using parameters as given in Table 5.1. We see in the Figure 5.2, that the mobility of hydrogen atom is many order higher than that of oxygen atom at low temperature. Thus chemical reactions are mostly governed by hydrogen atoms at low temperature. Virtually, hydrogen can be considered the only mobile species on the surface of the dust grain. Although, with the rise in temperature of the dust grain, the difference in mobility of hydrogen atom and that of oxygen atom decreases sharply but still it is few order of magnitude less even at 20 K. Other species is more strongly bound with the surface, therefore they will have even lower mobility than atomic oxygen. Therefore we neglected their movement on the grains. Thus we have two mobile species H and O and all other species are stationary.

Table 5.1: Binding energies at top of silicate surface.

Species	Substrate			
	Amorphous olivine		Water	
	Binding energy (E_1) (K)	Desorption energy (E_2) (K)	Binding energy (E_1) (K)	Desorption energy (E_2) (K)
H	404	510	500	650
H_2	135	300	330	440
O	650	800	600	800
OH	900	1260	2600	3500
H_2O	1500	2000	4200	5640
H_2O_2	3700	4950	3700	4950
HO_2	3200	4300	3200	4300
O_2	750	1000	750	1000
O_3	1350	1800	1350	1800

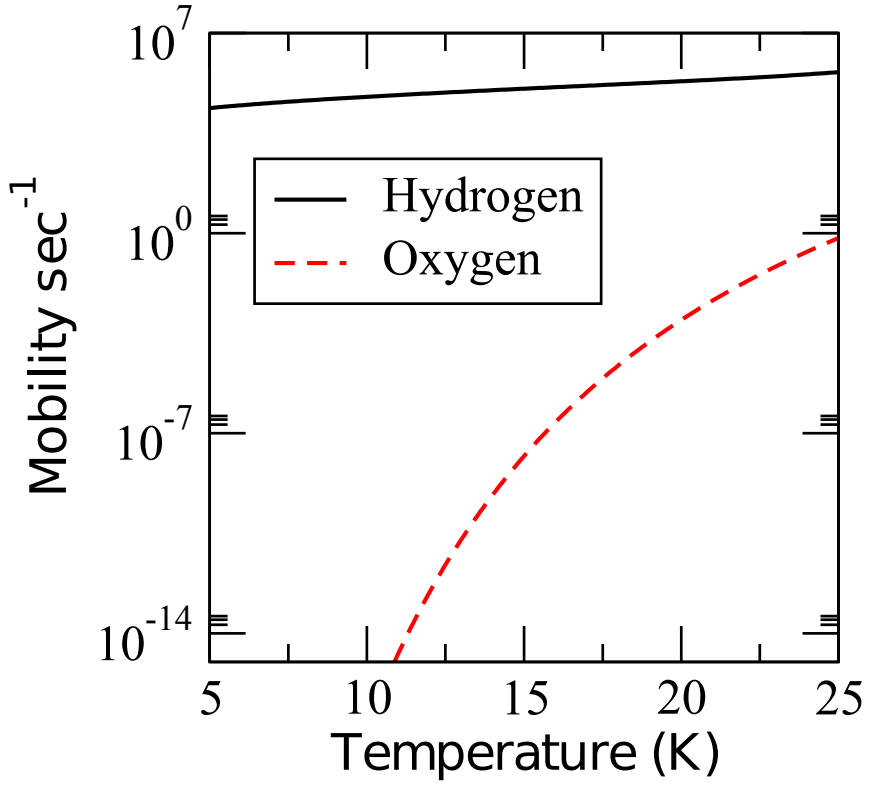

Figure 5.2: Mobility of H and O, on the amorphous silicate surface, calculated using parameters as written in Table 5.1.

5.4 Results

In the following subsections we presented results for water formation. All the calculations (other than the size distribution calculations) are done for 0.01 micron size grain with 50 $\times$ 50 binding sites. We avoided bigger size grains due to very high computational time required for calculation and it does not provide any extra information. Grains smaller than 0.01 micron is avoided, because formation of molecules is dependent on grain size when the sizes are smaller than 0.01 micron. We have discussed this issue farther when we have shown calculations with the size distribution.

5.4.1 Formation of Water

In Figure 5.3, we show water production (in monolayers) on dust grain as a function of time for various accretion rates of gaseous H atom. The gaseous oxygen abundance is considered to be 10^{-4} relative to the total hydrogen density. It can be seen that as H flux increases, production rate of water also increases and as temperature increases production of water decreases. These results can be divided into two parts, one for diffuse cloud conditions and other other for dense cloud conditions. For diffuse cloud conditions (flux corresponding to n_H = 1 to 10 cm^{-3} and temperature between 15 - 20 K), water abundance is very low. Only a fraction of a monolayer is grown on the surface for flux corresponding to n_H = 1 cm^{-3}, and it increases to about 2 monolayer for flux corresponding to n_H = 10 cm^{-3}. However, for dense cloud conditions (flux corresponding to $n_H \geq$ 500 cm^{-3} and temperature between 6 - 15 K), water formation is very efficient, maximum water abundance can go up to 200 monolayers, which is consistent with the observations (Gibb et al. (2000)).

Top panel in Figure 5.4 shows fraction of H forming H_2 and H_2O (lines with circles) and bottom panel shows fraction of O forming H_2O. Here I would like to recall

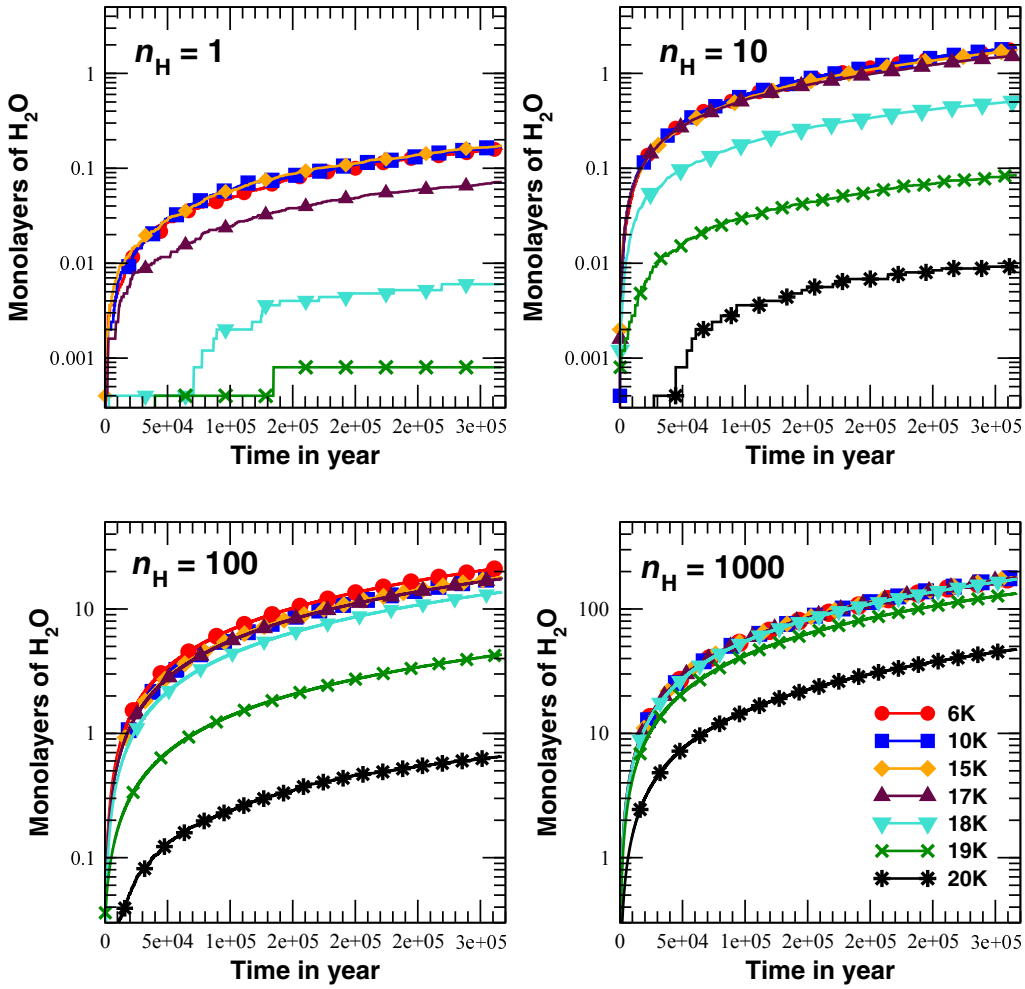

Figure 5.3: Production of water in monolayer for different flux of H.

our results shown in Chapter 3, where we showed that H_2 production decreases when coverage of H atom decreases. But in Figure 5.4, we see that although production of H_2 started to decrease after 10 K, indicating that H coverage is going down, production of water remains unchanged and steady. Thus Figure 5.4, clearly shows the temperature dependence for water production comes only when contribution of oxygen atom starts to decrease. Since, oxygen desorption rate is negligible below 15 K, it can stay on the grain surface and react with adsorbed H atom to form water. In addition, since, oxygen accretion rate is four order of magnitude less than the hydrogen, even at 15 K, there is enough H-atoms to use up all oxygen on the grain. Therefore water formation is

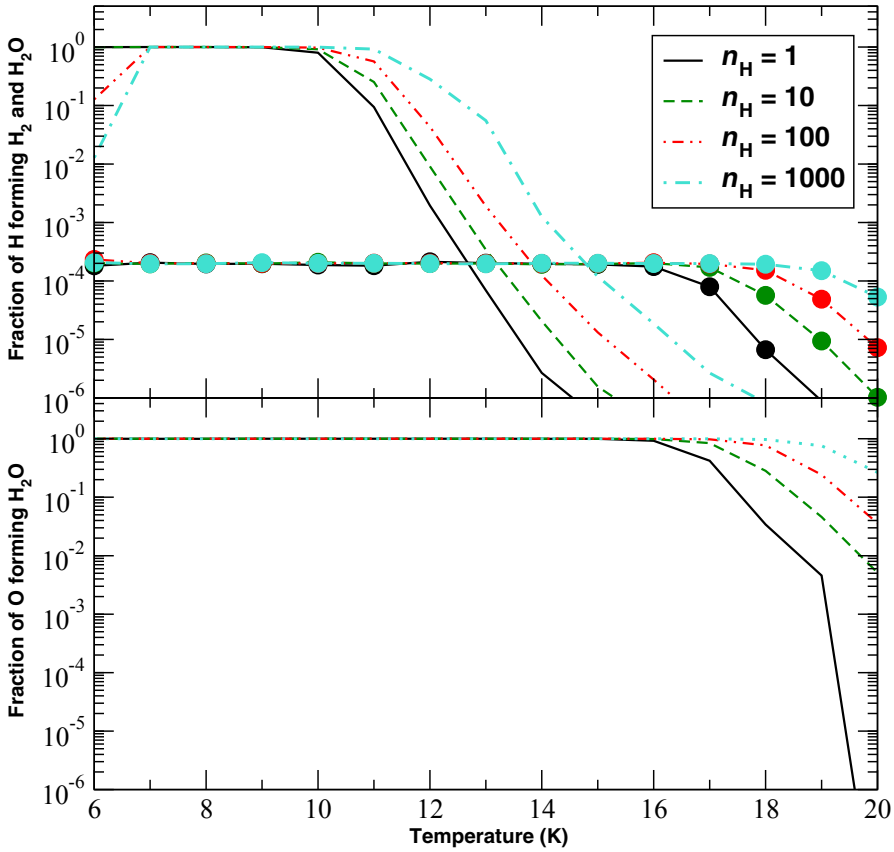

Figure 5.4: Top panel: Fraction of H forming H_2 and H_2O (lines with circles).Bottom Panel: Fraction of O forming H_2O.

independent of H coverage below 15 K. This is also evident from the fact that up to 15 K, almost all O are contributing in water production. As temperature rises further, due to desorption of O atoms, their contribution towards water production decreases and hence water production rate also decreases further. And correspondingly, fraction of H forming water also decreases.

5.4.1.1 Effect of tunneling

Figure 5.5 shows the effect of tunneling in water production. We see that when we considered both tunneling and thermal mobility, water production rate improves slightly above 15 K, below this temperature there is no change in water production as almost

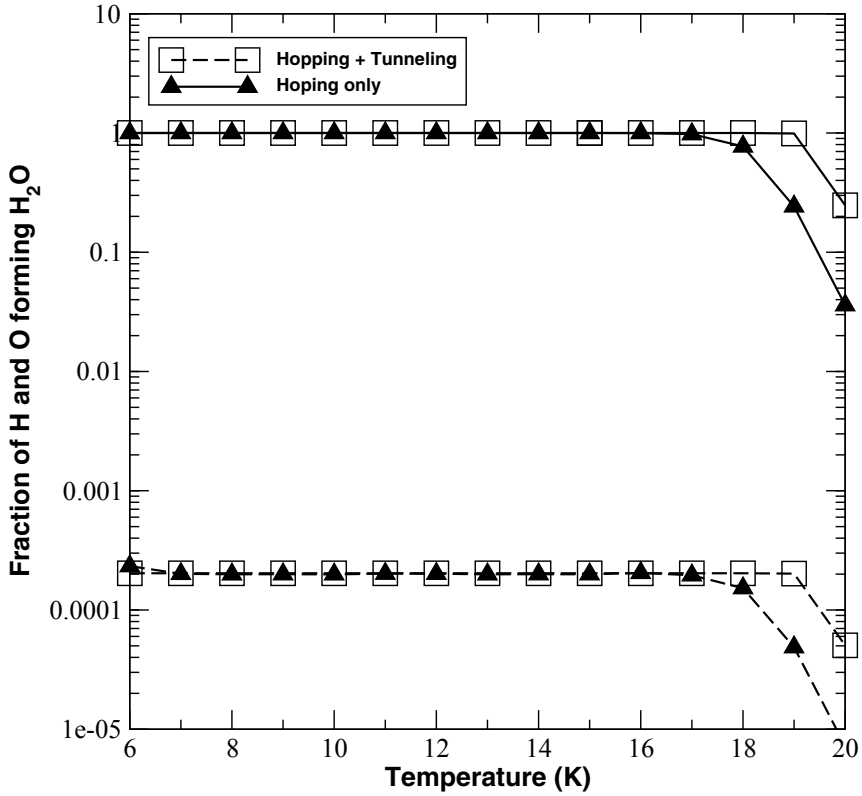

Figure 5.5: Effect of tunneling on water production. Fraction of H (dashed lines) and O (solid lines) forming H_2O, these results are for $n_H = 100$ cm^{-3}.

all O are already contributing to water formation. But above 15 K due to increased mobility of H and O, water production improves as we have observed in the case of production of hydrogen molecule also.

Figure 5.6 shows how inclusion of tunneling translates into number of water monolayers produced. At 20 K around 2 monolayers is formed when both tunneling and hopping is considered, and, in absence of tunneling it is only 0.5 monolayer, a factor of four less. Thus at this temperature considering tunneling is important. However, as temperature is decreased, at 18 K this gap is significantly less and completely goes away by 15 K. Thus, below 15 K tunneling may be neglected for water formation study.

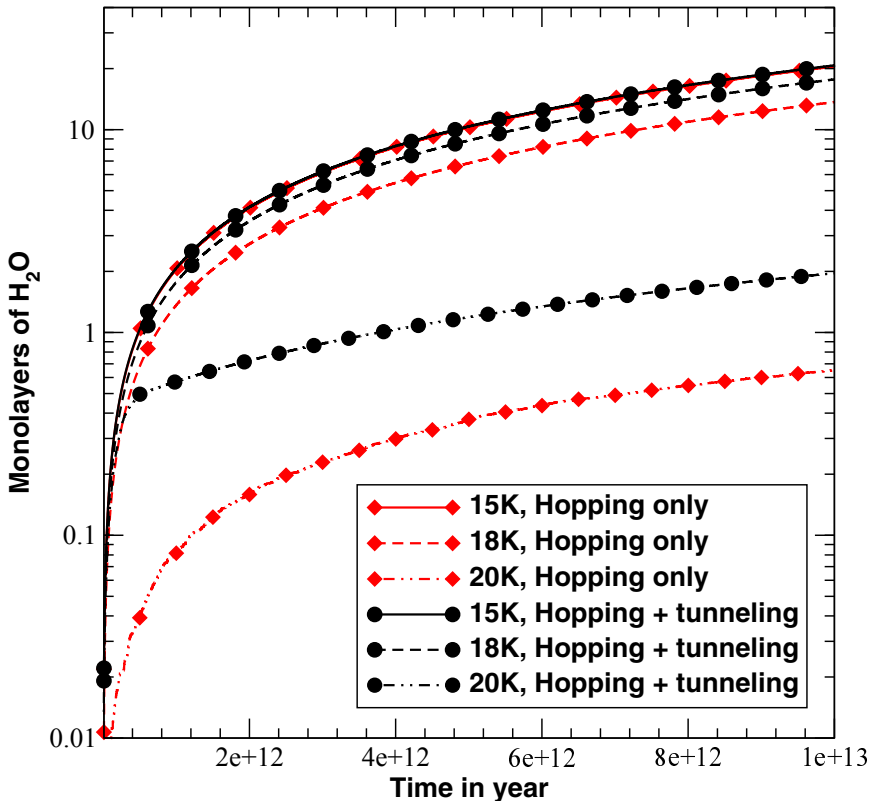

Figure 5.6: Production of water in monolayer, showing the difference between hoping only and hopping + tunneling case. These results are for fluxes that corresponds to $n_{\rm H} = 100$ cm^{-3}.

5.4.1.2 Effect of grain size

In Figure 5.7, we see the effect of grain size variation on production of water in diffuse clouds. Here we used the MRN grain size distribution as described in Chapter 4 and same steady state temperatures for each grain size. We run our simulation with a fixed flux of H corresponding to $n_{\rm H} = 100$ cm^{-3} and O-atom flux corresponding to oxygen abundance of 10^{-4} relative to the total hydrogen density. In the plot, dashed line with square represent fraction of H forming water and dotted line with diamond represent fraction of O forming water, we see that all oxygen atom accreting to grain surface are forming water for all grain sizes, thus no O atoms are lost due to desorption. Thus there is almost no grain size dependence on water formation as far as the average

grain temperature on the diffuse temperature are not high enough to cause considerable desorption of adsorbed O atoms. Figure 5.8 production of water on dfferent size of grains.

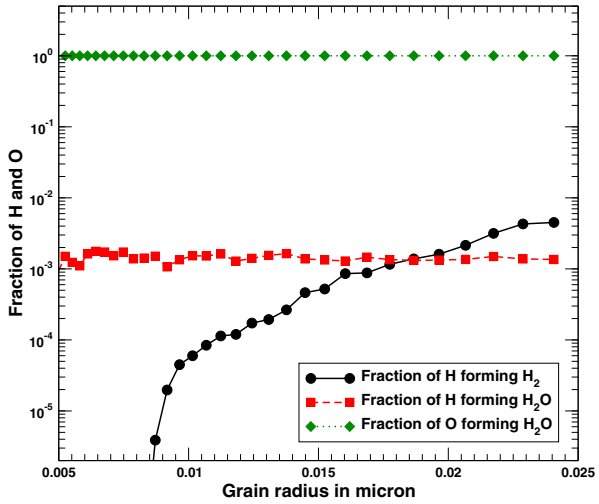

Figure 5.7: Fraction of H (dashed line with square) and O (dotted line with diamond) forming H_2O, and fraction of H (solid line with circle) forming H_2, these results are for $n_{\rm H} = 100$ cm^{-3}.

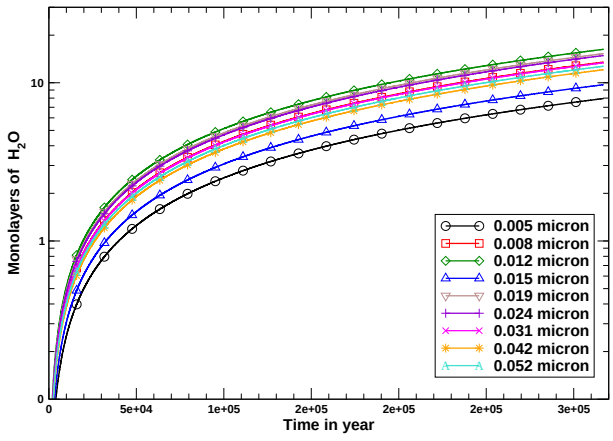

Figure 5.8: Production of water in monolayers as a function of time in year, these results are for $n_{\rm H} = 100$ cm^{-3}.

5.4.1.3 Effect of photon heating on grains

We also studied water formation when grain temperature fluctuates due to interaction with the stellar UV photons. We used same method for heating and cooling of grains as described in Chapter 4, and considered MRN grain size distribution. We saw in the above section that when we used average values of temperature for dust grains, then there is no grain size effect in formation of water although the formation rate of hydrogen molecule is affected.

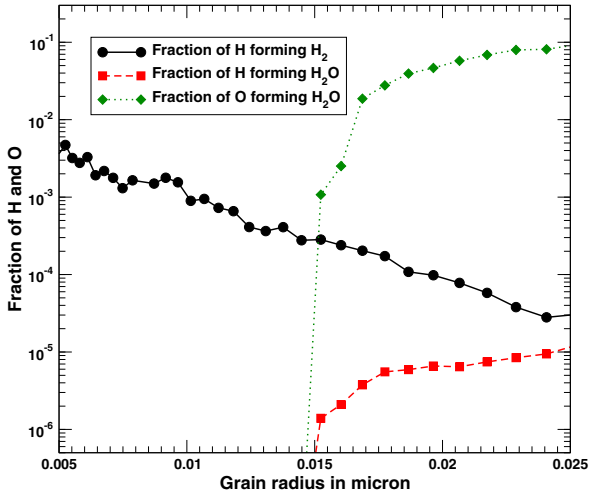

Figure 5.9: Fraction of H (dashed line with square) and O (dotted line with diamond) forming H_2O, and fraction of H (solid line with circle) forming H_2, these results are for $n_{\rm H} = 100$ cm^{-3}.

But in Figure 5.9, we see that with temperature fluctuation included, the water formation is not independent of sizes of dust grains. Small grains are unable to form any water on them. Although H_2 is forming on small grains (solid line with circle), mainly because it has four order of magnitude more accretion rate than oxygen atom. Due to photon hitting temperature rises to $\sim$ 40K (see Figure 4.6), resulting desorption of all H and O from the surface. Thus for small grains (< 0.015 μm), the probability is very low for any H or O atom to stay on the surface long enough to take part in chemical

reaction which is necessary for water formation. But as grain size increases the peak temperature due to photon hitting decreases as shown in Chapter 4, this results in low desorption rate and we see increased water formation rate.

5.4.2 Formation of other molecules

In these calculations we included formation mechanism of 7 molecules, H_2, O_2, O_3, OH, H_2O, H_2O_2 and HO_2. We observed high abundance only for molecular hydrogen and water as discussed in earlier subsections. Apart from these two, OH is also produced at the same rate as for water. Due to very low desorption rate of OH, and high mobility of H atoms on the surface, all OH were rapidly converted to water. Therefore, on the grain surface, we observed only a very small number (~ 5) of OH. Same is very true for O_2. As almost all O is converted to OH and then water, we did not observed any noticeable production of O_2. Resulting in almost negligible production of other bigger molecules like HO_2, H_2O_2 and O_3 under diffuse cloud conditions.

5.5 Summary

We used CTRW Monte Carlo simulation to study formation of water and few other molecules in diffuse clouds. We found that, formation of water mainly depends on coverage of O on the surface. Water formation rate goes down only when temperature is high enough to cause significant desorption of O from the surface else all O accreted to the surface is converted to water. We found that when average grain temperature is used under diffuse cloud conditions, there is no size dependence on the water formation. However, when we use temperature fluctuations, then small grains do not produce any water on their surface due to higher temperature due fluctuation and only bigger grains

can produce water and that too at reduced rate. Molecules other than H_2 and water is not produced in significant numbers.

References

Ceccarelli, C., Caselli, P., Herbst, E., Tielens, A. G. G. M., & Caux, E. 2007, in Protostars and Planets, ed. V. B. Reipurth, D. Jewitt, & K. Keil (U. Arizona Press) 47

Cuppen, H.M., & Herbst, E., 2007 ApJ, 668, 294

Dartois, E. 2005, Space Science Reviews, 119, 293

Dulieu, F., Amiaud, L., Congiu, E., Fillion, J. H., Matar, E., Momeni, A., Pirronello, V., & Lemaire, J. L., 2010, A&A 512, A30

Eddington, A. S., 1937, The Observatory, 60,99

Ehrenfreund, P. et al. 2003, Planet. Space Sci., 51, 473

Gibb, E. L., Whittet, D. C. B., Schutte, W. A., et al. 2000, ApJ, 536, 347

Gillett, F. C., & Forrest, W. J., 1973, ApJ, 179

Leger, A. et al. 1979, A&A 79, 256

Morbidelli, A. et al. 2000, Meteoritics & Planetary Science, 35, 1309

Parise, B., Ceccarelli, C., & Maret, S. 2005, A&A, 441, 171

Tielens, A. G. G. M., & Hagen, W., 1982, A&A 114, 245

van Dishoeck, Ewine F., Herbst, Eric & Neufeld, David A, 2013, Chemical Reviews, 113, 9043